UNIVERSITÉ DE MONTRÉAL

PLASMONIC AND NANOPHOTONICS SENSORS FROM VISIBLE TO TERAHERTZ

ALIREZA HASSANI
DÉPARTEMENT DE GÉNIE PHYSIQUE
ÉCOLE POLYTECHNIQUE DE MONTRÉAL

THÈSE PRÉSENTÉE EN VUE DE L'OBTENTION
DU DIPLÔME DE PHILOSOPHIÆ DOCTOR
(GÉNIE PHYSIQUE)
MAI 2009

Your file Votre référence
ISBN: 978-0-494-53797-8
Our file Notre référence
ISBN: 978-0-494-53797-8

UNIVERSITÉ DE MONTRÉAL

ÉCOLE POLYTECHNIQUE DE MONTRÉAL

Cette thèse intitulée:

PLASMONIC AND NANOPHOTONICS SENSORS FROM VISIBLE TO TERAHERTZ

présentée par: HASSANI Alireza

en vue de l'obtention du diplôme de: Philosophiæ Doctor

a été dûment acceptée par le jury d'examen constitué de:

M. MARTINU Ludvik, Ph.D., président

M. SKOROBOGATIY Maksim A., Ph.D., membre et directeur de recherche

M. CALOZ Christophe , Ph.D., membre

M. BOCK Wojtek J., Ph.D., membre

TO MY FAMILY AND ALL OF MY MENTORS

"Imagination is more important than knowledge."

- Albert Einstein

"Man's mind stretched to a new idea never goes back to its original dimensions."

-Oliver Wendell Holmes

ACKNOWLEDGMENTS

I would like to thank all my friends and colleagues at Engineering Physics Departments, Ecole Polytechnique, specially Dr. Elio Pone, Bertrand Gauvreau, Alexandre Dupuis, Ning Guo, Francis Bisomenu, Laurent Chouinard, Bora Ung.

I am grateful to thank Profs. Wojtek J. Bock, Ludvik Martinu, Christophe Caloz, and Charles Dubois who accept to evaluate my PhD thesis.

I would like to thank the secretaries and other staffs at the Engineering Physics Department, Ecole Polytechnique.

I wish to thank my wife and family for their support during my PhD study.

RÉSUMÉ

Nous démontrons dans cette thèse la conception de nouveaux capteurs plasmoniques compacts et ultra sensibles couvrant un domaine spectral du visible jusqu'aux ondes THz. Cet objectif est atteint en considérant, d'une façon systématique, plusieurs sous catégories de l'objectif principal. D'abord cette thèse démontre l'excitation plasmonique dans des fibres microstructurées TIR dont les trous sont revêtus d'un mince couche d'or opérant à titre de capteurs biochimiques à fonctions microfluidiques de même qu'un concept de capteurs plasmoniques basés sur des guides d'ondes à bande photonique interdite oeuvrant dans le visible et l'IR. Deuxièmement nous développons le critère du design d'un nouveau type de fibre poreuse à faibles pertes dans le régime des THz qui doit être utilisée comme base d'un capteur plasmonique. Troisièmement respectivement, nous proposons des critères de design de capteurs plasmoniques basés sur des fibres à bande photonique interdite et des capteurs plasmoniques basés sur des fibres poreuses à faibles pertes oeuvrant dans le régime des THz. Pour le régime des THz, nous considérons l'utilisation de ferroélectriques en remplacement des métaux et nous découvrons qu'ils sont susceptibles de supporter des plasmons de surface.

Nous introduisons la notion de capteur à résonance de plasmons de surface basés sur des fibres optiques microstructurées. Les deux principaux défis de la conception des capteurs sont identifiés, c.à.d. la correspondance de la phase entre les modes guidés dans le cœur et les modes plasmoniques, et deuxièmement l'optimisation microfluidique pour permettre un écoulement efficace de la substance à analyser. La correspondance de phase a été facilitée par l'introduction d'une microstructure dans le cœur de la fibre. Des fonctions microfluidiques étendues sont obtenues par l'intégration de grands canaux adjacents au cœur de la fibre.

Nous présentons une approche novatrice de design d'un capteur plasmonique basé sur un guide d'onde plan dans lequel le mode de cœur gaussien d'un guide effectivement unimodal est en phase à toute longueur d'onde désirée avec un plasmon de surface qui

se propage à la jonction entre un revêtement métallique et le milieu diélectrique ambiant. En faisant varier la taille du coeur du guide d'ondes (ou par variation de la géométrie du coeur), on peut déplacer la relation de dispersion d'un mode de cœur vers celle du mode plasmonique jusqu'à ce que la correspondance de phase se manifeste à λ_c. La longueur du capteur peut être modifiée par la variation du nombre de couches de réflecteur, davantage de réflecteurs résultant en un capteur plus long. Nous avons présenté des exemples de capteurs à SPR aqueux basés sur un guide d'onde à cristaux photonique, des fibres de Bragg à cœur solide ou liquide, ainsi que des fibres microstructurées à cristaux photoniques et cœur solide.

Ensuite, nous considérons la conception de fibres poreuses à faibles pertes opérant dans le régime des Terahertz pour leur utilisation dans le corps d'un capteur plasmonique. L'utilisation d'une expression approximative analytique pour calculer les pertes par macrocourbure, nous permet de conclure que les fibres poreuses suggérées sont très résistantes à la courbure, avec des pertes par courbures inférieures à la perte d'absorption modal même pour des courbures aussi serrées que 3 cm de rayon. Deuxièmement, nous avons considéré des fibres de Bragg poreuses à large bande photonique interdite fabriquées par des couches de matériau concentriques suspendues dans l'air à l'aide un réseau des ponts circulaires. Le diamètre de la fibre à cœur creux est beaucoup plus grand que la longueur d'onde d'opération, permettant ainsi un couplage efficace de diverses sources THz. Bien que les pertes totales modales (d'absorption et du rayonnement) plus faibles que 5 dB/m puissent être atteintes avec une matériau qui a des pertes de volume de 130 dB/m, la bande passante de la fibre a été trouvé inférieure à 0.1 THz.

Nous avons proposé des critères de conception d'une fibre de Bragg à cœur solide destinée à servir de capteur plasmonique à THz où l'excitation du plasmon THz sur un film mince de polymère de fluorure de Polyvinylidène (PVDF) par l'intermédiaire d'une correspondance de phase avec le mode fondamental de cœur est démontrée. Pour le capteur proposé, la dispersion anormale d'un mode guidé de coeur causée par une interaction forte avec un mode plasmonique en bordure de bande d'une fibre à bande photonique

interdite est démontrée. La nouvelle méthodologie de la détection des changements dans l'indice de réfraction de l'analyte par l'intermédiaire de la détection de changement de propagation d'impulsions courtes, est proposée.

Un capteur de type SPR entièrement fait de polymère est démontré dans les THz en mettant en scène un cœur poreux recouvert d'une fine couche ferroélectrique de PVDF en présence d'un analyte gazeux. Dans cette conception, nous profitons de la faible perte de la fibre poreuse proposée au chapitre 4 pour exciter le plasmon THz par un bon réglage de l'indice du mode de cœur de la fibre poreuse. Nous montrons que les deux méthodes de détection, celle basée sur l'amplitude et celle basée sur le régime spectral amènent à des sensibilités de l'ordre de $\sim 10^{-4} RIU$ sur le changement d'indice de réfraction de l'analyte gazeux. En outre, en directe analogie à la détection SPR dans le visible, l'existence de résonances plasmoniques en THZ permet l'étude de la dynamique des particules de la taille du micron dans une région de 10-60 μm à l'extérieur de la surface extérieure du capteur. Cela peut être d'un intérêt particulier pour la détection sans étiquette de bactéries spécifiques en fonctionnalisant la surface du capteur avec des phages spécifiques de certaines bactéries.

ABSTRACT

The global research objective of this thesis is to demonstrate design of novel compact and ultra-sensitive plasmonic sensors operating anywhere from the visible to the THz spectral ranges. The enabling technologies for such sensors are photonic bandgap and microstructured waveguides and fibers containing metallic inclusions. We achieve the stated global objective by systematically addressing several smaller problems. Firstly, this thesis demonstrates plasmonic excitation in metalized microstructured fibers in the context of bio-chemical sensing with enhanced microfluidics for visible and IR ranges. Furthemore, this basic design concept is generalized for the use with photonic bandgap fibers and waveguides; major advantages of using photonic bandgap waveguides in place of Total Internal Reflection (TIR) fibers for plasmonic sensing are discovered. Secondly, design criteria of a new type of low loss porous fiber operating in the THz regime is developed to be used in the body of a plasmonic-like sensor operating in THz spectral range. Thirdly, instead of metals, in THz regime we investigate the use of ferroelectrics, which we discover to be more suitable for supporting surface plasmons in this spectral range. The methods used and major results obtained in this thesis are summarized in the following.

In the first chapter, we discuss the theory of surface plasmons, surface plasmon excitation and sensing methodologies.

In the second chapter we show that using microstructured fibers one can solve much easier the problem of phase matching between the surface plasmon wave and fiber core mode, which is common when standard TIR fibers are used. Moreover, the use of microstructured fibers enables integration of the microfluidics and optics during drawing step thus simplifying considerably the sensor fabrication and operation. Furthermore, the different shapes of the metalized surface to enhance the plasmonic excitation were explored with an aim to enhance sensitivity.

In the third chapter, the design of photonic crystal waveguide-based surface plasmon

resonance sensor is proposed. By judicious design of a photonic crystal waveguide, the effective refractive index of a core mode can be made considerably smaller than that of the core material, thus enabling efficient phase matching with a plasmon, high sensitivity, and high coupling efficiency from an external Gaussian source, at any wavelength of choice from the visible to near-IR. This is, to our knowledge, not achievable by any other design. Moreover, unlike the case of total internal reflection waveguide-based sensors, a wide variety of material combinations can be used to design photonic crystal waveguide-based sensors as there is no limitation on the value of the waveguide core refractive index. Amplitude and spectral based methodologies for the detection of changes in the analyte refractive index were devised. Sensor resolution as low as $8.3 \cdot 10^{-6}$ RIU was found for aqueous analyte.

In the forth chapter, we propose two designs of effectively single mode porous polymer fibers for low-loss guiding of terahertz radiation. Designing of such a porous fiber, capable of having a low modal effective index, facilitates the phase matching of the fiber core mode and the plasmon waves bordering a low index analyte at Terahertz regime. As a first design we consider a fiber containing an array of subwavelength holes separated by sub-wavelength material veins. As a Second design, we consider a large diameter hollow core photonic bandgap Bragg fiber made of solid film layers suspended in air by a network of circular bridges. Numerical simulations of radiation, absorption and bending losses are presented; strategies for the experimental realization of both fibers are suggested. Emphasis is put on the optimization of the fiber geometries to increase the fraction of power guided in the air inside of the fiber, thereby alleviating the effects of material absorption and interaction with the environment. Total fiber loss of less than 10 dB/m, bending radii as tight as 3 cm, and fiber bandwidth of $\sim$ 1 THz is predicted for the porous fibers with sub-wavelength holes. Performance of this fiber type is also compared to that of the equivalent sub-wavelength rod-in-the-air fiber with a conclusion that suggested porous fibers outperform considerably the rod-in-the-air fiber designs. For the porous Bragg fibers total loss of less than 5 dB/m, bending radii as tight as 12 cm, and

fiber bandwidth of ~ 0.1 THz are predicted.

In the fifth chapter, THz plasmon-like excitation on top of a thin ferroelectric polyvinylidene fluoride (PVDF) layer covering solid-core polymeric Bragg fiber and facing liquid analyte is demonstrated theoretically. Thanks to the refractive index behavior of the ferroelectric PVDF layer we demonstrate new type of plasmonic-like excitations in THz regime which was impossible before while using metal layers in THz regime. In a view of designing a fiber-based sensor of analyte refractive index, phase matching of a THz plasmon-like mode with the fundamental core guided mode of a fiber is then demonstrated for the most challenging case of low refractive index analytes. Novel sensing methodology based on the core mode anomalous dispersion is proposed. Similarly to the Surface Plasmon Resonance sensors in the visible, we show the possibility of designing high sensitivity sensors in the THz regime with a resolution of $2 \cdot 10^{-4}$RIU in refractive index change.

In the sixth chapter, plasmon-like excitation at the interface between fully polymeric fiber sensor and gaseous analyte is demonstrated theoretically in terahertz regime. Such plasmonic excitation occurs on top of a $\sim 30\mu$m ferroelectric PVDF layer wrapped around a subwavelength porous polymer fiber. The major fraction of power guided in the air inside of the porous fiber alleviates the effects of material absorption and lowers the effective modal index to facilitate the plasmonic phase matching. In a view of designing a fiber-based sensor of analyte refractive index, phase matching of a plasmon-like mode with the fundamental core guided mode of a low loss porous fiber is then demonstrated for the challenging case of a gaseous analyte. We then demonstrate the possibility of designing high sensitivity sensors with amplitude resolution of $3.4 \cdot 10^{-4}$ RIU, and spectral resolution of $1.3 \cdot 10^{-4}$ RIU in THz regime. Finally, novel sensing methodology based on detection of changes in the core mode dispersion is proposed. As an advantage, in direct analogy to Surface Plasmon Resonance (SPR) sensing in the visible, existence of plasmon-like resonances in THZ can enable study of the micron-sized particle binding dynamics within 10 - 60 μm of the sensor surface. This can be of particular interest

for the label-free detection of specific bacteria by fictionalizing the sensor surface with bacteria specific phages. In comparison, SPR sensors in the visible can only detect binding of nano-molecules with sizes less than 100 nm (size of a plasmon tail), rendering the method insensitive to the larger particles, such as bacteria.

To summarize, in this thesis we present design methodologies of compact and ultra sensitive sensors of the analyte refractive index using microstructured and photonic crystal fibers. Design methodologies are presented for sensors in spectral ranges from the visible to THz. Performance of such novel plasmonic sensors are contrasted with that of plasmonic sensors based on standard TIR fibers. Major advantages of microstructured and PBG fiber-based sensors are discovered in sensitivity, ease of operation and portability.

CONDENSÉ EN FRANÇAIS

L'objectif principal de cette thèse est de démontrer la conception de nouveaux capteurs plasmoniques compacts et ultra sensibles couvrant un domaine spectral du visible jusqu'aux ondes THz. Cet objectif est atteint en considérant, d'une façon systématique, plusieurs sous catégories de l'objectif principal. D'abord, dans les chapitres 2 et 3, cette thèse démontre l'excitation plasmonique dans des fibres microstructurées TIR dont les trous sont revêtus d'un mince couche d'or opérant à titre de capteurs biochimiques à fonctions microfluidiques de même qu'un concept de capteurs plasmoniques basés sur des guides d'ondes à bande photonique interdite oeuvrant dans le visible et l'IR. Deuxièmement, dans le chapitre 4, nous développons le critère du design d'un nouveau type de fibre poreuse à faibles pertes dans le régime des THz qui doit être utilisée comme base d'un capteur plasmonique. Troisièmement, dans les chapitre 5 et 6, respectivement, nous proposons des critères de design de capteurs plasmoniques basés sur des fibres à bande photonique interdite et des capteurs plasmoniques basés sur des fibres poreuses à faibles pertes oeuvrant dans le régime des THz. Pour le régime des THz, nous considérons l'utilisation de ferroélectriques en remplacement des métaux et nous découvrons qu'ils sont susceptibles de supporter des plasmons de surface. Les méthodes utilisées et les principaux résultats obtenus dans cette thèse sont résumés, selon les chapitres, dans ce qui suit.

Dans le premier chapitre, nous expliquons la théorie, l'excitation et la méthodologie de la détection des plasmons de surface.

Dans le deuxième chapitre, nous introduisons la notion de capteur à résonance de plasmons de surface basés sur des fibres optiques microstructurées. Les deux principaux défis de la conception des capteurs ont été identifiés, c.à.d. la correspondance de la phase entre les modes guidés dans le cœur et les modes plasmoniques, et deuxièmement l'optimisation microfluidique pour permettre un écoulement efficace de la substance à analyser. La correspondance de phase a été facilitée par l'introduction d'une microstructure dans

le cœur de la fibre. Des fonctions microfluidiques étendues de la fibre. La sensibilité en amplitude du capteur pour mesurer des changements d'indice d'une substance à analyser à $0.65\mu m$ a été évaluée à $5 \cdot 10^{-5} RIU^{-1}$, en supposant qu'un changement de 1% constitue la limite de détection de l'amplitude. En interrogation spectrale, la limite inférieure de détection a été évaluée à $3 \cdot 10^{-5} RIU^{-1}$, en supposant une résolution de $0.1nm$ dans le déplacement du pic du plasmonique. Ces sensibilités sont comparables à celles des meilleurs capteurs basés sur des guides d'ondes et des fibres existants pour la mesure de substances aqueuses. De plus, les MOFs permettent le design de capteurs opérant à presque toute longueur d'onde dans le visible et l'IR proche grâce à leur capacité de supporter des modes à faible indice effectif. Les nombreux paramètres géométriques ajustables des MOFs permettent de faciliter l'obtention d'un accord de phase avec un mode plasmonique. Finalement, l'intégration de canaux microfluidiques pendant l'étirage des MOFs augmente la fiabilité des capteurs puisque aucune étape supplémentaire d'encapsulation microfluidique n'est nécessaire.

Dans le troisième chapitre, nous avons présenté une approche novatrice de design d'un capteur plasmonique basé sur un guide d'onde plan dans lequel le mode de cœur gaussien d'un guide effectivement unimodal est en phase à toute longueur d'onde désirée avec un plasmon de surface qui se propage à la jonction entre un revêtement métallique et le milieu diélectrique ambiant. La longueur d'onde d'opération de ces capteurs peut être ajustée arbitrairement dans une plage allant du visible au proche infrarouge. De plus, une grande variété de combinaisons de matériaux peut être utilisée pour concevoir de tels capteurs puisqu'il n'y a pas de contrainte sur la valeur d'indice de réfraction du cœur. Finalement, le degré de couplage entre les modes peut être varié en changeant le nombre de couches de réflecteur intermédiaires, qui déterminent aussi la longueur du capteur. La méthodologie de design de capteurs plasmoniques basés sur des guides à cristaux photoniques est plutôt générale et sa mise en œuvre peut s'appliquer à des guides plan, des fibres de Bragg ainsi que des fibres microstructurées. Plus particulièrement, il s'agit de d'abord déterminer une longueur d'onde d'opération λ_c. Ensuite, l'indice effectif du

plasmon $n_{eff}(\lambda_c)$ à λ_c est approximé par sa valeur théorique pour une interface métal-diélectrique planaire. Ensuite, la bande photonique interdite du guide d'onde réflecteur à λ_c est conçue de manière à être centrée près de $n_{eff}(\lambda_c)$. En faisant varier la taille du coeur du guide d'ondes (ou par variation de la géométrie du coeur), on peut déplacer la relation de dispersion d'un mode de cœur vers celle du mode plasmonique jusqu'à ce que la correspondance de phase se manifeste à λ_c. La longueur du capteur peut être modifiée par la variation du nombre de couches de réflecteur, davantage de réflecteurs résultant en un capteur plus long. Enfin, nous avons présenté des exemples de capteurs à SPR aqueux basés sur un guide d'onde à cristaux photonique, des fibres de Bragg à cœur solide ou liquide, ainsi que des fibres microstructurées à cristaux photoniques et cœur solide. La sensibilité en amplitude du design proposé était aussi élevé que $725 \cdot RIU^{-1}$. En supposant qu'un changement de 1% dans l'intensité de la transmission peut être détecté avec fiabilité, une résolution de mesure aussi élevée que $1.38 \cdot 10^{-5} RIU$ est démontrée. La sensibilité spectrale du design proposé est aussi élevée que $12000nm \cdot RIU^{-1}$. En supposant qu'un changement de $0.1nm$ dans la position du pic de plasmon peut être détectée avec fiabilité, une résolution de $8.3 \cdot 10^{-6} RIU$ est démontrée. Les longueurs du capteur dans nos exemples variaient d'une fraction de mm à $\sim 10cm$. Pour mesurer les changements dans l'analyte aqueux, la sensibilité de nos designs de fibres sont comparables ou même supérieures à celles des meilleurs capteurs à base de guide d'ondes existants (Homola et al., 1999).

Le quatrième chapitre de cette thèse est consacré à la conception de fibres poreuses à faibles pertes opérant dans le régime des Terahertz pour leur utilisation dans le corps d'un capteur plasmonique présenté au chapitre 6. Les longueurs d'onde correspondant au régime des terahertz couvrent l'intervalle $30 - 3000micron$ et ont un fort potentiel pour des applications dans la détection biomédicale ainsi que dans l'imagerie et la spectroscopie non invasives. Les sources térahertz sont généralement volumineuses, donc la conception de guides d'ondes THz efficaces pour la livraison et la collection à distance d'un rayonnement THz à large bande est une priorité pour de nombreuses ap-

plications pratiques de cette technologie. La complexité principale dans la conception de guides d'ondes THz est le fait que presque tous les matériaux sont très absorbants dans cette plage spectrale. Puisque la plus faible perte par absorption atteignable est dans l'air sec, des guides d'ondes efficaces doivent maximiser la fraction de puissance guidée dans l'air. Nous avons proposé deux types de fibres de plastique poreuses pour une guidance à faible perte de rayonnement THz. Ces fibres agissant comme un coupleur dans le corps d'un capteur THz plasmonique facilitent également l'excitation plasmonique dans le régime THz par un bon réglage de l'indice modal de cœur contrôlé par la densité de trous d'air. Dans ce cas, une fibre microstructurée THz de polymère contenant un cylindre avec une structure de trous d'air hexagonale a d'abord été discutée. Il faut souligner qu'une structure périodique de trous n'est pas nécessaire parce que le mécanisme de guidage reposte sur la réflexion totale interne, et non pas sur l'effet de bande photonique interdite. Bien que le diamètre du coeur de la fibre soit comparable à la longueur d'onde de fonctionnement, la majeure partie de flux THz lancé dans la fibre est confinée à l'intérieur des trous d'air situés dans le cœur de la fibre. Par conséquent, le couplage à l'environnement de la gaine est considérablement réduit, tandis qu'une perte par absorption modale inférieure à $10\ \mathrm{dB/m}$ peut être atteinte malgré une perte par absorption matérielle de $130\ \mathrm{dB/m}$. L'utilisation d'une expression approximative analytique pour calculer les pertes par macro-courbure, nous permet de conclure que les fibres poreuses suggérées sont très résistantes à la courbure, avec des pertes par courbures inférieures à la perte d'absorption modal même pour des courbures aussi serrées que $3\ \mathrm{cm}$ de rayon. Enfin, les fibres poreuses suggérées sont à large bande ayant une largeur de bande de ~ 1 THz même en présence de courbures serrées. Deuxièmement, nous avons considéré des fibres de Bragg poreuses à large bande photonique interdite fabriquées par des couches de matériau concentriques suspendues dans l'air à l'aide un réseau des ponts circulaires. Le diamètre de la fibre à cœur creux est beaucoup plus grand que la longueur d'onde d'opération, permettant ainsi un couplage efficace de diverses sources THz. Bien que les pertes totales modales (d'absorption et du rayonnement) plus

faibles que 5 dB/m puissent être atteintes avec une matériau qui a des pertes de volume de 130 dB/m, la bande passante de la fibre a été trouvé inférieure à 0.1 THz. Le couplage vers des états de surface parasites de la multicouche réflective facilité par les ponts de suspension a été déterminé être le principal mécanisme responsable de la réduction de la largeur de bande de la fibre de Bragg poreuse à bande photonique interdite.

Dans le cinquième chapitre, nous avons proposé des critères de conception d'une fibre de Bragg à cœur solide destinée à servir de capteur plasmonique à THz où l'excitation du plasmon THz sur un film mince de polymère de fluorure de Polyvinylidène (PVDF) par l'intermédiaire d'une correspondance de phase avec le mode fondamental de cœur est démontrée. Il faut souligner que dans le régime des THz, contrairement au régimes visible et infrarouge, la permittivité négative élevée des métaux proscrit fortement les champs électromagnétiques de pénétrer à l'intérieur du métal, et l'excitation des plasmons de l'interface métal/diélectrique devient difficile. Par conséquent, l'excitation efficace des plasmons à des fréquences plus basses exige un matériau artificiel, par exemple un réseau de fils métalliques 2D pour lequel les paramètres géométriques de la structure artificielle peuvent ajuster la fréquence de plasma des électrons du métal dans le régime de fréquence THz ou sub-THz. Grâce au comportement de l'indice de réfraction de la couche de fluorure de polyvinylidène ferroelectrique, nous avons ici la preuve d'un nouveau type d'excitation plasmonique dans le régime THz jamais démontré auparavant, même pour des couches de métaux étaient utilisées dans le régime THz. Le PVDF est un polymère ferroélectrique semi cristallin avec une permittivité de petite valeur absolue dans les régions du visible et de l'IR proche. Toutefois, dans une partie de la région THz, la longueur d'onde comprise entre 100 μm (3 THz) and 700 μm (0.43 THz), la partie réelle de l'indice de réfraction du PVDF est inférieure à 1, tandis que la partie imaginaire est positive et supérieure à 1. Par conséquent, la partie réelle de la constante diélectrique du PVDF est négative et, par analogie avec le comportement des métaux dans la région visible, la couche de PVDF est susceptible de supporter une excitation plasmonique. En outre, le PVDF donne une occasion de concevoir une structure polymérique pour dis-

positifs plasmoniques THz faisant appel à des techniques de production de masse bien implantées, telles que des micro-gaufrage et l'étirage des fibres, ce qui rend le processus de fabrication potentiellement très adapté à l'échelle industrielle. Pour le capteur proposé, la dispersion anormale d'un mode guidé de coeur causée par une interaction forte avec un mode plasmonique en bordure de bande d'une fibre à bande photonique interdite est démontrée. La nouvelle méthodologie de la détection des changements dans l'indice de réfraction de l'analyte par l'intermédiaire de la détection de changement de propagation d'impulsions courtes, est proposée. Enfin, la résolution du capteur à base amplitude sur aussi peu que $2 \cdot 10^{-4}$ RIU est démontré dans le régime THz, avec une longueur de capteur à d'environ 1 cm.

Dans le sixième chapitre, un capteur de type SPR entièrement fait de polymère est démontré dans les THz en mettant en scène un cœur poreux recouvert d'une fine couche ferroélectrique de PVDF en présence d'un analyte gazeux. Dans cette conception, nous profitons de la faible perte de la fibre poreuse proposée au chapitre 4 pour exciter le plasmon THz par un bon réglage de l'indice du mode de cœur de la fibre poreuse. L'excitation plasmonique à l'interface PVDF/air peut être obtenue par le mode de cœur de la fibre quand la correspondance de la phase est satisfaite. D'une façon similaire aux capteurs optiques SPR, le mode guidé dans le cœur présente un pic prononcé de pertes au point de correspondance de phase avec un mode plasmonique. En outre, la dispersion du mode de cœur varie considérablement dans la même région de correspondance de phase. En détectant des changements dans la longueur d'onde d'accord de phase en raison des changements d'indice de réfraction de l'analyte, des systèmes de détection hautement sensibles sont possibles. Nous montrons que les deux méthodes de détection, celle basée sur l'amplitude et celle basée sur le régime spectral amènent à des sensibilités de l'ordre de $\sim 10^{-4} RIU$ sur le changement d'indice de réfraction de l'analyte gazeux. En outre, en directe analogie à la détection SPR dans le visible, l'existence de résonances plasmoniques en THZ permet l'étude de la dynamique des particules de la taille du micron dans une région de 10-60 μm à l'extérieur de la surface extérieure du capteur. Cela peut

être d'un intérêt particulier pour la détection sans étiquette de bactéries spécifiques en fonctionnalisant la surface du capteur avec des phages spécifiques de certaines bactéries. En comparaison, les capteurs SPR dans le visible peuvent détecter seulement des nano-molécules avec des tailles de moins de 100nm (taille d'une onde évanescente de plasmon), ce qui rend la méthode insensible aux particules plus grosses, comme les bactéries. La déposition de couches métalliques à l'intérieur de fibres optiques microstructurée a été récemment signalée, soit sous haute pression avec la technique " Chemical Vapor Deposition " (CVD) (Sazio et al., 2006) ou par la technique de déposition à chimie humide utilisé dans la fabrication de guides d'ondes creux recouverts de métal (Harrington, 2000). Comme première suggestion, il est possible de fabriquer des couches et de les revêtir de métal pour la fabrication des fibres microstructurées proposées, ce qui contribuera à démontrer expérimentalement les performances de détection de ce type de capteurs.

La deuxième suggestion est de fabriquer la fibre poreuse de polymère à faibles pertes opérant dans les THz que nous avons proposée, ce qui est poursuivi actuellement par certains étudiants de notre groupe. Le facteur déterminant pour le développement des fibres poreuses toutes diélectriques est que ces fibres peuvent être fabriquées à partir d'un seul matériau en utilisant des techniques d'étirage de fibres, qui sont, potentiellement, plus simple que la fabrication de guides d'ondes à revêtement métallique en raison de l'omission de l'étape de revêtement.

TABLE OF CONTENTS

LIST OF FIGURES

LIST OF NOTATIONS AND SYMBOLS

ABBREVIATIONS

RIU:	refarctive index unit
MOF:	microstructured optical fiber
SPR:	surface plasmon resonance
TIR:	total internal reflection
IR:	infrared
PBG:	photonic band gap
PVDF:	polyvinylidene fluoride
THz:	terahertz

NOTATIONS

λ:	wavelength in vacuum
ω:	angular frequency
$\mathbf{k}$:	wave number
β:	modal parameter
n_{eff}:	effective modal index
d_i:	thickness of a layer of reflector i
n_i:	real part of the index of refraction of a layer of reflector i
ϵ_i:	permittivity of a dielectric layer of i
$\mathbf{S_z}$:	Poynting vector
N:	number of layers in the reflector
α:	transmission loss of a guided mode
P_0:	power injected at $z = 0$
L:	length of the device
S:	refractometry sensitivity
T:	transmittance

Λ:	Pitch of a microstructured fiber
d:	the diameter of holes of a microstructured fiber
d_c:	the diameter of holes inside of the core of fiber
E:	electrical field
H:	magnetic filed
t:	time
ϵ:	the permittivity of material
d_{bio}:	the thickness of biolayer
n_{bio}:	the index of biolayer
$n_{analyte}$:	the index of analyte

INDICES

d:	dielectric
l,h:	low index layer (l) and high index layer (h)
a:	on the analyte
$H2O$:	on the aqueous sample
$gold$:	on the gold layer
Au:	on the layer
Si:	on the silicon substarte
∞:	on the Drude model
p:	on the Drude model, resonance plasma
t:	on the Drude model, parameter t
A:	on the sensitivity, amplitude
M:	on the sensitivity, maximum
λ:	on the sensitivity, spectral
$peak$:	on the losses, upper limit

LIST OF TABLES

INTRODUCTION

In the visible and ultraviolet spectral ranges, the collective oscillation of the free charge carriers at a metal/dielectric interface yields a surface plasmon wave propagating along the surface of the metal. Surface plasmons (Agranovich and Mills, 1982) are extremely sensitive to changes in the refractive index of the dielectric. This feature constitutes the core of many Surface Plasmon Resonance (SPR) sensors. Typically, these sensors are implemented in the Kretschmann-Raether prism geometry to direct p-polarized light through a glass prism and reflect it from a thin metal (Au, Ag) film deposited on the prism facet (Kretschmann and Raether, 1968). The presence of a prism allows resonant phase matching between an incident electromagnetic wave and a high-loss plasmonic wave at the metal/analyte interface for a specific combination of the angle of incidence and wavelength. By detecting changes in the amplitude or phase of the reflected light due to its coupling with a plasmon wave, one can detect minute changes in the refractive index of an analyte bordering the metal layer. Since the plasmon excitation condition resonantly depends on the value of the refractive index of an ambient medium within 100 - 300 nm from the interface, the method enables detection of biological binding events on the metal surface with unprecedented sensitivity (Kretschmann and Raether, 1968). The course of a biological reaction can then be followed by monitoring angular (Liedberg et al., ; Melendez et al., 1996), spectral (Zhang and Uttamchandani, 1988) or phase (Kabashin and Nikitin, 1998; Grigorenko et al., 1999) characteristics of the reflected light. However, the high cost and large size of commercially available systems makes them useful only in a laboratory, while many important field and other applications remain out of the reach of this method. Using optical fibers instead of a prism in plasmonic sensors offers miniaturization, high degree of integration and remote sensing capabilities. Over the past decade, driven by the need to miniaturize of SPR sensors, various compact configurations enabling coupling between optical waveguide modes

and surface plasmonic waves have been investigated. Among others, metallized single-mode, polarization maintaining, and multi-mode waveguides, metallized tapered fibers, and metalized fiber Bragg gratings have been studied (Jorgenson and Yee, 1993; Vidal et al., 1993; Alonso et al., 1993; Alonso et al., 1994; Homola, 1995; Trouillet et al., 1996; Tubb et al., 1997; Homola et al., 1997b; Slavik et al., 1998; Diez et al., 2001; Piliarik et al., 2003; Monzón-Hernández et al., 2004; Monzon-Hernandez and Villatoro, 2006; Suzuki et al., 2006; Ctyroky et al., 1999a; Trouillet et al., 1996; Weisser et al., 1999; Gupta and Sharma, 2005). Moreover, recently, SPR excitation by a tilted fiber Bragg grating is proposed (Shevchenko and Albert, 2007). The surface plasmons in this fibers are excited by the excited fiber cladding modes which are very sensitive to environment temperature. On the other hand, in this fibers a small part of light power is propagating by a cladding mode, resulting in weak plasmon excitation and refractometry sensitivity. Finally, the control of excitation of a specific cladding mode is difficult and excitation of several cladding modes leads to several plasmonic excitations, which is a source of noise in these sensors.

In the following, the four principal difficulties hindering the development of the integrated waveguide-based SPR sensors, at either visible or THz frequencies, have been identified. The first two problems affect the SPR sensors operating in the visible and IR range, while the third and forth problems influence the waveguide SPR sensors designed for the THz range.

First challenge is phase matching of a waveguide core mode and a plasmonic wave. Mathematically, phase matching constitutes equating the effective refractive indexes of the two modes at a given wavelength of operation. In the case of a single mode waveguide effective refractive index of its core mode is close to that of a core material. For most practical core materials their refractive index is higher than 1.45. Effective refractive index of a plasmon is typically close to that of a bordering analyte, which in the case of air is ~ 1.0, while in the case of water is ~ 1.33. Only at higher frequencies (λ<700 nm

for a plasmon on a gold metal film, for example) does the plasmon refractive index become high enough to match that of a waveguide core mode (Homola, 1995; Homola et al., 1997b). From a sensor design point of view, it is quite unsatisfactory to be limited by the values of the material refractive indices even without the ability of compensating material limitations with a judicious choice of a sensor geometry. In principle, the phase matching problem can be alleviated by coupling to a plasmon via the high order modes of a multimode waveguide (Ctyroky et al., 1999a; Trouillet et al., 1996; Weisser et al., 1999; Gupta and Sharma, 2005). Such modes can have significantly lower effective refractive indices than a waveguide core index. In such a set-up light has to be launched into a waveguide in such a way as to excite high order modes, some of which will be phase matched with a plasmon mode. As only a fraction of higher order modes are phase matched to a plasmon, only a fraction of total launched power will be coupled to a plasmon, thus reducing sensor sensitivity. Moreover, as power distribution in high order modes is very sensitive to the launching conditions this adds additional noise due to variations in the coupling setup.

The second problem that limits the development of the waveguide based plasmonic sensors is that of packaging the microfluidics setup, waveguide and metallic layers into a single sensor. For example, in traditional single mode fiber based sensors, to metallize fiber surface one has to first strip the fiber jacket and then polish the fiber cladding almost to the core in order to enable evanescent coupling with a plasmon. This laborious procedure compromises fiber integrity making the resulting sensor prone to mechanical failures. Integration of a metallized fiber piece into a microfluidics setup presents yet another additional step in sensor fabrication, thus increasing the overall fabrication cost.

In the case of waveguide-based SPR sensors in the THz regime, the third challenge is designing a low loss waveguide with tunable modal effective index. The main complexity in designing THz waveguides is the fact that almost all materials are highly absorbent in the THz region. Since the lowest absorption loss occurs in dry air, an efficient wave-

guide design must maximize the fraction of power guided in the air. For instance, hollow core metallic waveguides, such as those conventionally used to guide microwaves, were shown to have 5 dB/cm loss at 1 THz (McGowan et al., 1999). However, metals, like stainless steel, are not efficient reflectors in the THz regime because of their finite conductivity, which leads to appreciable waveguide losses. On the other hand, many groups have studied a wide variety of dielectric waveguides such as plastic solid core holey fibers (Han et al., 2002; Goto et al., 2004), Bragg bandgap fibers (Skorobogatiy and Kabashin, 2007), subwavelength plastic fibers (Chen et al., 2006), and low index discontinuity waveguides (Nagel et al., 2006). These studies have again shown that, even when using relatively low absorption loss plastics or glasses, the waveguide absorption loss remains substantial unless a considerable fraction of power is guided in the air. Thus, to design a waveguide based plasmonic sensors operating at THz frequencies, one needs to first design a very highly low loss fiber guiding in THz regime with a designable modal index suitable for plasmonic excitations.

The forth problem, that prevents plasmonic excitation in THz regime, is the large negative permittivity of metals at THz frequencies strongly prohibits electromagnetic fields from penetrating inside a metal. Thus plasmon excitations on the metal/dielectric interface become challenging. The solution for efficient plasmonic excitation at lower frequencies has, until now, been to design an artificial material, for example a 2D subwavelength metallic wire lattice, for which the geometrical parameters of the artificial structure can tune the electron plasma frequency of metal to the THz or sub-THz frequency range (Pendry et al., 1996; Pendry et al., 1998). The procedure of designing an artificial material and integrating it with other components in the body of a sensor makes the design of a THz plasmonic sensor very complex and sometimes impossible from the sensor fabrication point of view.

The main objective of this thesis is to design novel, compact, and ultra-sensitive microstructured optical fiber (MOF) based SPR sensors operating anywhere from the visible

to the THz spectral range. This main objective is divided to two objectives that are: a) design of MOF based SPR sensors operating at visible and IR, b) design of MOF based SPR like sensors operating at THz.

At the first objective, we aim to design MOF-based plasmonic sensors operating at visible and IR. The strategy here is to use MOFs, for first time, instead of convectional fibers in the body of plasmonic sensor to enhance the refractometry sensitivity, microfluidic characteristics and probe depth of SPR sensors. We are interested in these type of sensors because they have the potential of being very sensitive to both the thickness of biolayers constituting of viruses, bacterizes and DNAs as well as the index change of analytes. Moreover, these miniaturized sensors based on MOFs can be design to have an improved microfluidic characteristics allowing these sensors to be more easily integrated into a chip than other SPR sensors. Thus the prospective application of these type of sensors can be a very sensitive remote biosensor. Furthermore, these type of biosensor have a potential to be integrated into a body of a wireless remote devices to transfer the output of the sensor during measurement. Besides, MOF based plasmonic sensors can operate at longer wavelength, i.e. $\sim 1\,\mu$m instead of $\sim 0.6\,\mu$m, resulting in a more detection depth for the sensors, for instant, $\sim 1\,\mu$m; this detection depth is $\sim 3-10$ times more than that of the usual waveguide based plasmonic sensors operating at visible, thus enabling the detection of bigger size viruses and bioparticles.

Our second objective is to introduce and design the first polymeric MOF-based plasmonic-like sensors operating at THz. The design and development of these type of sensors at THz face two main problems which are finding materials, which naturally support SPR at THz regime and design a low loss waveguide with tunable modal effective index. By addressing solutions for these limitations, we aim to design and propose fully polymeric MOF based plasmonic-like sensors at THz for refractometry and bio-layer sensing. We are interested in design of plasmonic like sensors at THz because the operating wavelength of these sensors are more than 300 times longer than that of the SPR sensors at

visible and IR, resulting in at least $\sim$200 times longer probe depth for the sensor. This enables the detection of biolayers composed of macromolecules and bacterial with size of $\sim 1-100\ \mu$m, which is impossible at visible - IR operating wavelength range.

We achieve the stated two objectives by systematically addressing solutions to the four challenges previously mentioned. In general, we propose two categories of solutions: a) solutions for the problem that SPR sensors face at visible and IR, b) solutions for problem that SPR sensors face at THz.

The first category of solution, presented in chapter 2 and 3, proposes using MOFs instead of the conventional fibers in the body of waveguide-based SPR sensors. Microstructured fibers are usually made of only one dielectric, such as glass or polymer, with porous cladding containing periodic arrays of air holes to lower and tune the fiber cladding index. Here, the motivation for using MOFs is that the choice of the geometry and size of the holes in these fibers enables tuning the modal propagation constant of the fiber more conveniently than that of conventional fibers. Furthermore, the surface of holes can be metal plated for plasmonic excitation; this gives two opportunities of having metalized surface with different shape and improvement the microfluidic characteristics of sensors. Another freedom is the microstructured fibers can be designed to guide light by Total Internal Reflection (TIR), studied in chapter 3, or Photonic Band Gap (PBG) mechanism, studied in chapter 4. We are also motivated to demonstrate that the PBG MOFs enable the MOF based SPR sensors to operate at IR range (1 μm instead of 0.6 μm), which means higher sensitivity and probe depth for the waveguide based SPR sensors, which was impossible while using the conventional fibers.

The second category, presented in chapter 4 to 6, addresses solutions for the two main difficulties for the design of THz MOF based SPR-like sensors, which are naturally plasmonic excitation and design of low loss waveguide at THz. Low loss THz waveguide design difficulty can be solved with introducing subwavelength holes inside a dielectric

rod to confine light inside air holes instead of material, presented in chapter 4, resulting in decreasing absorption and bending loss. To solve the plasmon excitation difficulty at THz we find a ferroelectric polymer which support surface plasmon at THz and simulate the plasmonic excitation on top of that polymeric film, and eventually we design two SPR sensors at THz regime operating at 280 μm and 300 μm, presented in chapter 5 and 6 respectively.

This thesis consist of the theory overview, 5 articles, and a conclusion chapter. Chapter one is devoted the description of the fundamental theory behind surface plasmon waves, the means of plasmon excitation and the sensing methodologies used in plasmonic sensing.

In chapter 2, we present design strategies for the MOF based SPR sensors by proposing two designs for MOF based SPR sensors where the MOFs guiding based on TIR. In the first TIR MOF based SPR sensor, the fiber core is surrounded by the two layers of holes. Metallized holes in the second layer are considerably larger than these in the first layer, thus simplifying the flow of analyte through them. In the second MOF based SPR sensor, two large semi circular channels covered with metal are used to further enhance microfluidic flow. Another reason for the introduction of the two structures is to study the effect of metallic surface geometry on the efficiency of plasmonic excitation. In each sensor, plasmons on the inner surface of the metallized channels or holes containing an analyte can be excited by the fundamental mode of the single mode MOF. We have identified two main sensor design challenges which are the phase matching between the core guided and plasmonic modes, and microfluidics optimization to enable efficient analyte flow. Phase matching was facilitated by introducting of an air hole into the fiber core. In general, by adjusting many of the MOF geometrical parameters it is considerably simpler to enforce phase matching with a plasmon compared to the standard TIR waveguides and fibers. Improved microfluidics here is addressed by the integration of large analyte filled channels adjacent to the fiber core. Moreover, integration of the microfluidic channels

during MOF drawing increases sensor reliability as laborious extra step of microfluidics packaging is avoided. The maximum sensitivity for measuring index changes in the aqueous analyte at $0.65\mu m$ is calculated to be $5 \cdot 10^{-5}$ RIU (Refractive Index Unit) at the amplitude-based mode and $3 \cdot 10^{-5}$ RIU at the wavelength interrogation mode. These range of sensitivities are comparable to the ones of the best existing standard fiber and waveguide-based sensors optimized for aqueous analytes (Homola et al., 1999).

In the chapter 3, we propose the design criteria for PBG waveguide based surface plasmon sensors. This sensor design concept is implemented using solid and hollow core Bragg fibers, as well as PBG microstructured fibers. In these sensors the plasmon waves on the surfaces of a thin metal film inside of a hole are excited by a Gaussian-like leaky mode of an effectively single mode PBG waveguide. The most important advantage of using the PBG waveguide in the body of a SPR sensors is that the effective refractive index of the waveguide core mode can be made considerably smaller than that of the core material, thus enabling efficient phase matching with a plasmon, high sensitivity, and high coupling efficiency from an external Gaussian source, at any wavelength of choice from the visible to near-IR. To our knowledge, this is not achievable by any other design. The sensors operating at the near-IR ~ 1 μm have a larger the depth of filed ~ 1 μm with respect to the ones operating at visible $\sim 100 - 300$ nm, resulting in detecting bioparticles with bigger size. Moreover, unlike the case of TIR fiber or waveguide-based sensors, a wide variety of material combinations can be used to design PBG waveguide-based sensors as there is no limitation on the value of the waveguide core refractive index. In addition, coupling strength between the waveguide core and plasmon modes can be varied by changing the number of the intermediate reflector layers, which also permits designing the overall sensor length. The maximum sensitivity for measuring index changes in the aqueous analyte is calculated to be $1.38 \cdot 10^{-5}$ RIU at the amplitude-based mode and $8.3 \cdot 10^{-6}$ RIU at the wavelength interrogation mode. Sensor lengths in our examples varied from sub-mm to ~ 10 cm. For measuring changes in the aqueous ana-

lyte, sensitivities of our fiber designs are comparable to or even surpass those of the best existing waveguide-based sensor designs (Homola et al., 1999).

In chapter 4, 5, and 6, we address to solutions for difficulties hindering the design of THz waveguide based plasmonic sensors. Notice that THz waveguide based plasmonic sensors have not been reported before, and in analogy to the waveguide plasmonic sensors we have introduced these type of sensors here.

In chapter 4, we propose two designs of effectively single mode porous polymer fibers for low-loss guiding of terahertz radiation. The proposed novel low loss waveguide structures also enable tuning of the modal effective index of the core mode, thus facilitating the phase matching of the core mode and plasmon waves bordering a low index analyte. Thus, we are addressing solutions for phase matching and low loss guiding for plasmonic sensors at the THz regime. First, we present a fiber of several wavelengths in diameter containing an array of sub-wavelength holes separated by sub-wavelength material veins. Second, we detail a large diameter hollow core PBG Bragg fiber made of solid film layers suspended in air by a network of circular bridges. Numerical simulations of radiation, absorption and bending losses are presented; strategies for the experimental realization of both fibers are suggested. Emphasis is put on the optimization of the fiber geometries to increase the fraction of power guided in the air inside of the fiber, thereby alleviating the effects of material absorption and interaction with the environment. Total fiber loss of less than 10 dB/m, bending radii as tight as 3 cm, and fiber bandwidth of $\sim$ 1 THz is predicted for the porous fibers with sub-wavelength holes. Performance of this fiber type is also compared to that of the equivalent sub-wavelength rod-in-the-air fiber with a conclusion that suggested porous fibers outperform considerably the rod-in-the-air fiber designs. For the porous Bragg fibers total loss of less than 5 dB/m, bending radii as tight as 12 cm, and fiber bandwidth of $\sim$ 0.1 THz are predicted. Coupling to the surface states of a multilayer reflector, facilitated by the material bridges, is determined as the primary mechanism responsible for the reduction of the bandwidth of a porous

Bragg fiber. However, both proposed fibers are in the category of highly low loss fiber in the THz regime, in chapter 6 we choose the porous sub-wavelength fiber in the design of THz waveguide-based plasmonic sensor because of the following reasons: a) the Bragg fiber has smaller bandwith compared to the porous sub-wavelength holes fiber, b) tuning the modal refractive index in the porous sub-wavelength fiber is much easier than that of Bragg fiber, c) the fabrication of the porous sub-wavelength is easer.

In chapter 5, THz plasmon-like excitation on top of a thin ferroelectric PVDF layer, covering solid-core polymeric Bragg fiber and facing a liquid analyte, is demonstrated theoretically. We discuss the fact that the refractive index behavior of the ferroelectric PVDF layer demonstrates a new type of plasmonic-like excitation in THz regime which was impossible when using metal layers (Hassani et al., 2008d; Hassani and Skorobogatiy, 2008). PVDF can be electrically poled to convert to a ferroelectric semi-crystalline polymer with the real part of the refractive index less than one, while the imaginary part is positive and mostly larger than one, in the wavelength range between 100 μm (3 THz) and 700 μm ($\sim$ 0.43 THz). Therefore, the real part of the PVDF dielectric constant is negative, and by analogy with the behavior of metals in the visible range, PVDF layer is expected to support a plasmon-like excitation. Moreover, PVDF gives an opportunity to design a fully polymeric structure for THz plasmonic devices using such established mass production techniques as fiber drawing, which potentially makes the fabrication process highly suitable for the industrial scale-up. In a view of designing a fiber-based sensor of analyte refractive index, phase matching of a THz plasmon-like mode with the fundamental core guided mode of the solid core bragg fiber is then demonstrated for the refractive index analytes $n_a = 1.33$. Although, the solid bragg fiber is lossy for THz range, in analogy to the visible range, having the Bragg fiber in the body of the sensor is intuitive because of the presence of Bragg reflectors which enables the tuning of the effective reflective index of the core mode for efficient plasmon exciation in the THz range. In conclusion, similarly to the Surface Plasmon Resonance sensors in the visible,

we show the possibility of designing high sensitivity sensors in the THz regime with a resolution of $2 \cdot 10^{-4}$ RIU in refractive index change.

In chapter 6, plasmon-like excitation at the interface between a fully polymeric fiber sensor and gaseous analyte is demonstrated theoretically in the terahertz regime. Such plasmonic excitation occurs on top of a $\sim 30\,\mu$m ferroelectric PVDF layer wrapped around a subwavelength porous polymer fiber. In a view of designing a fiber-based sensor of analyte refractive index, phase matching of a plasmon-like mode with the fundamental core guided mode of a low loss porous fiber, introduced in the chapter 4, is then demonstrated for the challenging case of a gaseous analyte. Worth mentioning that the sub-wavelength porous fiber not only provides a low loss guiding mechanism for the core mode but also decrease the modal effective refractive index of the core mode to the degree that phase matching between the core mode and THz surface plasmons bordering a gaseous analyte makes possible. We then demonstrate the possibility of designing high sensitivity sensors with amplitude resolution of $3.4 \cdot 10^{-4}$ RIU, and spectral resolution of $1.3 \cdot 10^{-4}$ RIU in the THz regime. Furthermore, the novel sensing methodology based on detection of changes in the core mode dispersion is proposed. In direct analogy to SPR sensing in the visible, existence of plasmon-like resonances in THz can enable study of the micron-sized particle binding dynamics within $10-60\ \mu$m of the sensor surface. This can be of particular interest for the label-free detection of specific bacteria by functionalizing the sensor surface with bacteria specific phages. In comparison, SPR sensors in the visible can only detect binding of nano-molecules with sizes around $100-300$ nm (size of a plasmon tail), rendering the method insensitive to the larger particles, such as bacteria.

In the final chapter, we summarize the result and methodologies presented in the thesis. Finally, we also present the outline of our future research plans. The list of papers I have contributed to during my PhD study is in the following.

Journal papers

A. Hassani, M. Skorobogatiy, "Surface plasmon resonance-like integrated sensor at terahertz frequencies for gaseous analytes," Opt. Express, Vol. 16, pp. 20206-20214 (2008)

A. Hassani, A. Dupuis, and M. Skorobogatiy, "Surface Plasmon Resonance-like fiber-based sensor at terahertz frequencies," J. Opt. Soc. Am. B, Vol. 25, pp. 1771-1775 (2008).

A. Hassani, A. Dupuis, and M. Skorobogatiy, "Porous polymer fibers for low loss THz guiding," Opt. Express, vol. 16, pp. 6340-6351 (2008).

A. Hassani (invited paper), B. Gauvreau, M. Fassi Fehri, A. Kabashin, and M. A. Skorobogatiy, "Photonic crystal fiber and waveguide-based Surface Plasmon Resonance sensors for applications in the visible and near-IR," Electromagnetics, Special Issue is Surface Waves and Complex Mediums, Vol. 28, pp. 198-213 (2008).

A. Hassani, A. Dupuis, and M. Skorobogatiy, "Low Loss Porous Terahertz Fibers Containing Multiple Subwavelength Holes," Appl. Phys. Lett, vol. 92, 071101 (2008).

A. Dupuis, N. Guo, B. Gauvreau, **A. Hassani**, E. Pone, F. Boismenu, and M. Skorobogatiy, "Guiding in the visible with "colorful" solid-core Bragg fibers," Opt. Lett., vol. 32, 2882-2884 (2007).

B. Gauvreau, **A. Hassani**,M. Fassi Fehri, A. Kabashin, and M. A. Skorobogatiy, "Photonic bandgap fiber-based Surface Plasmon Resonance sensors," Opt. Express, vol. 15, 11413-11426 (2007).

E. Pone, **A. Hassani**, S. Lacroix, A. Kabashin, and M. Skorobogatiy, "Boundary integral method for the challenging problems in bandgap guiding, plasmonics and sensing," Opt. Express, Vol. 15, 10231-10246 (2007).

A. Hassani, M. Skorobogatiy, "Design criteria for the Microstructured Optical Fiber-

based Surface Plasmon Resonance sensors," J. Opt. Soc. Am. B, Vol. 24, 1423-1429 (2007).

A. Hassani, E. Pone, M. Skorobogatiy, "Heating of microstructured optical fibers due to absorption of the propagating light," J. Opt. Soc. Am. B, Vol. 24, pp. 756-762 (2007).

A. Hassani, M. Skorobogatiy "Design of the microstructured optical fiber-based surface plasmon resonance sensors with enhanced microfluidics," Opt. Express, vol. 14, pp. 11616-11621 (2006)

Conference Proceeding

A. Hassani, M. Skorobogatiy, "Ferroelectric PVDF-Based Surface Plasmon Resonance-Like Integrated Sensor at Terahertz Frequencies for Gaseous Analytes," CMI6, CLEO 2009.

A. Dupuis, **A. Hassani**, M. Skorobogatiy, "Design and Fabrication of Subwavelength THz Fibers with Multiple Holes," CThQ6, CLEO 2009.

A. Hassani, A. Dupuis, M. Skorobogatiy, "Highly porous plastic fibers for low-loss Terahertz guiding," European Optical Society Annual Meeting, Paris, France (EOSAM), Topical Meeting on Terahertz Science and Technology-TOM 2, 2008

A. Hassani, A. Dupuis, M. Skorobogatiy, "Surface Plasmon Resonance-like fiber sensors in terahertz," EOSAM,TOM 2, France, 2008

A. Hassani, B. Gauvreau, M. Skorobogatiy, "Novel Photonic Crystal Fiber Sensors Using Splitting of a Degenerate Plasmonic Doublet," CMJ1,CLEO, USA, 2008

E. Pone, **A. Hassani**, S. Lacroix, M. Skorobogatiy, "A Pressure Sensor Based on the Loss Birefringence of a Microstructured Optical Fiber Containing Metal Coated Elliptical

Inclusions" CMZ3,CLEO, USA, 2008

A. Dupuis, N. Guo, B. Gauvreau, **A. Hassani**, E. Pone, F. Boismenu, M. Skorobogatiy, "Colorful" Solid-Core Bragg Fibers Guiding in the Visible," CTuMM2,CLEO, USA 2008

A. Hassani, A. Dupuis, M. Skorobogatiy, "Low Loss THz Fibers with Multiple Subwavelength Holes," JWA47,CLEO, USA, 2008

A. Dupuis, N. Guo, B. Gauvreau, **A. Hassani**, E. Pone, F. Boismenu, M. Skorobogatiy, "All-Fiber Spectral Filtering with Solid Core Photonic Band Gap Bragg Fibers," OFC, OThM3, USA, 2008. Technical Digest

E. Pone, **A. Hassani**, S. Lacroix, M. Skorobogatiy, "Accurate Modal Analysis of Microstructured Optical Fibers with the Boundary Integral Method," OFC, OThR5, USA, 2008. Technical Digest.

Invited Talk: A. Dupuis, **A. Hassani**,M. Skorobogatiy, N. Guo, "Photonic crystal fibers for THz applications," SPIE Photonics West, Paper 6892-51, Ultrafast Phenomena in Semiconductors and Nanostructure Materials XII, Conference 6892, 2008.

A. Hassani, B. Gauvreau, M. Fassi Fehri, A. Kabashin, M. Skorobogatiy, "Photonic bandgap fiber-based Surface Plasmon Resonance sensors," Workshop on Nanophotonics and Plasmonics, Sao Paolo, Brazil 2007.

E. Pone, **A. Hassani**, M. Skorobogatiy, "Loss birefringence of a Microstructured Optical Fiber containing metal coated elliptical inclusions. Prospective in pressure sensing," Workshop on Nanophotonics and Plasmonics, Sao Paolo, Brazil 2007.

A. Hassani, M. Skorobogatiy, "Practical Design of Microstructured Optical Fibers for Surface Plasmon Resonance Excitation," CLEO, Section: Microstructured Fibers and

Applications, CWO4, May 6-11, 2007, Baltimore, Maryland, USA.

A. Hassani, M. Skorobogatiy, "Practical Design of Microstructured Optical Fibers for Surface Plasmon Resonance Sensing," Optical Fiber Communication Conference (OFC), OThA5, 2007. Technical Digest. March 25-29, 2007, Anaheim, California, USA.

CHAPITRE 1

THEORY OF SURFACE PLASMON SENSORS

1.1 Introduction

In this chapter, we first start with the theory of surface plasmon waves and then discuss the excitation of surface plasmons using light. Then, design methodologies and various surface plasmon based sensing methodologies for MOF based SPR sensors are discussed. To simplify our presentation we consider two particular examples of the microstructured fiber-based plasmonic sensors.

1.2 Electromagnetic theory of surface plasmons

The coherent fluctuation of the density of surface electrons excited by electromagnetic fields produces the surface plasmon waves, propagating along a metal/dielectric interface. The propagation of the Surface Plasmon Resonance (SPR) waves on a metallic film can be fully described by solution of the Maxwell's equations and applying the electromagnetic boundary conditions at the metal/dielectric interface (Raether, 1988).

To discuss the solution of the Maxwell's equation for surface plasmons, Consider two semi-infinite spaces divided by the horizontal plane $z = 0$, shown in Fig. 1.1, where the upper ($z \geq 0$) and lower ($z \leq 0$) half-spaces are respectively occupied by dielectric and metal. The electrical fields in the dielectric and metal can be respectively described as:

$$E = E_0^d \exp[i(k_x - \omega t)] \exp(-ik_z^d) \tag{1.1}$$

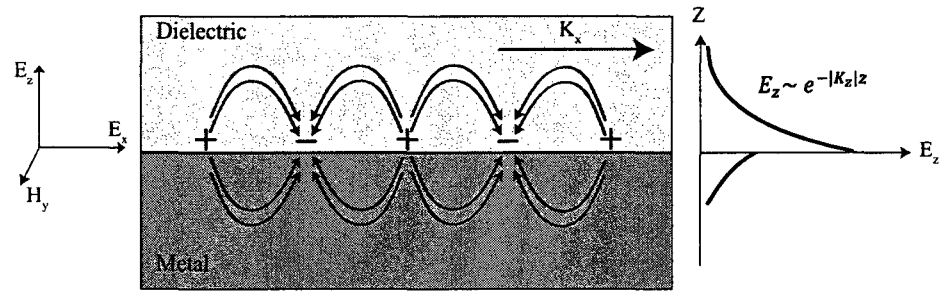

FIG. 1.1 – *The schematic of the filed distribution of the p-polarized surface plasmon propagating at the metal/dielectric interface.*

and

$$E = E_0^m \exp[i(k_x - \omega t)] \exp(ik_z^m), \tag{1.2}$$

where d and m correspondingly indicate the permittivities of the dielectric, having a real permittivity ε_d, and metal, having a complex permittivity $\varepsilon_m = \varepsilon_m^r + i\varepsilon_m^i$.

Here k_z^d and k_z^m are the wave vectors perpendicular to the metal/dielectric interface described by

$$z \geq 0 \qquad k_z^d = [\varepsilon_d(\frac{\omega}{c})^2 - k_x^2]^{1/2} \tag{1.3}$$

and

$$z \leq 0 \qquad k_z^m = [\varepsilon_m(\frac{\omega}{c})^2 - k_x^2]^{1/2}. \tag{1.4}$$

The wave vectors k_z^d and k_z^m effectively define the penetration depth of the surface plasmons. Indeed, the field amplitude of the surface plasmons decay exponentially from the metal/dielectric interface in dielectric and metal as $\exp(-|K_z^d||z|)$ and $\exp(-|K_z^m||z|)$, respectively, where $K_z^d = ik_z^d$ and $K_z^m = ik_z^m$. This defines the penetration depth of the surface plasmons (the depth at which the field amplitude falls to $1/e$) as $\delta_{zd} = \frac{1}{|K_z^d|}$ and $\delta_{zm} = \frac{1}{|K_z^m|}$ for dielectric and metal respectively.

The surface plasmon wave vector in the x direction, k_x, is defined as

$$k_x = k_x^r + ik_x^i = \frac{\omega}{c}(\frac{\varepsilon_d \varepsilon_m}{\varepsilon_d + \varepsilon_m})^{1/2}, \tag{1.5}$$

see ref. (Raether, 1988). The imaginary part of the k_x, k_x^i, is responsible for the propagation loss of the surface plasmon waves, while, the real part of the wave vector, k_x^r, defines the dispersion relation of the surface plasmons. The value of k_x^r, as long as $|\varepsilon_m^r| > \varepsilon_m^i$, can be estimated as:

$$k_x^r = \frac{\omega}{c}(\frac{\varepsilon_d \varepsilon_m^r}{\varepsilon_d + \varepsilon_m^r})^{1/2}. \tag{1.6}$$

Fig. 1.2 shows the dispersion relation of a plasmon resonance wave and the light line of air. As the operating frequency increases towards $\omega = \omega_{sp} = \frac{\omega_p}{\sqrt{1+\varepsilon_d}}$, the dielectric constant of the metal, estimated using the free electron gas approximation $\varepsilon_m(\omega) = 1 - \frac{\omega_p^2}{\omega^2}$, becomes less negative and reaches $\varepsilon_m^r = -\varepsilon_d$. Therefore, the value of k_x^r tends to infinity.

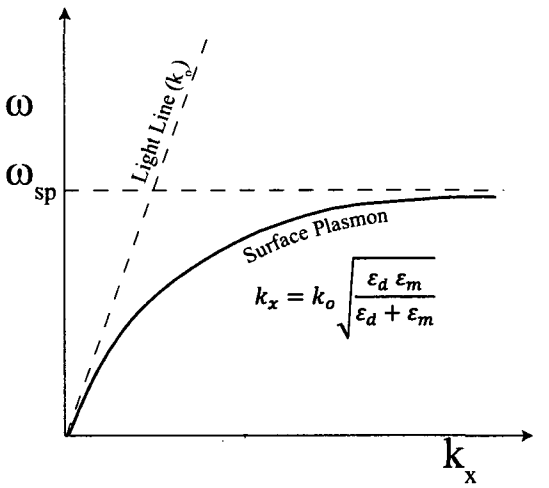

FIG. 1.2 – *Schematic of surface plasmon resonance waves dispersion relation and the air line.*

1.3 Excitation of Surface Plasmons

To excite the surface plasmon by light, the light wave vector parallel to the metal/dielectric interface should be matched with that of the surface plasmon, i.e.

$$k_x^{light} = k_x^r = \frac{\omega}{c}(\frac{\varepsilon_d \varepsilon_m^r}{\varepsilon_d + \varepsilon_m^r})(1/2). \tag{1.7}$$

Since the wave vector of the surface plasmon propagating along a metal/dielectric interface is always larger than that of the light propagating in the adjacent dielectric , a coupler such as a prism or waveguide should be used to match the two wave vectors to achieve phase matching between the wave vector of light and surface plasmon.

Kretschmann configuration, shown in Fig. 1.3(a), is one of the example of the use of prism as a coupler. In the Kretschmann configuration, the p-polarized light beam directed into a glass prism reflects from a thin metallic layer at the prism facet. Thus, to excite the surface plasmon the value of the light wave vector component parallel to the metallic layer, $k_x^{light} = \frac{\omega}{c} n_{prism} \sin\theta$, can be adjusted by the proper choice of the angle of incidences(as long as the prism refractive index is larger than that of the dielectric material).

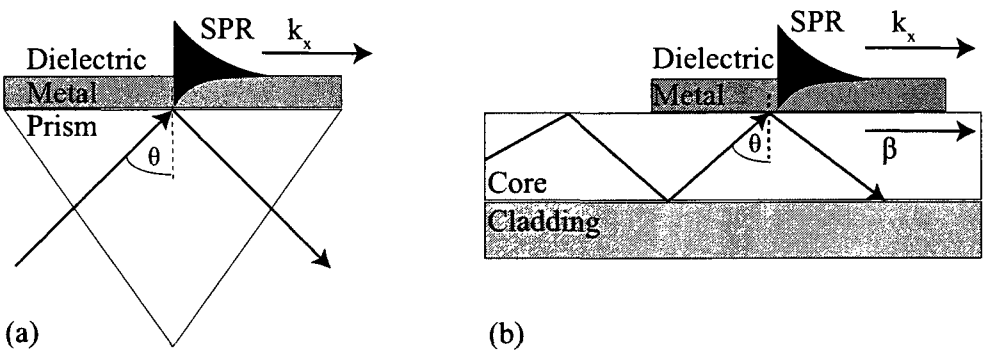

FIG. 1.3 – *Schematics of using a coupler for plasmonic excitation, a) the use of a prism in Kretschmann configuration, b) the use of a slab waveguide with a TM polarized.*

In another configuration, Fig. 1.3 (b) shows the schematic of a slab waveguide, guiding a TM mode, operating as a coupler to excite the plasmon waves on the thin metallic layer deposited on the top of the waveguide. In direct analogy to the prism couplers in Fig. 1.3(a), the angle of incident of light, is defined by the propagation constant of the guided mode. By adjusting the propagation constant of the guided mode one can adjust the incident angle of light to excite the plasmon wave, so that $\beta_{mode} = k_x^r$.

The conventional waveguide designs are limited by the limited range of the material refractive indexes available experimentally. As a result, the phase matching between plasmon and a core mode is typically challenging. To overcome a material imposed challenge will use the innovative waveguide geometries to manipulate the mode dispersion relations and to achieve phase matching between the plasmonic and guided modes. Consider for example, the use of a MOF for the plasmon-based sensor design. MOF complex geometry has enough structural (geometrical) parameters to tune the modal effective index of its guided modes by the choice of the position and the size of the air holes.

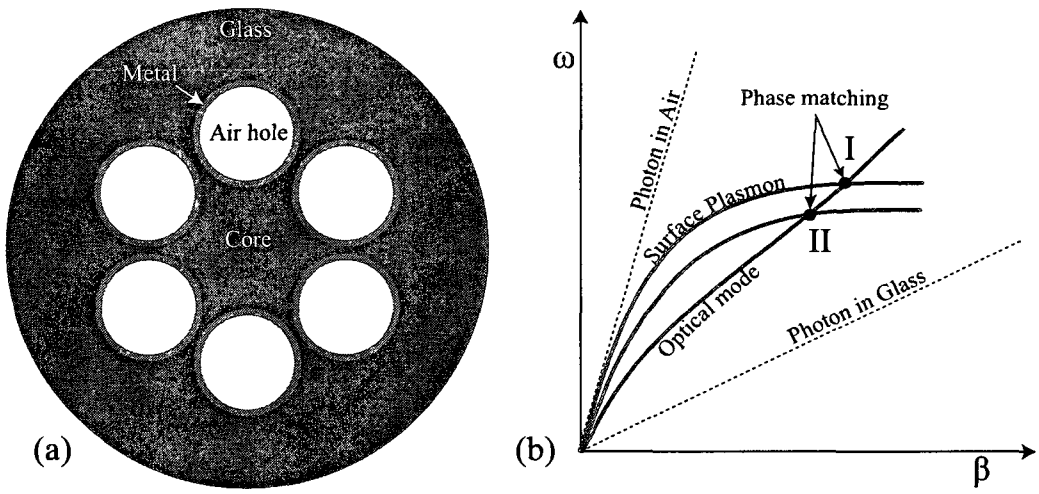

FIG. 1.4 – *a) Schematic of the cross section of a simple microstructured fiber with metallized holes, b) Schematic of the dispersion relation of the guided core mode and surface plasmons for two different value of analyte refractive index, Points I and II correspond to the the phase matching points between the plasmon and a core guided fiber mode.*

Fig. 1.4(a) shows the schematic of the cross section of a simple MOF made of a single material, glass or polymer. The six air holes surrounding the fiber core act as a lower refractive index cladding, confining the optical power in the higher refractive index core. The hole surfaces is further metallised to enable excitation of a surface plasmon. Furthermore, the choice of the position and size of the air holes allows tuning of the effective refractive index of the core mode guided along the fiber, thus enabling phase matching between the core mode and plasmon at a certain desirable wavelength.

Fig. 1.4 (b) is the schematic of the dispersion relations of the fundamental core guided mode and the surface plasmon waves. The figure also shows the light lines of air and glass. The intersection points I and II indicate the phase matching points between the core mode and the plasmon dispersion relations. At a phase matching point, a large part of the optical power in the fiber core mode is transferred to the lossy surface plasmon wave propagating at the metallic layer covering the air holes. This results in a significant decrease in the transmitted power in the vicinity of the wavelength of phase matching. Moreover, according to (1.6) the propagation constant of the surface plasmon k_x changes when changing the dielectric constant of a bordering analyte ($n = \sqrt{\varepsilon_d}$). Therefore a change in the analyte dielectric constant changes the position of the phase matching point, and therefore position of the dip in the transmission spectrum. For example, the position of the phase matching point shown in Fig. 1.4 (b) shifts from I to II; thus, resulting in a shift for the loss dip. Several sensing methodology based on the shift of sharp spectral features (loss dip, for example) can be used to enable sensing. We will explain several common sensing methodologies used in the next section.

1.4 Methodology

In this section we explain the methodology used for the design of the SPR sensors and sensing strategies. In the first part, methodologies for SPR design based on PBG and TIR

MOFS at the visible-IR and THz will be discussed. In the second part, the proposed methodologies for refractometry sensitivity and biolayer detection methods are described by mean of two intuitive examples.

1.4.1 SPR Sensor Design Methodologies

The methodology for MOF based SPR sensor designs is quite general and its particular implementation can be based on the type of waveguide, i.e. TIR or PBG MOFs. Usually, we start with a choice of an operational wavelength λ_c taking place at visible, IR or THz. Then, the surface plasmon effective refractive index $n_{eff}(\lambda_c)$ at λ_c is approximated by its value for the plasmon excitation on a planar metal-analyte interface. Afterwards, a TIR or PBG based waveguide should be used based on the desired operation wavelength of the SPR sensors. For example, for the visible range we prefer to use TIR MOF, as explained in chapter 2, because it is easy to design and even fabrication. For the IR range or double plasmonic peaks excitation, the proper choice is a PBG MOF giving more ability to tune the modal effective index. However, the design of a PBG MOF is more difficult than a TIR MOF. For THz range, the waveguide of choice is the subwavelength porous fiber guiding light by TIR mechanism, introduced in chapter 4.

Even thought design methodologies for each proposed SPR sensors are detailed in the next five articles (chapters), we will briefly discuss the design methodologies of these MOFs in the following. Pitch (Λ), the center to center distance of two holes, and the diameter of holes (d) are the two most important parameters to design a microstructured optical fiber. In a TIR MOF usually an array of hexagonal airholes constitutes a low index cladding surrounding the core of fiber. Also, the core of MOF can be contain of one or several small holes. In addition to the size of cladding airholes, the size of the small air holes in the core of fiber gives more freedom to tune the modal effective index of the core mode. Usually, the diameter of the core of TIR MOF, created by a missing hole in

the center of fiber, is 2Λ , which depends on the size of pitch. Therefore, by changing the size of core and cladding airholes and pitch, one can adjust the effective index of the core mode to be equal to that of surface plasmon at the desired wavelength λ_c. In the case of PBG MOFs, the photonic bandgap of the waveguide reflector at λ_c has to be designed to be centered in the vicinity of $n_{eff}(\lambda_c)$. By varying the core size of fiber (or considering a proper sized air hole inside the core), one can shift the dispersion relation of a core mode towards that of the plasmonic mode until phase matching occurs at λ_c. Also, the sensor length can be changed by varying the number of layers in a photonic crystal reflector, with more efficient reflectors resulting in the longer sensors. To design a subwavelength porous fiber at the THz, the most important parameter is to find the optimum size of airholes which maximize the power confinement inside them at λ_c, resulting the lowest possible modal effective index for the core mode of the fiber. As discovered in chapter 4, the optimum size of holes is around of $\sim 0.15-0.2\lambda_c$; by slightly changing the optimum size of airholes or number of airhole layers, one can increase the modal effective index of the core mode to match to that of surface plasmon at desired wavelength λ_c. In chapter 6, This type of fiber enables us to design a THz plasmonic-like sensor for gaseous analytes.

In all simulations, a finite-element method with perfectly matched layer boundaries and a four fold symmetry (Jin, 2002) is used in order to find the complex propagation constants of the core-guided and plasmonic modes by solving the vectorial Maxwell equations. In the particular case of Bragg fibers exhibiting circular symmetry, in chapter 3 and 5, the results produced by the finite element method is also confirmed by a transfer matrix method. In the case of PBG MOFs such as honeycomb photonic crystal fibers the bandgap characteristics are compared to the similar results presented in the related articles. Furthermore, in any simulation for any structure we first study the convergence and accuracy of our preformed simulations and obtained results. Finally we found that the error of our simulation varies from 5% to 15% depending on choosing the meshing size and fiber structure.

FIG. 1.5 – *Schematics of the two MOF-based SPR biosensors. Six air filled holes is used to confine light in the fiber core and to control the coupling strength between the core mode and a plasmon wave. A small air filled hole in the fiber core is used to lower the refractive index of a core guided mode to facilitate phase matching with a plasmon. Two large semi-circular metallized channels are integrated into the fiber structure to enable analyte flow and plasmon excitations.*

1.4.2 Surface Plasmon Sensing Methodologies

In this section we describe the surface plasmon sensing methodologies by means of two examples. In the first example the design criteria and sensing methodology for the TIR MOF-based surface plasmon sensor of a bio-layer thickness is described, while the second example presents the design of a Bandgap MOF-based surface plasmon sensor for the detection of changes in the analyte.

In the first example, we investigate sensitivity of the microstructured optical fiber-based sensors of a bio-layer thickness. The MOF fibers guide using an effective TIR mechanism. Fig. 1.5 shows the schematic of the hexagonal solid-core MOF-based SPR sensors. This design features two large semi-circular channels containing analyte. Thin gold films are deposited on one side of the channels closer to the fiber core.

To lower the refractive index of the core guided mode (to facilitate phase matching with a plasmon) we introduce a small hole of diameter d_c into the fiber core center. All the

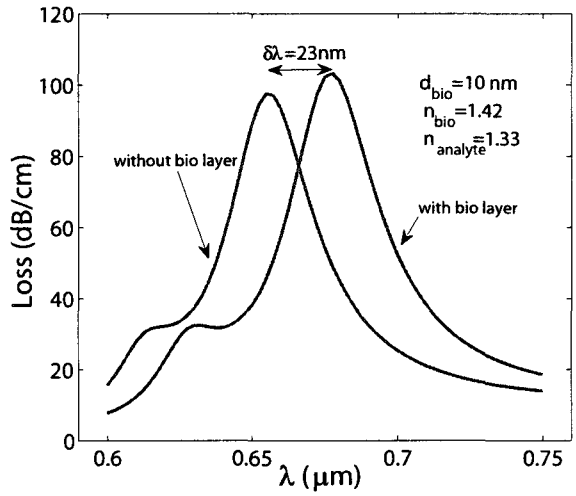

FIG. 1.6 – *Loss spectra of a fundamental core guided mode for the design shown in Fig. 1.5. Loss peaks correspond to the excitation of a plasmon mode on the surface of metallized channels filled with aqueous analyte* $n_a = 1.33$. *Modal losses are shown for the bio-layer thicknesses* $d_{bio} = 0$ *and* $d_{bio} = 10$, *assuming the bio-layer refractive index* $n_{bio} = 1.42$. *By changing the bio-layer thickness, attenuation peak corresponding to the point of phase matching between the core guided and plasmon modes shifts.*

holes in the fiber crossection are filled with air $n_{air} = 1.0$, while metal covered semi-circular channels are filled with analyte (aqueous solution) $n_a \simeq 1.33$. In the design we consider the diameters of the 6 holes surrounding the fiber core to be $d = 0.6\Lambda$, while the diameter of a central hole is taken to be $d_c = 0.45\Lambda$. Pitch of the underlying hexagonal lattice is $\Lambda = 2\ \mu$m. By changing the size of a central hole, one can tune the effective refractive index of the fundamental mode. The semi circular channels of the Fibers are metallized with a thin gold layer and feature large sizes to facilitate the flow of analyte. Channel size (difference in the inner and outer radii) is 1.5Λ, while thickness of the bridge connecting the fiber core and cladding regions is $d_c/4$. Finally, we assume that MOF is made of a silica glass with refractive index given by the Sellmeier equation, and gold layer thickness is defined as d_{gold} and in this work is in the range $40-65$ nm.

For the MOF-based sensor with $d_{gold} = 50$ nm, $d_{bio} = 0$ (Fig. 1.6) the phase matching

point is located at 660 nm where the difference between the real parts of the modal refractive indexes of the core and plasmon mode is the smallest. In the vicinity of a phase matching point the two modes become strongly mixed, with losses of a core guided mode increasing dramatically due to the energy transfer into the lossy plasmon mode (see Fig. 1.6). In bio-sensing applications, one defines sensitivity of an SPR sensor with respect to its ability to detect changes in the thickness d_{bio} of a thin bio-layer of index n_{bio} deposited on top of the metal film; n_{bio} is generally between 1.4 and 1.42 for most bio-molecules. Such a layer might, for example, consist of proteins bound to antibodies, which are intern, placed on a sensor surface to provide detection specificity. Core mode losses α [dB/cm] are presented in Fig. 1.6 for the two thicknesses of a bio-layer $d_{bio} = 0$ and $d_{bio} = 10$ nm. Thus, by changing the bio-layer thickness by only 10 nm the plasmon resonance peak shifts by $\sim$ 23 nm, which can be easily detected. Such a transduction mechanism can, thus, be used for the monitoring of formation of the nanometer-thin bio-layers on top of a metallized sensor surface.

We now discuss two main approaches to the detection of changes in the bio-layer thickness. The first method is known as a spectral-based method. Within this method, changes in the bio-layer thickness are detected by measuring displacement of a plasmonic peak in the absorption spectrum of a sensor. The sensitivity of the spectral method is defined as:

$$S_\lambda[nm \cdot nm^{-1}] = \lim_{d_{bio} \to 0} d\lambda_{peak}/d_{bio}, \tag{1.8}$$

where $d\lambda_{peak}$ is a shift in the wavelength of the absorption peak center measured before and after the bio-layer thickness is changed by d_{bio}. As an example, consider the sensor absorption spectra shown in Fig. 1.6, $d_{gold} = 50$ nm. Using definition (3.5), we find spectral sensitivity to be $2.3\ nm \cdot nm^{-1}$. It is typically a safe assumption that 0.1 nm change in the position of a resonance peak ($d\lambda_{peak}$) can be detected reliably, which leads to the sensor resolution of 0.044 nm in bio-layer thickness.

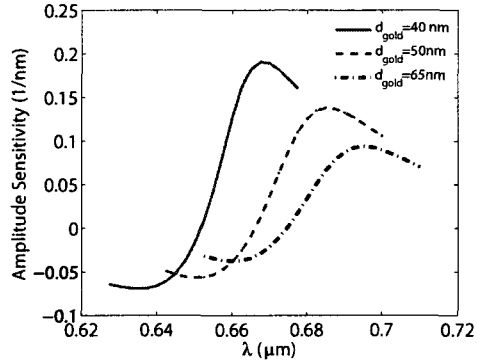

FIG. 1.7 – *Sensitivity of the MOF-based sensors to changes in the bio-layer thickness. Data is presented for sensors having three different values of the gold layer thicknesses* $d_{gold} = 40$ *nm,* 50 *nm,* 65 *nm.*

We now consider the second detection approach, which is known as amplitude-based detection method. In this method all the measurements are performed at a single wavelength. Advantage of this method is its simplicity and low cost compared to the spectral-based method, as no spectral acquisition is required. We now define sensitivity of the amplitude-based detection method. Let $\alpha(\lambda,d_{bio})$ to be transmission loss of the fundamental core mode as a function of the wavelength of operation and bio-layer thickness. Considering P_0 to be the power launched into the fiber core mode, the power detected at the end of a sensor of length L will then be $P(L,\lambda,d_{bio}) = P_0 exp(-\alpha(\lambda,d_{bio})L)$. At the operation wavelength λ, amplitude sensitivity to changes in the bio-layer thickness can then be defined as $S_A(\lambda)[nm^{-1}] = \lim_{d_{bio}\to 0} |P(L,\lambda,d_{bio}) - P(L,\lambda,0)|/P(L,\lambda,0)/d_{bio}$. Sensor length L is limited by the modal transmission loss. A reasonable choice of a sensor length is $L = 1/\alpha(\lambda,d_{bio})$. Corresponding sensor volume is then sub-nL. This choice of a sensor length results in a simple definition of sensitivity for small changes in the bio-layer thickness:

$$S_A(\lambda)[nm^{-1}] = -(\partial\alpha(\lambda,d_{bio})/\partial d_{bio})/\alpha(\lambda,d_{bio}). \tag{1.9}$$

In Fig. 1.7 we present amplitude sensitivities of the proposed MOF-SPR sensors for the three different values of the gold layer thickness $d_{gold} = 40$nm, 50nm, 65nm. We observe that for thicker gold films sensor sensitivity decreases. This is simple to understand by noting that when metallic layer thickness becomes larger than that of a metal skin depth (~20-30 nm) fiber core mode becomes effectively screened from a plasmon mode, thus resulting in a low coupling efficiency, and, as a consequence, in low sensitivity. As an example, consider the case of a 40 nm thick film for which maximum sensitivity to changes in the bio-layer thickness is equal to $\sim 0.2\ \text{nm}^{-1}$ and is achieved in the vicinity of 670 nm. By adding only 1nm thick bio-layer the transmitted intensity of a sensor would change by $\sim 20\%$, which can be easily detected. It is typically a safe assumption that 1% change in the transmitted intensity can be detected reliably, which leads to the sensor resolutions of 0.05 nm.

In the second example, we present design principles behind photonic bandgap fiber-based SPR sensors (Hassani et al., 2008f). Particulary we show that in photonic bandgap fiber-based SPR sensors, fundamental Gaussian-like leaky core mode can be phase matched with a plasmon at higher wavelength, thus enabling sensing even in near-IR. The effective refractive indices of the leaky core modes can be arbitrarily smaller than that of a waveguide core material, thus enabling phase matching with a plasmon at any desirably frequency. Using such a leaky mode for sensing can also give the additional advantage of an effectively single mode propagation regime. Our proposed design is a SPR sensor based on a honeycomb photonic crystal fiber operating at 1060 nm. We further demonstrate a novel sensing mechanism based on the detection of breaking of an degeneracy between the two plasmonic excitations, the plasmonic excitations on the analyte/metal and the glass/metal interfaces.

In Fig. 1.8(a) the schematic of a honeycomb photonic crystal fiber-based SPR sensor is presented. The design parameters are chosen as follows, the center to center distance between adjacent holes is $\Lambda = 0.77\ \mu$m, the cladding hole diameter is $d = 0.55\Lambda$, the

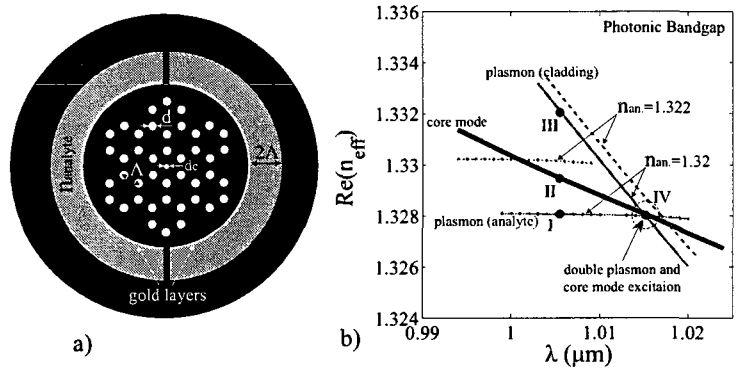

FIG. 1.8 – *Solid core honeycomb photonic crystal fiber-based SPR sensor. a) Schematic of the sensor. The solid core having a small central hole is surrounded with a honeycomb photonic crystal reflector. Two large channels are integrated to implement analyte access into the fiber reflector region. The channels are goldplated for plasmon excitation. The gold layer is bordered by the aqueous analyte. b) Band diagram of the sensor modes. Dispersion relation of the fundamental core mode (thick solid curve), analyte bound plasmonic mode (dashed curve with circles), and cladding bound plasmonic mode (dashed curve). The bandgap of an infinitely periodic reflector is shown as a clear region (Hassani et al., 2008f).*

diameter of the hole in the core center is $d_c = 0.35\Lambda$. The fiber is made of silica glass with a refractive index of $n_{glass} = 1.45$, the core and cladding holes are filled with air $n_{air} = 1$, while the large semi-circular channels are plated with a 40 nm thick layer of gold and filled with an aqueous analyte $n_a = 1.32$. The central hole in the fiber core lowers its effective refractive index compared to that of a silica cladding. Under certain conditions, such a core can support a mode confined by the bandgap of the honeycomb reflector. Guided by the bandgap of the fiber reflector, the effective refractive index of the core mode can be made much lower than that of the silica material. Moreover, radiation loss of a bandgap guided core mode can be reduced by adding more layers into the honeycomb reflector. The main reason why we chose a honeycomb structure of the fiber reflector is because it enables a very large photonic bandgap, thus simplifying considerably phase matching of the core guided and plasmonic modes. We design the fiber so that two plasmonic peaks are degenerate at $1009nm$ with $n_{analyte} = 1.32$. Fig. 1.8(b) shows

the dispersion relations of the Gaussian-like core mode (thick solid line), analyte bound plasmonic mode (thin solid line with circles) and cladding bound plasmonic mode (thick solid line).

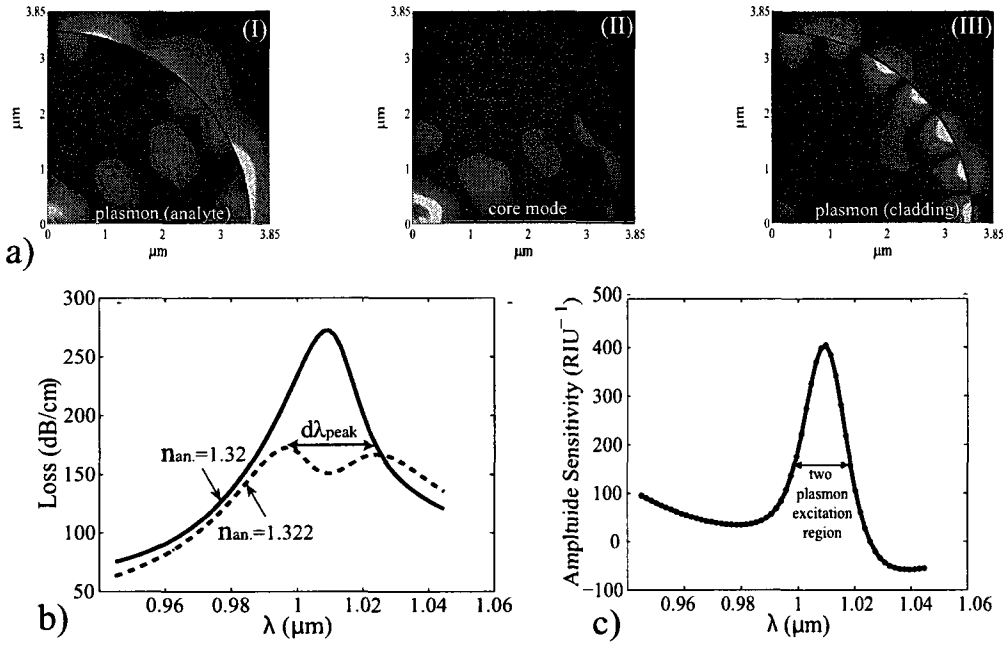

FIG. 1.9 – *Solid core honeycomb photonic crystal fiber-based SPR sensor. a) The energy flux distributions across the fiber cross-section are shown for the fundamental core mode (II) as well as the analyte and cladding bound plasmon modes (I,III) outside of the phase matching region. b) The solid curve shows loss of the fundamental core mode near the degenerate phase matching point with two plasmonic modes and* $n_{analyte} = 1.32$. *Due to degeneracy, only one peak is distinguishable in the loss curve. Dashed line shows splitting of the degeneracy in plasmonic modes when the analyte refractive index is changed to* $n_{analyte} = 1.322$. *c) Dependence of the sensor amplitude sensitivity on wavelength (Hassani et al., 2008f).*

Corresponding flux distributions of the core guided and plasmonic modes are presented in Fig. 1.9(a). The core mode loss shows a single plasmonic peak (solid curve in Fig. 1.9(b)). When the refractive index of the analyte is varied, this affects the two plasmonic dispersion relations differently. Particularly, the analyte bound plasmon mode is affected much more strongly by the changes in the analyte refractive index than the clad-

ding bound plasmonic mode. As a result, degeneracy is lifted, and two closely spaced plasmonic peaks appear in the core mode loss curve (dashed curve in Fig. 1.9(b)).

For example, a 0.002 change in the analyte refractive index splits a single plasmonic peak into two peaks separated by 27.5 nm. This permits a novel spectral detection technique, where relative peak separation can be used to characterize changes in the analyte refractive index. By defining spectral sensitivity as: $S_\lambda = |\lambda_{peak1} - \lambda_{peak2}|/dn_{analyte}$, we find spectral sensitivity of 13750 nm·RIU^{-1}. It is typically a safe assumption that a 0.1 nm change in the position of a resonance peak can be detected reliably, which results in a sensor resolution of $7.2 \cdot 10^{-6}$ RIU, which is, to our knowledge, the highest reported spectral sensitivity of an aqueous fiber-based SPR sensor. Finally, in Fig. 1.8(c), we present the amplitude sensitivity of the proposed honeycomb fiber-based sensor as defined by: $S_A(\lambda)[RIU^{-1}] = -\frac{1}{\alpha(\lambda,n_a)}\frac{\partial\alpha(\lambda,n_a)}{\partial n_a}$. Where $\alpha(\lambda,n_a)$ and n_a are the transmission loss of the core mode and the refractive index of the analyte, respectively . The maximal sensitivity 400 RIU^{-1} is achieved at 1009 nm. It is typically a safe assumption that a 1% change in the transmitted intensity can be detected reliably, which leads to a sensor resolution of $2.5 \cdot 10^{-5}$ RIU. Sensor length in this case is in $\sim$ 1 mm range.

In conclusion, the theory of surface plasmon waves and then the excitation of surface plasmons using light are discussed. Then, we have explained the surface plasmon sensor design and sensing methodologies. This part includes two examples which illustrate the design criteria for the TIR MOF based SPR sensor for biolayer thickness detection and the design of a PBG MOF based SPR sensor for refractometry sensing in an aqueous analyte.

CHAPITRE 2

ARTICLE 1: DESIGN CRITERIA FOR MICROSTRUCTURED-OPTICAL-FIBER-BASED SURFACE-PLASMON-RESONANCE SENSORS

Alireza Hassani, Maksim Skorobogatiy[1].

The emphasis of this article is on using TIR based MOFs instead of conventional fibers in the design of the SPR sensors. First we indicate the difficulties that conventional fiber based SPR sensors face, such as light-plasmon phase matching and polishing difficulties. Second, by presenting the design strategies for two MOF based SPR sensors designs, we theoretically demonstrate the ability of MOFs to over come the limitation that intrinsically exist at conventional fiber based SPR sensors. For example, this article shows that the modal effective index of light can be adjusted by geometry and size of holes in the MOFs, resulting in light-plasmon phase matching easiness. Furthermore, ability of making different shape of gold plated holes or channels in MOFs prevents side polishing the fiber and enables having different shape or size of microfluidic channels and metallic layers that is not possible in the conventional fiber based SPR sensors. The comparison between sensitivity of surface plasmon on metallic holes and semi-cylindrical channels in this article shows that the semi-cylindrical shape metallic layer present higher refractometry sensitivity. The maximum refractometry sensitivity at $0.65\ \mu$m is calculated to be $5 \cdot 10^{-5}$ RIU at the amplitude-based mode and $3 \cdot 10^{-5}$ RIU at the wavelength interrogation mode. Overall, this article is a starting point for the design of TIR MOF based SPR sensors and discuss the parameters that are important in design of these sensors. Moreover some new design parameters like the shape of metallic layers are introduced.

1. Department Engineeing Physics, École Polytechnique de Montréal, Montréal Canada

2.1 Abstract

Design strategies for the Microstructured Optical Fiber-based Surface Plasmon Resonance sensors are presented. In such a sensor plasmons on the inner surface of the large metallized channels containing analyte can be excited by a fundamental mode of a single mode microstructured fiber. Phase matching between plasmon and a core mode can be enforced by introducing air filled microstructure into the fiber core. Particularly, in its simplest implementation effective refractive index of a fundamental mode can be lowered to match that of a plasmon by introducing a small central hole into the fiber core. Resolution of the MOF-based sensors is demonstrated to be as low as $3 \cdot 10^{-5} \mathrm{RIU}^{-1}$. Ability to integrate large size microfluidic channels for efficient analyte flow together with a single mode waveguide of designable modal refractive index is attractive for the development of integrated highly sensitive MOF-SPR sensors operating at any designable wavelength.

2.2 Introduction

Propagating at the metal/dielectric interface, surface plasmons (Agranovich and Mills, 1982) are extremely sensitive to changes in the refractive index of the dielectric. This feature constitutes the core of many Surface Plasmon Resonance (SPR) sensors. Typically, these sensors are implemented in the Kretschmann-Raether prism geometry to direct p-polarized light through a glass prism and reflect it from a thin metal (Au, Ag) film deposited on the prism facet (Kretschmann and Raether, 1968). The presence of a prism allows resonant phase matching of an incident electromagnetic wave with a high-loss plasmonic wave at the metal/analyte interface at a specific combination of the angle of incidence and wavelength. By detecting changes in the amplitude or phase of the reflected light due to its coupling with a plasmon wave one can detect minute changes in the

refractive index of an analyte bordering the metal layer. Using optical fibers instead of a prism in plasmonic sensors offers miniaturization, high degree of integration and remote sensing capabilities. Over the past decade, driven by the need of miniaturization of SPR sensors, various compact configurations enabling coupling between optical waveguide modes and surface plasmonic waves have been investigated. Among others, metallized single-mode, polarization maintaining, and multi-mode waveguides, metallized tapered fibers, and metalized fiber Bragg gratings have been studied (Jorgenson and Yee, 1993; Vidal et al., 1993; Alonso et al., 1993; Alonso et al., 1994; Homola, 1995; Trouillet et al., 1996; Tubb et al., 1997; Homola et al., 1997b; Slavik et al., 1998; Diez et al., 2001; Piliarik et al., 2003; Monzón-Hernández et al., 2004; Monzon-Hernandez and Villatoro, 2006; Suzuki et al., 2006; Ctyroky et al., 1999a; Trouillet et al., 1996; Weisser et al., 1999; Gupta and Sharma, 2005). Two principal difficulties hindering development of the integrated waveguide-based sensors have been identified. First challenge is phase matching of a waveguide core mode and a plasmonic wave. Mathematically, phase matching constitutes equating the effective refractive indexes of the two modes at a given wavelength of operation. In the case of a single mode waveguide effective refractive index of its core mode is close to that of a core material. For most practical core materials such index is higher than 1.45. Effective refractive index of a plasmon is typically close to that of a bordering analyte, which in the case of air is ~ 1.0, while in the case of water is ~ 1.33. Only at higher frequencies (Homola, 1995; Homola et al., 1997b) ($\lambda < 700$ nm for a plasmon on a gold metal film, for example) plasmon refractive index becomes high enough as to match that of a waveguide core mode. From a sensor design point of view it is quite unsatisfactory to be limited by the values of the material refractive indices without the ability of compensating material limitations with a judicious choice of a sensor geometry. In principle, phase matching problem can be alleviated by coupling to a plasmon via the high order modes of a multimode waveguide (Ctyroky et al., 1999a; Trouillet et al., 1996; Weisser et al., 1999; Gupta and Sharma, 2005). Such modes can have significantly lower effective refractive indices than a waveguide core index. In such

a set-up light has to be launched into a waveguide as to excite high order modes some of which will be phase matched with a plasmon mode. As only a fraction of higher order modes are phase matched to a plasmon, then only a fraction of total launched power will be coupled to a plasmon, thus reducing sensor sensitivity. Moreover, as power distribution in high order modes is very sensitive to the launching conditions this adds additional noise due to variations in a coupling setup.

Second problem that limits development of the waveguide based sensors is that of packaging of the microfluidics setup, waveguide and metallic layers into a single sensor. For example, in traditional single mode fiber based sensors, to metallize fiber surface one has to first strip the fiber jacket and then polish fiber cladding almost to the core to enable evanescent coupling with a plasmon. This laborious procedure compromises fiber integrity making the resulting sensor prone to mechanical failures. Integration of a metallized fiber piece into a microfluidics setup presents yet another additional step in sensor fabrication, thus increasing the overall fabrication cost.

The goal of this paper is to build upon a great body of ideas developed by the waveguide-based SPR sensing community and to illustrate that the phase matching and packaging issues can be facilitated using Photonic Crystal Fibers (PCFs) or Microstructured Optical Fibers (MOFs) operating in the effectively single mode regime. Recently, we have demonstrated that effective refractive index of a Gaussian-like core mode propagating in the bang gap of a photonic crystal waveguide (Skorobogatiy and Kabashin, 2006a; Skorobogatiy and Kabashin, 2006b) can be designed to take any value from 0 to that of a refractive index of a core material. This enables phase matching and plasmon excitation by the waveguide core mode at any desirable wavelength. It was also recently demonstrated (Kuhlmey et al., 2006; Hassani and Skorobogatiy, 2006) that plasmon mode can be excited by the core guided mode of a single mode holey fiber featuring a single ring of metallized holes. Microfluidics in microstructured fibers is enabled by passing analyte though the fiber porous cladding, thus, partially solving the packaging problem. Deposi-

tion of metal layers inside of the MOFs can be performed ether with high pressure CVD technique (Sazio et al., 2006) or electro-less plating techniques used in fabrication of metallized hollow waveguides and microstructures (Harrington, 2000; Takeyasu et al., 2005).

2.3 Geometry of a MOF-based SPR sensor

In this paper we develop general principles of the MOF design for applications in plasmonic sensing, where the two key requirements are phase matching with a plasmon wave and optimized microfluidics. Figs. 2.1(a,b) show the two schematics of proposed hexagonal solid-core MOF-based SPR sensors. In the first MOF, fiber core is surrounded by the two layers of holes. Metallized holes in the second layer are considerably larger than these in the first layer, thus simplifying the flow of analyte through them. This fiber has been considered in details in (Hassani and Skorobogatiy, 2006). In the second MOF, two large semi circular channels covered with metal are used to further enhance microfluidic flow. Another reason for the introduction of the two structures is to study the effect of metallic surface geometry on the efficiency of plasmonic excitation.

To lower the refractive index of a core guided mode (to facilitate phase matching with a plasmon) we introduce a small hole of diameter d_c into the core center. In place of a single hole in the core, an array of smaller holes can be used similarly to Ref. (Cordeiro et al., 2006). Holes in the core and in the first layer are filled with air $n_{air} = 1.0$, while metal covered holes in the second layer are filled with analyte (aqueous solution) $n_a \simeq 1.33$. As a first example we will consider a MOF with the diameters of the core, first and second layer holes chosen as $d_c = 0.5\Lambda$, $d_1 = 0.6\Lambda$ and $d_2 = 0.8\Lambda$, respectively. Pitch of the underlying hexagonal lattice is $\Lambda = 2\ \mu$m. By changing the size of a central hole, one can tune the effective refractive index of the fundamental mode. First layer of holes works as a low refractive index cladding enabling mode guidance in the fiber

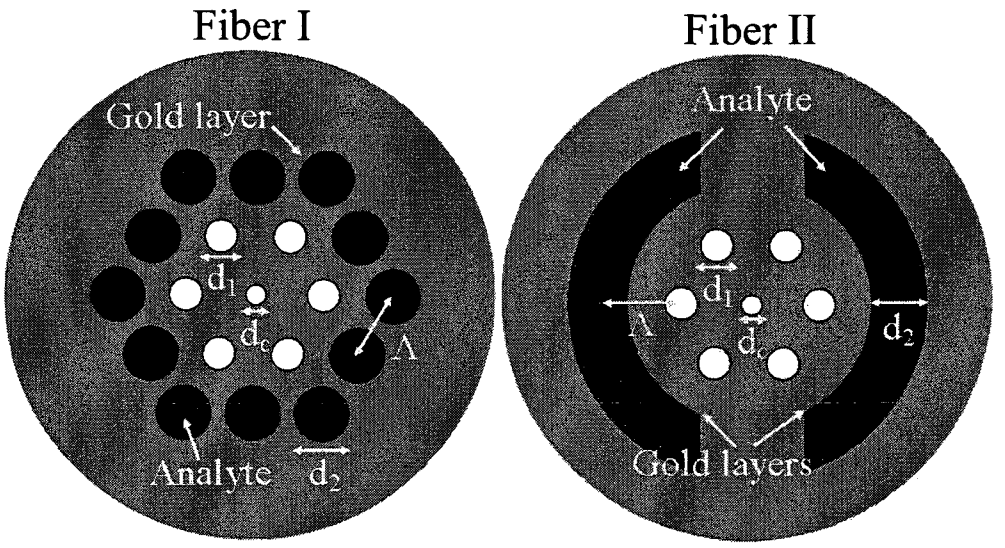

FIG. 2.1 – *Schematics of the two MOF-based SPR sensors. In the fiber I, large holes in the second layer are filled with analyte and metallized for plasmon excitation. Air filled holes in the first layer enable guiding in the higher refractive index fiber core, while at the same time, controlling coupling strength between the core mode and plasmon wave. Small air filled hole in the fiber core is used to lower the refractive index of a core guided mode to facilitate phase matching with a plasmon. In the fiber II, a large semi circular metallized channel is integrated into the fiber structure to enhance microfluidic flow.*

core. Coupling strength between the core mode and plasmon is strongly influenced by the size of the holes in the first layer, (larger hole sizes result in a weaker coupling). Holes in the second layer of Fiber I and semi circular channels of Fiber II are metallized with a $\sim$ 40 nm layer of gold and feature large sizes to facilitate the flow of analyte. Finally, we assume that MOF is made of a silica glass with refractive index given by the Sellmeier equation. Dielectric constant of gold ϵ_{Au} is approximated in the visible and near IR region by the Drude model (Kurihara K, 2002) $\epsilon_{Au}(\omega) = \epsilon^{\infty} - \omega_p^2/[\omega(\omega + i\omega_\tau)]$, where $\epsilon^{\infty} = 9.75$, $\omega_p = 1.36 \cdot 10^{16} rad/s$, and $\omega_\tau = 1.45 \cdot 10^{14} rad/s$.

2.4 Excitation of plasmonic waves by the core guided mode of a MOF

Finite element method with PML boundaries was used to find complex propagation constants of the core guided and plasmonic modes. A typical fiber-based plasmonic sensor operates in the vicinity of a phase matching point between the core guided mode and a plasmon wave localized at the metallized surface. As an example, in Fig. 2.2 for the fiber II we present dispersion relations of the core guided mode (solid line) and a plasmon wave (dashed line). Phase matching point is located at 640nm where the difference between the modal refractive indexes is the smallest. Energy flux distributions in the vicinity of a phase matching point (insets (a,b) in Fig. 2.2) allows clear differentiation of the nature of the two modes. In the vicinity of a phase matching point the two modes become strongly mixed (inset (c) in Fig. 2.2), with losses of a core guided mode increasing dramatically due to the energy transfer into the lossy plasmon mode. Core mode losses calculated as $Im(n_{eff})$ are presented in Fig. 2.2 in a thin solid line. For the reference, losses in [dB/m] are defined as $\alpha[dB/m] = 40\pi Im(n_{eff})/(ln(10)\lambda[m])$. Detection of increase in the loss of a core guided mode at the point of its phase matching with a plasmon constitutes the core of many sensor designs.

We now investigate plasmon wave transduction mechanism in greater details. In Fig. 2.3 we present losses of the core guided modes in the wavelength range of 0.5 μm-1.3 μm for the two MOF designs of Fig. 2.1. Thin solid line corresponds to fiber I, $n_a = 1.33$ and features three plasmonic excitation peaks located at 560 nm, 950 nm and 1290 nm defined by increase in the core mode propagation losses. Thick solid line corresponds to fiber II, $n_a = 1.33$ and features two plasmonic excitation peaks located at 640 nm and 1120 nm. To demonstrate potential of these fibers for sensing, we present in thin and thick dashed lines, losses of the core guided modes of the fibers I and II for the case when the analyte refractive index is slightly varied ($n_a = 1.34$ for the fiber I, and $n_a = 1.335$ for the fiber II). As a result, positions of the plasmonic resonances shift by

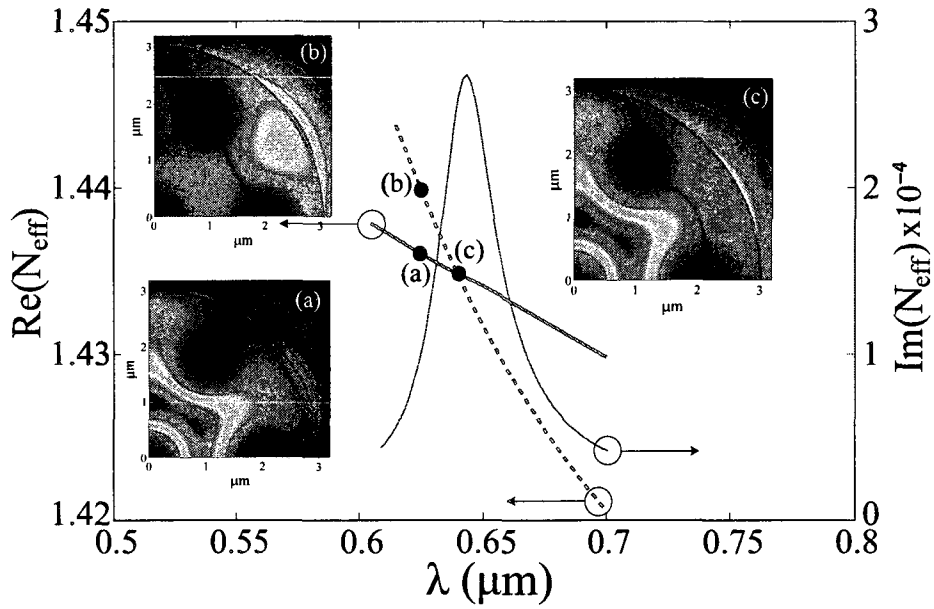

FIG. 2.2 – *Dispersion relations of a core guided mode (thick solid line) and a surface plasmon (thick dashed line) in the vicinity of the phase matching point. Insets (a), (b) show energy fluxes of the core guided and plasmon modes close to the phase matching point. Transmission loss of a core guided mode (thin solid line) exhibits strong increase at the phase matching point due to efficient mixing with a plasmon wave as confirmed by its energy flux distribution (inset (c)).*

$\sim$ 10 nm, with the first peak (at shorter wavelengths) being the most sensitive to the changes in the analyte refractive index. This transduction mechanism is commonly used for the detection of the analyte bulk refractive index changes, as well as monitoring of formation of the nanometer-thin bio-layers on top of a metallized sensor surface.

It is important to note that the shape of a metallized surface can have a significant effect on the plasmonic excitation spectrum. Thus, a planar metallized surface supports only one plasmonic peak, while a cylindrical metal layer can support several plasmonic peaks (Diez et al., 2001; Monzón-Hernández et al., 2004; Monzon-Hernandez and Villatoro, 2006; Al-Bader and Imtaar, 1993). In Fig. 2.3 we present energy flux distributions at the first and second plasmonic peaks of the two MOFs considered in this paper. From the

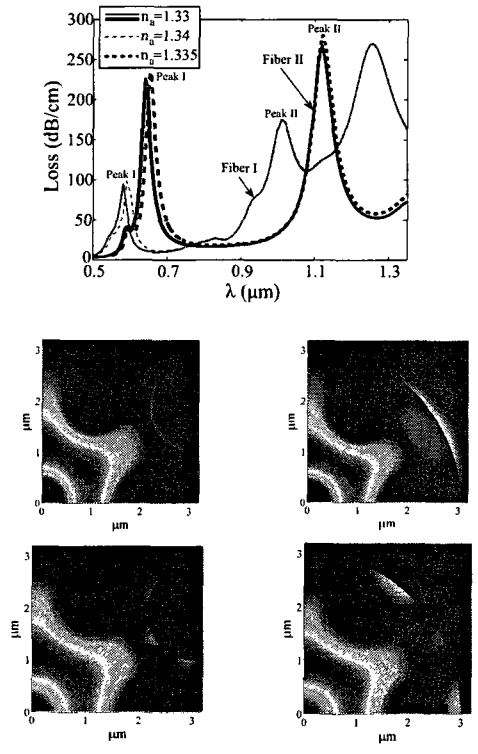

FIG. 2.3 – *Calculated loss spectra of the core guided modes for two fiber designs. Loss spectra (solid lines) feature several attenuation peaks corresponding to the excitation of plasmonic modes on the surface of metallized channels filled with aqueous analyte* $n_a = 1.33$. *By changing analyte refractive index (dotted lines) resonant attenuation peaks corresponding to the points of phase matching between the core guided and plasmon modes shift. In the insets, energy flux of a core guided mode is presented at various absorption peaks.*

pictures one can see that the shape of a metallizes surface does effect strongly the field distributions of plasmonic waves. Moreover, one can also notice that for the first plasmonic peaks there is considerably more field penetration into the analyte filled channels than in the case of the second plasmonic peaks. This explains why center wavelengths of the first peaks are considerably more sensitive than the center wavelengths of the second peaks to the changes in the analyte refractive index. In principle, by monitoring changes in the excitation of several plasmonic resonances, one can improve sensor sensitivity. With this method refractive-index resolution of $\sim 10^{-6}$ has been demonstrated in optical

fibers covered with circular metallic layers (Monzon-Hernandez and Villatoro, 2006).

Plasmon wave being a surface excitation is also very sensitive to the thickness of metallic layer. In Fig. 2.4 we show changes in the spectra of the first plasmonic peaks for fibers I and II when thickness of a gold layer on the inside of microfluidic channels is varied. Generally, modal propagation loss at resonance decreases when thickness of a gold layer increases, and simultaneously, center wavelengths of the peaks shift towards longer wavelengths. For a fiber II, for example, the position of a plasmonic peak shifts from 640 nm to 665 nm when the gold layer thickness increases from 40 nm to 65 nm. Given that the width of a peak at half maximum is $\sim$ 40 nm, changes in the peak position due to nanometer variations in the metal layer thickness can be easily detected. This transduction mechanism can be used to study metal nanoparticle binding events on the metallic surface of a sensor (Patskovsky et al., 2005). This mode of sensor operation can be of interest, for example, to the monitoring of concentration of metal nanoparticles attached to the photosensitive drugs in the photodynamic cancer therapy (Cinteza et al., 2006).

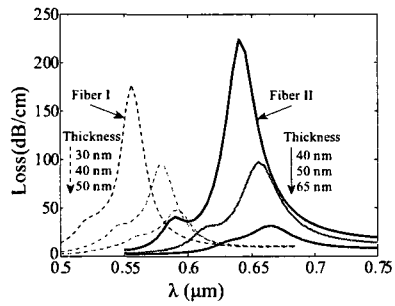

FIG. 2.4 – *Loss spectra in the vicinity of the first plasmonic peak for fibers with a gold layer of varying thickness. Dashed lines - fiber I, solid lines - fiber II.*

2.5 Tuning of plasmonic excitations

Plasmon wave excitation spectrum can be readily tuned by varying MOF structural parameters. In what follows we will study the effect of size variation of the central hole, as well as holes in the first layer, with a view of tuning and optimizing plasmon excitation by the core guided mode of a MOF.

In Figs. 2.5(a,b) we present losses and effective refractive indexes of a core guided mode of fiber II in the vicinity of a plasmonic peak I for various diameters of the central hole $d_c = 0.55\Lambda, 0.45\Lambda, 0.35\Lambda$. Diameter of the holes in the first layer is fixed and equal to $d_1 = 0.6\Lambda$. In Fig. 2.5(a) one can observe an overall increase in the modal losses of a core guided mode for the larger diameters of the central hole. This fact is easy to rationalize by noting that larger size of a central hole promotes expulsion of the modal field from the fiber core. This, in turn, leads to the greater modal presence near the metallic interface, hence higher propagation losses. Another consequence of the modal expansion from the fiber core and into the air filled microstructure is reduction of the modal refractive index, leading to the shift of a plasmonic peak towards longer wavelengths.

In Figs. 2.5(c) we present losses of a core guided mode of fiber II in the vicinity of a plasmonic peak I for various diameters of the holes in the first layer $d_1 = 0.6\Lambda, 0.7\Lambda$. Diameter of the central hole is fixed and equal to $d_c = 0.35\Lambda$. In Fig. 2.5(c) one can observe an overall decrease in the modal losses of a core guided mode for the larger size holes in the first layer. This is easy to understand by noting that larger size holes in the first layer lead to the lower refractive index of the microstructured cladding. This, in turn, increases core-cladding refractive index contrast, hence increasing modal confinement in the core region, and resulting in lower modal losses due to coupling to a metal surface in the second layer.

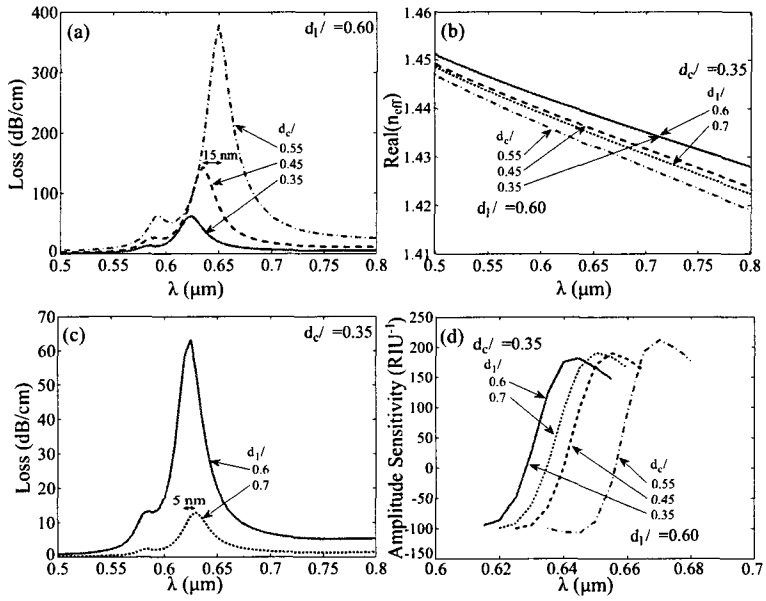

FIG. 2.5 – *Effect of the fiber structural parameters on the efficiency of plasmon excitation (case of fiber II, incorporating 40nm thick gold layer). (a) Loss of a core guided mode for various values of the fiber central hole diameter* $d_c = 0.55\Lambda, 0.45\Lambda, 0.35\Lambda$, *assuming a fixed diameter of the first layer holes* $d_1 = 0.6\Lambda$. *(b) Dispersion relation of a fiber core mode for various values of the structural parameters. (c) Loss of a core guided mode for two values of the first layer hole diameter* $d_1 = 0.6\Lambda, 0.7\Lambda$, *assuming a fixed central hole diameter* $d_c = 0.35\Lambda$. *(d) Sensitivity comparison between fibers of different structural parameters.*

2.6 Sensitivities of the MOF-based SPR sensors

The simplest mode of operation of a fiber-based SPR sensor is detection of changes in the bulk refractive index of an analyte. As real part of a plasmon refractive index depends strongly on the value of an analyte refractive index, then the wavelength of phase matching between the core guided and plasmon modes will also be sensitive to the changes in the analyte refractive index. There are two main approaches to detection. The first one is an amplitude based method, where all the measurements are done at a single wavelength. Advantage of this method is its simplicity and low cost as no spectral ma-

nipulation is required. Disadvantage is a smaller operational range and lower sensitivity when compared to the wavelength interrogation methods, in which transmission spectra are taken and compared before and after the change in the analyte has occurred.

We start by describing a single wavelength, amplitude based detection method. We define $\alpha(\lambda,n_a)$ to be the transmission loss of a core mode as a function of the wavelength and refractive index of an analyte. Considering P_0 to be the power launched into the fiber core mode, the power detected after propagation along the sensor of length L will be $P(L,\lambda,n_a) = P_0 exp(-\alpha(\lambda,n_a)L)$. For the operational wavelength λ, amplitude sensitivity to the dn_a change in the analyte refractive index can then be defined as $S_A(\lambda)[RIU^{-1}] = |P(L,\lambda,n_a + dn_a) - P(L,\lambda,n_a)|/P(L,\lambda,n_a)/dn_a$, which is frequently expressed in the units of $[dB \cdot RIU^{-1}]$ defined as $S_A(\lambda)[dB \cdot RIU^{-1}] = 10/ln(10)S_A(\lambda)[RIU^{-1}]$. Sensor length L is limited by the modal transmission loss. A reasonable choice of a sensor length is $L = 1/\alpha(\lambda,n_a)$, which falls into a sub-cm range for the MOFs described in this paper. Corresponding sensor volume is then sub-nL. This choice of a sensor length results in a simple definition of sensitivity for the small changes in the analyte refractive index

$$S_A(\lambda)[RIU^{-1}] = -(\partial\alpha(\lambda,n_a)/\partial n_a)/\alpha(\lambda,n_a).$$

In Fig. 2.6 we present amplitude sensitivities of the two proposed MOF-SPR sensors for the various values of the metal layer thickness 40 nm, 50 nm and 65 nm. Dashed lines correspond to the fiber I-based sensor, while solid lines correspond to the fiber II-based sensor. Maximum sensitivity of the fiber I-based sensor for detecting changes in the aqueous analyte in the vicinity of $0.6\ \mu$m is 520 dB·RIU^{-1}, while maximum sensitivity of a fiber II-based sensor in the vicinity of $0.65\ \mu$m is 820 dB·RIU^{-1}. It is typically a safe assumption that 1% change in the transmitted intensity can be detected reliably, which leads to the sensor resolutions of $8 \cdot 10^{-5}$ RIU and $5 \cdot 10^{-5}$ RIU for the fiber designs I

and II, respectively. For measuring changes in the aqueous analyte sensitivities of our fiber designs are comparable to the ones of the best existing fiber-sensors (Homola et al., 1999).

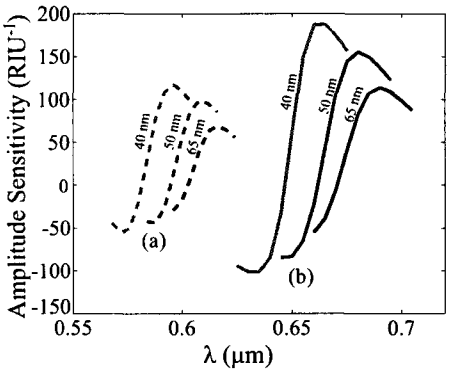

FIG. 2.6 – *Sensitivity of the two MOF-based sensors in the vicinity of the first plasmonic peak for various values of the gold layer thickness. Dashed lines - fiber I, solid lines - fiber II.*

Note from Fig. 2.6 that amplitude sensitivity depends strongly on the thickness of a gold layer. Overall, sensitivity reduces when metallic layer becomes thicker. This fact is simple to understand. When metallic layer thickness becomes significantly larger than that of a metal skin depth ($\sim$ 20-30 nm), fiber core mode becomes effectively screened from a plasmon, resulting in a low coupling efficiency, and, as a consequence, low sensitivity. Additionally, as fiber material refractive index is larger than that of an analyte, for thicker metal layers, plasmon refractive index decreases. In accordance with Fig. 2.5(b) this leads to the shift of the sensitivity peak (phase matching wavelength) towards longer wavelengths. Rather surprisingly, maximum value of sensitivity is only weakly dependent on the choice of the diameters of the central and first layer holes. In Fig. 2.5(c) we present amplitude sensitivity of the fiber II-based design for various choices of the d_c and d_1 parameters. While impacting strongly the wavelength of peak sensitivity and the value of the modal loss, various choices of hole diameters have a weak effect on the maximum value of sensitivity. As sensor length is inversely proportional to the modal

loss, tuning of the fiber structural parameters allows design of fiber-sensors of widely different lengths (from [mm] to [m]), while having comparable sensitivities. This might be important for the practical considerations of integrating such a fiber sensing element into a complete sensor system.

In the wavelength interrogation mode, changes in the analyte refractive index are detected by measuring displacement of a plasmonic peak. In this case sensitivity is defined as $S_\lambda[nm \cdot RIU^{-1}] = d\lambda_{peak}/dn_a$. For the two MOF-based designs with 40 nm gold layer, we find that their corresponding sensitivities are 800 nm·RIU^{-1} and 3000 nm·RIU^{-1}, respectively. It is typically a safe assumption that 0.1 nm change in the position of a resonance peak can be detected reliably, which leads to the sensor resolutions of $1.2 \cdot 10^{-4}$RIU and $3 \cdot 10^{-5}$ RIU for the fiber designs I and II, respectively. Again, as in the case of amplitude based sensors, we find that for measuring changes in the aqueous analyte using wavelength interrogation mode, sensitivities of our sensors are comparable to the ones of the best existing waveguide-sensors (Homola et al., 1999).

2.7 Conclusion

We have introduced a concept of Microstructured Optical Fiber-based Surface Plasmon Resonance sensor. Two main sensor design challenges were identified, which are the phase matching of the core guided and plasmonic modes, and microfluidics optimization to enable efficient analyte flow. Phase matching was facilitated by introduction of the hollow microstructure into the fiber core. Improved microfluidics was addressed by the integration of large analyte filled channels adjacent to the fiber core. Sensitivity of the amplitude-based sensor for measuring changes in the aqueous analyte at $0.65\,\mu$m was found to be $5 \cdot 10^{-5}$ RIU, assuming 1% amplitude change detection limit. Detection limit of the same sensor in the wavelength interrogation mode was found to be $3 \cdot 10^{-5}$ RIU, assuming 0.1 nm detection limit in the shift of a plasmonic peak. Thus found sensitivi-

ties are comparable to the ones of the best existing fiber and waveguide-based sensors optimized for aqueous analytes. Additionally, MOFs offer sensor design at almost any desirable wavelength in the visible and near IR because of their ability to support core guided modes of small effective refractive indices. By adjusting many of the MOF geometrical parameters is it considerably simpler to enforce phase matching with a plasmon compared to the standard TIR waveguides and fibers. Moreover, integration of the microfluidic channels during MOF drawing increases sensor reliability as laborious extra step of microfluidics packaging is avoided.

CHAPITRE 3

ARTICLE 2: PHOTONIC CRYSTAL FIBER AND WAVEGUIDE-BASED SURFACE PLASMON RESONANCE SENSORS FOR APPLICATION IN THE VISIBLE AND NEAR-IR

Alireza Hassani,Bertrand Gauvreau, Majid Fassi Fehri, Andrei Kabashin, Maksim Skorobogatiy [1].

The main focus of this paper is the design of PBG MOF based SPR sensors capable of operating at higher or multi-wavelengths. Therefore, we present the design criteria for SPR sensors based on solid and hollow core Bragg fibers, as well as PBG microstructured fibers. The advantage of using the PBG MOFs, which its modal effective index can be much smaller than its core index, instead of conventional fiber in the body of SPR sensors is the efficient phase matching with a surface plasmon at any wavelength of choice from the visible to IR. To our knowledge, this is not achievable by any other waveguide based SPR sensor designs. Also another advantage from point of view of biolayer thickness detection is that the SPR sensors operating at longer wavelength, i.e. the near-IR, have a larger probe depth with respect to the ones operating at shorter wavelength, i.e. visible, resulting in detecting biolayer consisting of bigger sized bioparticles. On the other hand, unlike the TIR PBG based SPR sensors presented at the previous chapter a wide variety of material combinations can be used to design PBG MOF based SPR sensors because their modal effective index is not limited by the value of the core index. Using PBG MOFs in the body of SPR sensors, plasmon excitation at $\sim 0.68\ \mu$m, $\sim 0.84\ \mu$m and $\sim 1.3\ \mu$m theoretically demonstrated that illustrate more freedom at operation wavelength for the SPR sensors. Moreover, we present a design of PBG MOFs based SPR sensors for double plasmonic peaks excitation, one peak at $\sim 0.65\ \mu$m and

another one at ~ 0.85 μm, which open new horizon for these type SPR sensor operating at visible and IR simultaneously. The maximum refractometry sensitivity is calculated to be $1.38 \cdot 10^{-5}$ RIU at the amplitude-based mode and $8.3 \cdot 10^{-6}$ RIU at the wavelength interrogation mode. Sensor lengths in our examples varied from sub-mm to $\sim$ 10 cm. Finally this article discussing the design criteria of PBG MOF based SPR sensors is a complementary part for the previous chapter presenting the design criteria of TIR MOF based SPR sensors.

1. Engineeing Physics Department, École Polytechnique de Montréal, Montréal Canada

3.1 Abstract

In the proposed photonic crystal waveguide-based surface plasmon resonance sensor, a plasmon wave on the surface of a thin metal film is excited by a Gaussian-like leaky mode of an effectively single mode photonic crystal waveguide. By judicious design of a photonic crystal waveguide, the effective refractive index of a core mode can be made considerably smaller than that of the core material, thus enabling efficient phase matching with a plasmon, high sensitivity, and high coupling efficiency from an external Gaussian source, at any wavelength of choice from the visible to near-IR, which is, to our knowledge, not achievable by any other design. Moreover, unlike the case of total internal reflection waveguide-based sensors, a wide variety of material combinations can be used to design photonic crystal waveguide-based sensors as there is no limitation on the value of the waveguide core refractive index. This sensor design concept was implemented using planar multilayer photonic crystal waveguides, solid and hollow core Bragg fibers, as well as microstructured photonic crystal fibers. Amplitude and spectral based methodologies for the detection of changes in the analyte refractive index were devised. Sensor resolution as low as $8.3 \cdot 10^{-6}$ RIU was found for aqueous analyte.

Key words: surface wave, surface plasmon resonance, fiber optic sensors, photonic crystal fiber

3.2 Introduction

Propagating at the metal/dielectric interface, surface plasmons (Agranovich and Mills, 1982) are extremely sensitive to changes in the refractive index of the dielectric. This feature constitutes the core of many Surface Plasmon Resonance (SPR) sensors. Typi-

cally, these sensors are implemented in the Kretschmann-Raether prism geometry where p-polarized light is launched through a glass prism and reflected from a thin metal (Au, Ag) film deposited on the prism facet (Kretschmann and Raether, 1968). The presence of a prism allows phase matching of an incident electromagnetic wave with a plasmonic wave at the metal/ambient dielectric interface at a specific combination of incidence angle and wavelength. Mathematically, the phase matching condition is expressed as an equality between the plasmon wavevector and a projection of the wavevector of an incident wave along the interface. Since the plasmon excitation condition depends resonantly on the value of the refractive index of an ambient medium within $100 - 300$ nm from the interface, the method enables detection of biological binding events on the metal surface with unprecedented sensitivity (Kretschmann and Raether, 1968). The course of a biological reaction can then be followed by monitoring angular (Liedberg et al., ; Melendez et al., 1996), spectral (Zhang and Uttamchandani, 1988) or phase (Kabashin and Nikitin, 1998; Grigorenko et al., 1999) characteristics of the reflected light. However, the high cost and large size of commercially available systems makes them useful only in a laboratory, while many important field and other applications remain out of the reach of this method.

Using optical waveguides and fibers instead of a bulk prism configuration in plasmonic sensors offers: miniaturization, high degree of integration and remote sensing capabilities. In fiber and waveguide-based sensors, one launches the light into a waveguide core and then uses coupling of a guided mode with a plasmonic mode to probe for the changes in the ambient environment. To excite efficiently a surface plasmon, the phase matching condition between a plasmon and a waveguide mode has to be satisfied, which mathematically amounts to the equality between their modal propagation constants (effective refractive indices). Over the past decade, driven by the need for miniaturization of SPR sensors, various compact configurations enabling coupling between optical waveguide modes and surface plasmonic waves have been investigated. Among others, metallized

single mode, multimode and polarization maintaining waveguides and fibers, metallized tapered fibers, metallized fiber Bragg gratings (Vidal et al., 1993; Alonso et al., 1994; Homola, 1995; Tubb et al., 1997; Homola et al., 1997b; Diez et al., 2001; Piliarik et al., 2003; Monzón-Hernández et al., 2004; Monzon-Hernandez and Villatoro, 2006; Suzuki et al., 2006; Ctyroky et al., 1999a; Al-Bader and Imtaar, 1993; Jorgenson and Yee, 1993; Trouillet et al., 1996; Ctyroky et al., 1999b; Weisser et al., 1999; Gupta and Sharma, 2005), and, recently, solid core microstructured fibers (Kuhlmey et al., 2006; Hassani and Skorobogatiy, 2006; Hassani et al., 2008a), as well as planar photonic crystal waveguides (Skorobogatiy and Kabashin, 2006a) have been studied. In the majority of fiber implementations (with an exception of microstructured fibers), one typically strips the fiber polymer jacket and polishes off the fiber cladding until fiber core is exposed; then, a metal layer is coated directly onto the fiber core. Thus the functionalized surface of a fiber core is then exposed to an analyte.

Ideally, one would use a single mode fiber or waveguide with all the power travelling in a single Gaussian-like core mode operating near the point of resonant excitation of a plasmon (Lavers and Wilkinson, 1994; Harris and Wilkinson, 1995; Weiss et al., 1996; Homola et al., 1997b; Dostalek et al., 2001; Sheridan et al., 2004). A Gaussian shape for core mode is important as it is best suited for excitation by standard Gaussian laser sources. Near the point of phase matching, most of the energy launched into a waveguide core mode could be efficiently transferred into a plasmon mode. However, in the Total Internal Refraction (TIR) single mode waveguides with low refractive index-contrast, coupling with a plasmon is realized at essentially grazing angles of modal incidence on a metal layer. As follows from the basic SPR theory, coupling at such grazing incidence angles leads to an inevitable decrease of sensitivity of a SPR method. In principle, high index-contrast single mode waveguides (see Fig. 3.1(a)) could be employed to increase the angle of modal incidence on the interface. However, phase matching between plasmon and fundamental waveguide mode is typically hard to realize. This is related to the

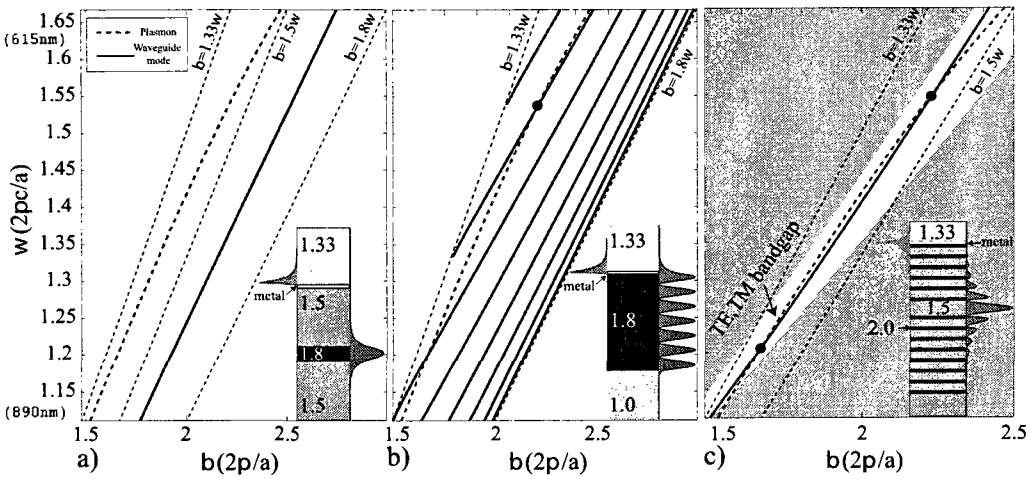

FIG. 3.1 – *Band diagrams and schematics of various sensor implementations. a) Single mode waveguide-based sensor. Dispersion relations of a core guided mode (solid) and a plasmon (thick dashed). Inset - coupler schematic;* $|H_{||}|^2$ *of a plasmon (left) and a core mode (right). b) Multimode waveguide-based sensor. Dispersion relations of the core modes (solid) and a plasmon (thick dashed). Inset - coupler schematic;* $|H_{||}|^2$ *of a plasmon (left) and a high order mode (right) at the phase matching point (black circle). c) Planar photonic crystal waveguide-based sensor. Dispersion relation of a fundamental Gaussian-like leaky core mode (solid) and a plasmon (thick dashed). Inset - coupler schematic;* $|H_{||}|$ *of a plasmon (left) and a core mode (right).*

fact that the effective refractive index of a core guided mode is close to the refractive index of the core material, which is typically larger than 1.45 due to practical material limitations. The effective refractive index of a plasmon is close to the refractive index of the ambient medium which is typically $n_a = 1$ for air or $n_a = 1.3$ for water. Thus, large discrepancy in the effective indices (as seen from Fig. 3.1(a)) makes phase matching between the two modes hard to achieve, except at higher frequencies ($\lambda < 650$ nm), where the plasmon dispersion relation deviates towards higher refractive indices. Thus, due to practical limitation on the lowest value of the waveguide core and cladding refractive indices, single mode TIR waveguide-based sensors were demonstrated mostly in the visible where the phase matching condition is easier to enforce.

Problems with phase matching and loss of sensitivity due to shallow angles of inci-

dence could be, in principle, alleviated by using multimode waveguides (Jorgenson and Yee, 1993; Trouillet et al., 1996; Ctyroky et al., 1999b; Weisser et al., 1999; Gupta and Sharma, 2005) (see Fig. 3.1(b)). If launched properly, modal effective propagation angles in such waveguides can be much steeper, resulting in smaller effective refractive indices. However, in multimode waveguides only a certain number of higher order modes will be phase matched with a plasmon. Thus, sensitivity and stability of such sensors depend crucially on launch conditions. Moreover, as spatial field distribution in a Gaussian-like laser source is typically not well matched with the field distribution of higher order mode of a multimode waveguide, only a small fraction of energy can be launched into such a mode, resulting, again, in decreased sensitivity.

In this paper, we present design principles of a novel photonic crystal fiber and waveguide-based SPR sensors, and show that they integrate advantages of both the single mode and multimode waveguide-based SPR sensors. Moreover, in photonic crystal fiber and waveguide-based SPR sensors, fundamental Gaussian-like leaky core modes (see Fig. 3.1(c)) can be phase matched with a plasmon at any desired wavelength of operation, thus enabling sensing anywhere from the visible to mid-IR. The term "leaky mode" generally refers to the guidance mechanism where the effective refractive index of a propagating mode is smaller than that of the waveguide cladding. Such unusual modes are called leaky modes as, outside of a waveguide core, they do not exhibit a traditional evanescent decay into the cladding, but rather they radiate slowly (leak) into the cladding. Unlike in the case of common TIR waveguides, leaky modes in photonic crystal waveguides are confined by the bandgap of a photonic crystal reflector. As a consequence, the effective refractive index of the fundamental (lowest loss) leaky core mode can be designed to be arbitrarily smaller than that of a waveguide core material, thus enabling phase matching with a plasmon at any desired frequency. Moreover, the lowest loss leaky core mode typically exhibits a Gaussian-like intensity distribution in the waveguide core region, thus enabling convenient excitation by a Gaussian beam of an external light source. Using the

fundamental (lowest loss) leaky mode for sensing gives the additional advantage of an effectively single mode propagation regime. In particular, when a set of modes is excited at a sensor input, higher order leaky modes radiate out faster than a fundamental mode. Consequently, after a certain propagation distance, only the fundamental mode is left in the waveguide core. Finally, the effective angle of modal incidence onto a metal film, and hence sensitivity, can be varied at will by a proper selection of the waveguide core and reflector materials.

The paper is organized as follows. In the first part, we introduce planar photonic crystal waveguide-based SPR sensors and highlight the key ideas for their design. In the second part of the paper, we demonstrate the design of SPR sensors using solid core and analyte filled hollow core Bragg fibers operating at 685 nm, 850 nm and 1300 nm. We argue that for plasmon excitation in the near-IR, the analyte filled hollow core Bragg fibers present a potent solution for plasmon excitation. In the third part of the paper we present an SPR sensor using honeycomb microstructured photonic crystal fiber operating at 1000 nm. We conclude by summarizing major findings of this paper.

Finally, throughout the paper, to find the modes of planar waveguides and circular symmetric Bragg fibers we have used a standard transfer matrix approach, while for the calculation of modes of microstructured fibers we have used commercial finite element code by Rsoft.

3.3 SPR sensors using planar photonic crystal waveguides

We start by considering plasmon excitation by a Gaussian-like TM polarized mode of a planar photonic crystal waveguide (see Fig. 3.2(a)), in which light confinement in a lower refractive index core is achieved by a surrounding multilayer reflector. TM polarization of the electromagnetic field in a planar multilayer assumes a single magnetic

field component $H_{||}$ directed parallel to the plane of a multilayer, while the electric field component is confined to a plane perpendicular to the multilayer.

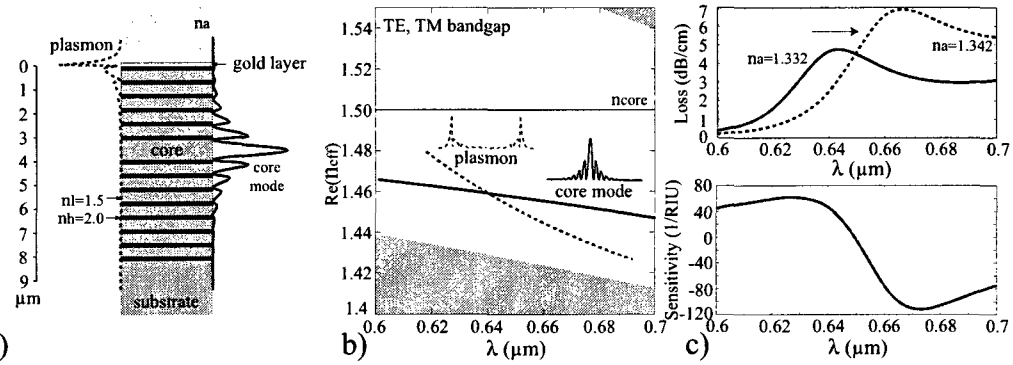

FIG. 3.2 – *Planar photonic crystal waveguide-based SPR sensor. a) Schematic of a sensor. Low refractive index core is surrounded by the periodic photonic crystal reflector. One side of the reflector is goldplated for plasmon excitation. Gold layer is bordered by aqueous analyte. $|H_{||}|$ field distribution in the fundamental core mode is shown on the right, while field distribution in a plasmonic mode is show on the left of the sensor schematic. b) Band diagram of sensor modes. Dispersion relation and field distribution of the fundamental core mode (thick solid curve), and plasmonic mode (dashed curve). Common part of the TE, TM bandgaps of a periodic reflector is shown as a clear region, while gray regions correspond to the continuum of the bulk reflector states. By design, the effective refractive index of a core guided mode can be made significantly smaller than that of the waveguide core material. c) Upper part: solid curve shows loss of a waveguide core mode near the phase matching point with a plasmon at which modal loss peaks. Dashed line shows shift of the modal loss curve when refractive index of the analyte is varied. Lower part: dependence of the sensor amplitude sensitivity on wavelength.*

The photonic crystal waveguide under consideration consists of 27 alternating layers having refractive indices $n_h = 2.0$, and $n_l = 1.5$. The core layer is layer number 12; having refractive index $n_c = n_l$. Analyte (first cladding) is water $n_a = 1.332$ bordering a 50 nm layer of gold. The substrate refractive index is 1.5. Theory of planar photonic crystal waveguides with infinite reflectors where $n_c = n_l$ (Skorobogatiy, 2005), predicts that, for a design wavelength λ_c, the effective refractive index $n_{eff}(\lambda_c)$ of the fundamental TE and TM core guided modes can be designed at will, as long as $0 \leq n_{eff} < n_l$, by

choosing the reflector layer thicknesses as

$$d_{l,h} = \frac{\lambda_c}{4\sqrt{n_{l,h}^2 - n_{eff}^2(\lambda_c)}}, \tag{3.1}$$

and by choosing the core layer thickness as $d_c = 2d_l$. Moreover, for this choice of n_c, the field distribution in the core is always Gaussian-like for TE polarized modes, while for TM polarized modes it is Gaussian-like as long as $n_{eff}^2 > \epsilon_l\epsilon_h/(\epsilon_l + \epsilon_h)$ (Skorobogatiy, 2005). By choosing the effective refractive index of a core mode to be that of a plasmon, a desired phase matching condition is achieved. For a waveguide with a finite reflector, the same design principle holds approximately. Thus, for an operating wavelength of $\lambda =$ 640nm considered in this example, phase matching is achieved when the photonic crystal waveguide above is designed using $\lambda_c = 635$ nm and $n_{eff}(\lambda_c) = 1.46$. A reasonable approximation to the $n_{eff}(\lambda_c)$ is a value of the effective refractive index of a plasmonic wave propagating at a planar gold-analyte interface:

$$n_{eff}^2(\lambda_c) = \frac{\epsilon_{gold}(\lambda_c)\epsilon_a(\lambda_c)}{\epsilon_{gold}(\lambda_c) + \epsilon_a(\lambda_c)}, \tag{3.2}$$

where ϵ_a is the dielectric constant of an analyte and ϵ_{gold} is the dielectric constant of the gold layer approximated by the Drude model:

$$\epsilon_{gold} = \epsilon_\infty - \frac{(\lambda/\lambda_p)^2}{1 + i(\lambda/\lambda_t)}, \tag{3.3}$$

where the choice $\epsilon_\infty = 9.75$, $\lambda_t = 13.0$ μm, $\lambda_p = 0.138$ μm presents one of the many possible fits of the experimental data.

In Fig. 3.2(b) we present band diagram of a planar photonic crystal waveguide-based SPR sensor. All the simulations are performed using standard transfer matrix theory on a complete system that includes both the waveguide and metal layer. Gray regions signify bulk states of a periodic reflector. The clear region is a common part of the reflector TE

and TM bandgaps. The thick solid line, which is almost parallel to the band gap edges, marked as "core mode" is a dispersion relation of a Gaussian-like leaky core mode with most of its modal energy concentrated in the low refractive index core. The dashed line marked as "plasmon" represents the dispersion relation of a plasmonic mode. Most of the plasmon energy is concentrated at the metal/analyte interface.

Near the phase matching point, fields of a core guided mode contain strong plasmonic contribution. As the plasmon exhibits very high propagation loss, the loss of a core mode (upper plot in Fig. 3.2(c)) will also exhibit a sharp increase near the phase matching point. An important aspect of the proposed setup is the freedom of adjusting loss of the core mode. As a leaky mode decays exponentially with respect to distance into the multilayer reflector, coupling strength between the plasmon and core modes can be controlled by changing the number of reflector layers situated between the waveguide core and a metal film. Ultimately, higher coupling strength leads to higher modal losses, hence, shorter sensor length. When the real part of the analyte refractive index is varied, the plasmon dispersion relation displaces accordingly, thus leading to a shift in the position of the phase matching point with a core guided mode. Consequently, in the vicinity of the phase matching point, transmission loss of a core guided mode varies strongly with changes in the analyte refractive index (see the upper part of Fig. 3.2(c)).

We would like to point out that what is identified as a "core mode" in all the figures in this paper is in fact a waveguide supermode that includes both the core guided mode and plasmonic contribution. Since the plasmon mode is extremely lossy, only a small mixing of this mode with the core mode is necessary to achieve sensing. We found pertinent to also show on the graphs what a plasmonic mode looks like near the phase matching point, although this mode by itself is not used in our sensing arrangements. Depending on the designs, the plasmon contribution to the evanescent tail of a core mode is not always visible on the field distribution plots as only the real components of the modes are truly phase matched.

The simplest mode of operation of a waveguide-based SPR sensor is detection of small changes in the bulk refractive index of an analyte. There are two main modalities of SPR detection - amplitude based and spectral based. In both methodologies sensing is enabled through detection of changes in the location of a sharp plasmonic loss peak which spectral position is strongly dependent on the value of the ambient refractive index. In the amplitude based approach, all the amplitude measurements are performed at a single wavelength near the center of a plasmonic peak. The advantage of this method is its simplicity and low cost, as no spectral manipulation is required. The disadvantage is a smaller dynamic range and lower sensitivity when compared to the wavelength interrogation approach, in which the whole transmission spectra are taken and compared before and after the change in the analyte has occurred.

We start by describing a single wavelength, amplitude based detection method. We define $\alpha(\lambda,n_a)$ to be the transmission loss of a core mode as a function of the wavelength and refractive index of an analyte n_a. Considering P_0 to be the power launched into the fiber core mode, the power detected after propagation along the sensor of length L will be $P(L,\lambda,n_a) = P_0 exp(-\alpha(\lambda,n_a)L)$. For the operating wavelength λ, amplitude sensitivity to the small changes in the analyte refractive index Δn_a can then be defined (and measured) as $S_A(\lambda)[RIU^{-1}]|_{\Delta n_a \to 0} = (P(L,\lambda,n_a + \Delta n_a) - P(L,\lambda,n_a))/P(L,\lambda,n_a)/\Delta n_a$. Sensor length L is typically limited by the modal transmission loss. A reasonable choice of a sensor length is $L = 1/\alpha(\lambda,n_a)$, which is $\sim 1cm$ range for the planar multilayer-based sensor described in this section. Such a choice of sensor length results in a simple definition of sensitivity for the small changes in the analyte refractive index

$$S_A(\lambda)[RIU^{-1}] = \frac{1}{P(L,\lambda,n_a)} \frac{\partial P(L,\lambda,n_a)}{\partial n_a} = -\frac{1}{\alpha(\lambda,n_a)} \frac{\partial \alpha(\lambda,n_a)}{\partial n_a}. \qquad (3.4)$$

In the lower part of Fig. 3.2(c) we present the amplitude sensitivity of the proposed planar photonic crystal waveguide-based SPR sensor. Maximal sensitivity is achieved at 673 nm and is equal to 112 RIU^{-1}. It is typically a safe assumption that 1% change

in the transmitted intensity can be detected reliably, which leads to a sensor resolution of $8.9 \cdot 10^{-5}$ RIU. This 1% criterion will be used throughout the paper to compare the sensors response.

In the wavelength interrogation mode, changes in the analyte refractive index are detected by measuring displacement of a plasmonic peak λ_{peak}. In this case, sensitivity is defined as

$$S_\lambda[nm \cdot RIU^{-1}] = \frac{d\lambda_{peak}(n_a)}{dn_a}. \tag{3.5}$$

In the case of a planar photonic crystal waveguide-based SPR sensor we find that the corresponding spectral sensitivity is 2300 nm·RIU^{-1}. Assuming that a 0.1 nm change in the position of a resonance peak can be detected reliably, a sensor resolution of $4.3 \cdot 10^{-5}$ RIU is obtained. The sensor length in this case is $\sim$ 1 cm.

3.4 SPR sensors using photonic crystal Bragg fibers

In this section, we propose two distinct approaches for fiber-based SPR sensing in aqueous solutions using photonic crystal Bragg fibers. In both cases, a thin gold layer is deposited on the outer surface of a Bragg fiber in direct contact with an analyte. By tailoring the dispersion relation of the fundamental core guided mode of a Bragg fiber, the phase matching condition is obtained at various wavelength in the visible and near-IR.

3.4.1 Large solid core Bragg fiber-based sensor

The first design approach consists of using the leaky fundamental Gaussian-like core mode of a Bragg fiber, and lowering its effective refractive index towards that of a plasmon by the proper choice of a fiber reflector and a fiber core size. The choice of the fundamental Gaussian-like core mode over the higher order modes is motivated by its

optimal spatial overlap with the common Gaussian laser sources. Moreover, when a sufficiently long Bragg fiber is used, effectively single mode regime of operation can be achieved by radiation of higher order modes, thus reducing the overall noise limit of a sensor. In particular, we consider solid core photonic crystal Bragg fibers made of two

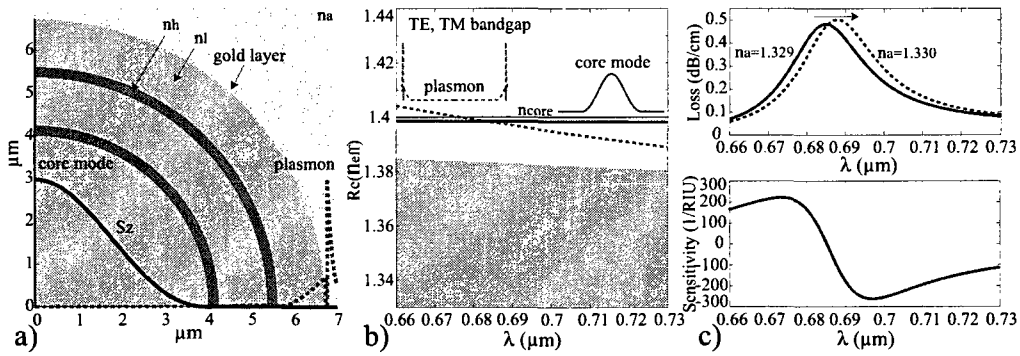

FIG. 3.3 – *Large solid core photonic crystal Bragg fiber-based SPR sensor. a) Schematic of a sensor. Low refractive index core is surrounded by a concentric photonic crystal reflector. Outside, the reflector is goldplated for plasmon excitation. Gold layer is bordered by aqueous analyte. Energy flux distribution across the fiber cross section is shown with a solid curve for the fundamental core mode, and with a dashed curve for the plasmonic mode. b) Band diagram of sensor modes. Dispersion relation and field distribution of the fundamental core mode (thick solid curve), and plasmonic mode (dashed curve). Common part of the TE, TM bandgaps of a periodic planar reflector is shown as a clear region, while gray regions correspond to the continuum of the bulk reflector states. c) Upper part: solid curve shows loss of the fundamental core mode near the phase matching point with a plasmon at which modal loss peaks. Dashed line shows shift of the modal loss curve when refractive index of an analyte is varied. Lower part: dependence of the sensor amplitude sensitivity on wavelength.*

materials with refractive indices $n_l = 1.40$ and $n_h = 1.60$. Prototypes of such fibers have been recently fabricated in our group by using a poly(vinylene difloride)/polycarbonate (PVDF/PC) and poly(methyl methylacrylate)/polystyrene (PMMA/PS) material combinations (Gao et al., 2006). In such fibers, the solid core of refractive index n_l is surrounded by N alternating high and low refractive index reflector layers of thicknesses d_l, and d_h. A typical choice of the reflector layer thicknesses is according to the quarter wave relation (3.1), where λ_c defines the center wavelength of the Bragg reflector bandgap,

and $n_{eff}(\lambda_c)$ is the desired effective refractive index of a core mode at that wavelength. This choice of the reflector parameters, only guarantees efficient bandgap guidance at λ_c of a mode with effective refractive index $n_{eff}(\lambda_c)$, however, it does not guarantee the existence of such a mode. As it will be detailed in what follows, one effective way of positioning a core mode dispersion relation inside of a fiber bandgap is by varying the fiber core diameter d_c. In a large core diameter Bragg fiber where $d_c \gg \lambda_c$, the effective refractive index of the fundamental core mode is close to that of a core material. By decreasing the fiber core size, one can considerably reduce the core mode effective refractive index.

With the choice of a desired phase matching λ_c and an approximation of the $n_{eff}(\lambda_c)$ performed using equation (3.2), we are still left with two free parameters which are the number of layers N in a Bragg reflector, and the fiber core size d_c. In metallized Bragg fibers, guided modes incur additional losses due to high absorption of the metal film. When operating within the bandgap of a Bragg fiber, fields of a leaky core mode decay exponentially fast into the periodic reflector. Thus, modal presence in the metallized region also decreases exponentially with the number of reflector layers. From this we conclude that variation in the number of reflector layers will primarily effect the core mode propagation loss.

We now investigate in more details the effect of a core size on the modal structure of an SPR sensor. First, we consider Bragg fiber sensor having large core diameter $d_c = 8\,\mu$m, operating in the vicinity of $\lambda_c = 740$ nm, and featuring a 4 layer reflector plated with a 40 nm thick layer of gold (see Fig. 3.3(a)). Reflector layer thicknesses are chosen to be $d_l = 1133$ nm, $d_h = 235$ nm. In Fig. 3.3(b) we present the band diagram of thus defined Bragg fiber sensor. Common TM, TE bandgap of a corresponding infinitely periodic Bragg reflector is presented as a clear region, while gray regions signify a continuum of the reflector bulk states. For a large core photonic crystal Bragg fiber, the effective refractive index of the lowest loss leaky mode (thick solid line) is close to that of the

refractive index of a core material (thin solid line). The dispersion relation of a plasmon mode is shown as thick dashed line. The dispersion relations of the core guided and plasmonic modes near λ_c are positioned well inside the reflector band gap by its proper design. Therefore, the fundamental core mode (solid curve in Fig. 3.3(a)) is well confined within the Bragg fiber core, while the plasmon mode (dashed curve in Fig. 3.3(a)) is mostly confined to the metal coating and the last reflector layer. Phase matching between the core and plasmonic modes is achieved at $\lambda = 684$ nm.

In the upper plot of Fig. 3.3(c) propagation loss of a core mode is presented as a function of wavelength. As seen from this figure, core mode propagation loss peaks at the wavelength of phase matching with the plasmon mode due to an efficient energy transfer from the core mode into the highly absorbing plasmon. In the lower part of Fig. 3.2(c) we present amplitude sensitivity (3.4) of the proposed large solid core Bragg fiber-based SPR sensor. Maximal sensitivity is achieved at 697 nm and is equal to 262$\cdot$ RIU^{-1}. The sensor resolution reaches $3.8 \cdot 10^{-5}$ RIU based on the last section assumption. In the case of a large solid core Bragg fiber-based SPR sensor we find that the corresponding spectral sensitivity (3.5) is 3000 nm$\cdot$ RIU^{-1}. For a wavelength-based detection, a sensor resolution of $3.3 \cdot 10^{-5}$ RIU is obtained. Sensor length in this case is $\sim$ 10 cm.

3.4.2 Small solid core Bragg fiber-based sensor

In the second design we explore the possibility of considerably reducing the effective refractive index of a core mode by reducing the fiber core size. This enables plasmonic excitation at longer wavelengths in the near-IR. Thus, with the same overall structure of the Bragg reflector as in the prior case, by reducing the fiber core diameter to $d_c = 2.2$ μm, plasmonic excitation at the interface with aqueous analyte is demonstrated at 836 nm. In Fig. 3.4(a) we show the cross section of a small solid core photonic crystal Bragg fiber sensor, and the energy flux distributions in its leaky fundamental core mode

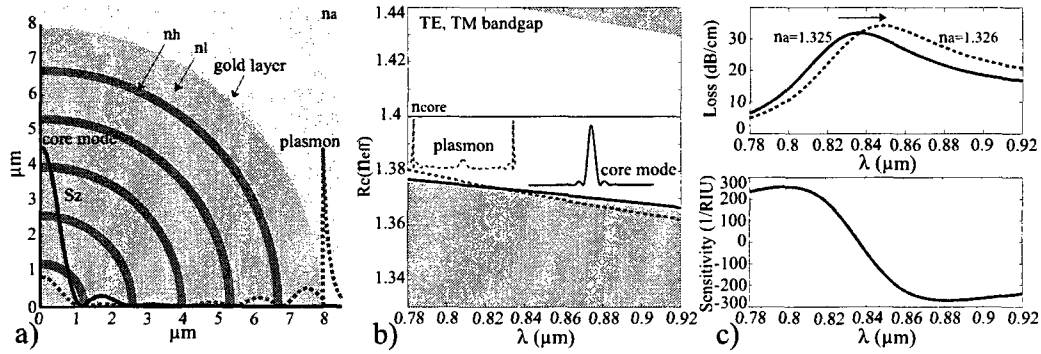

FIG. 3.4 – *Small solid core photonic crystal Bragg fiber-based SPR sensor. a) Schematic of a sensor. Low refractive index core is surrounded by a concentric photonic crystal reflector. Outside, the reflector is goldplated for plasmon excitation. Gold layer is bordered by aqueous analyte. Energy flux distribution across the fiber cross section is shown with a solid curve for the fundamental core mode, and with a dashed curve for the plasmonic mode. b) Band diagram of sensor modes. Dispersion relation and field distribution of the fundamental core mode (thick solid curve), and plasmonic mode (dashed curve). Common part of the TE, TM bandgaps of a periodic planar reflector is shown as a clear region, while gray regions correspond to the continuum of the bulk reflector states. c) Upper part: solid curve shows loss of the fundamental core mode near the phase matching point with a plasmon at which modal loss peaks. Dashed line shows shift of the modal loss curve when refractive index of an analyte is varied. Lower part: dependence of the sensor amplitude sensitivity on wavelength.*

and plasmonic mode. Although reflector layer thicknesses are the same as in the prior case (see Fig. 3.3(a)), the total number of layers is increased to 10 in order to reduce core mode radiation loss. In Fig. 3.4(b) we present the band diagram for this design. Common TM, TE bandgap of a corresponding infinitely periodic Bragg reflector is presented as a clear region, while gray regions signify the continuum of reflector bulk states. In a small core photonic crystal Bragg fiber, effective refractive index of the lowest loss leaky mode (thick solid line) can be considerably smaller than the refractive index of the core bulk material (thin solid line). The dispersion relation of the plasmon mode is shown as thick dashed line. Moreover, the dispersion relation of the core guided mode is shifted towards lower edge of the reflector bandgap. Therefore, the core mode (solid curve in Fig. 3.4(a)) and plasmonic mode (dashed curve in Fig. 3.4(a)) are not strongly confined, penetrating

significantly into the reflector region. Phase matching between the core and plasmonic modes is achieved at $\lambda = 836$ nm.

In the upper plot of Fig. 3.4(c) propagation loss of the core mode is presented as a function of the wavelength. As seen from this figure, it peaks at the wavelength of phase matching with the plasmon mode. In the lower part of Fig. 3.4(c) we present amplitude sensitivity (3.4) of the proposed small solid core Bragg fiber-based SPR sensor. Maximal sensitivity is achieved at 882 nm and is equal to $269 \cdot \text{RIU}^{-1}$. An amplitude interrogation yields a sensor resolution of $3.7 \cdot 10^{-5}$ RIU. Finally, we find that the corresponding spectral sensitivity (3.5) is 12000 nm$\cdot$ RIU^{-1}, leading to a resolution of $8.3 \cdot 10^{-6}$ RIU. Sensor length in this case is sub-cm.

3.4.3 Analyte-filled hollow-core Bragg fiber-based sensor

When designing fiber-based SPR sensors in the near-IR one faces a difficult problem of phase matching a plasmon and a core guided mode. The reason for such difficulty is that in this spectral region the effective refractive index of a plasmon becomes very close to that of an analyte, which for aqueous solutions, for example, is $n_a \sim 1.32$. As described in the previous section, to lower effective refractive index of a core guided mode to that of a plasmon, one can use a small solid core Bragg fiber with a properly positioned bandgap region. In that case, however, fiber core size becomes too small for convenient coupling. To resolve this problem we suggest using a large analyte-filled hollow core Bragg fiber shown in Fig. 3.5(a). In this case, as described earlier, the effective refractive index of the core mode (thick solid line in Fig. 3.5(b)) is close and somewhat smaller than the refractive index of the core material (analyte). In turn, the plasmon refractive index (dashed line in Fig. 3.5(b)) is close and somewhat larger than refractive index of the analyte. To enable phase matching between the core mode and a plasmon, one has to force the core mode to cross over the dispersion relation of an analyte. As detailed

in (Engeness et al., 2003) to force such a crossing, one has to introduce a defect into the structure of a reflector so as to induce anticrossing of the core mode with a reflector defect state (marked as a dashed circular region in Fig. 3.5(b)). The particular sensor

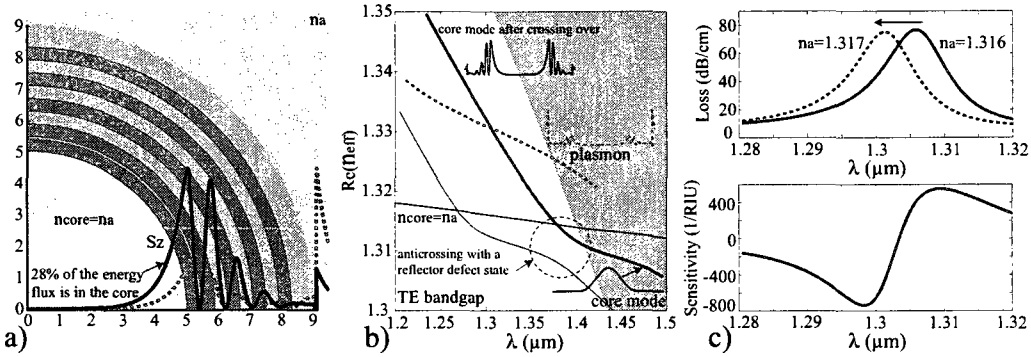

FIG. 3.5 – *Analyte-filled large hollow core photonic crystal Bragg fiber-based SPR sensor. a) Schematic of a sensor. Analyte-filled hollow core is surrounded by a concentric photonic crystal reflector. Outside, the reflector is goldplated for plasmon excitation. Gold layer is bordered by aqueous analyte. Energy flux distribution across the fiber cross section is shown with a solid curve for the fundamental core mode, and with a dashed curve for the plasmonic mode. b) Band diagram of sensor modes. Dispersion relation of the fundamental core mode crossing over the analyte light line (thick solid curve), and plasmonic mode (dashed curve). TE bandgap of a periodic planar reflector is shown as a clear region, while gray regions correspond to the continuum of the bulk reflector states. c) Upper part: solid curve shows loss of the crossed-over core mode near the phase matching point with a plasmon at which modal loss peaks. Dashed line shows shift of the modal loss curve when refractive index of an analyte is varied. Lower part: dependence of the sensor amplitude sensitivity on wavelength.*

geometry implementing this design principle is presented in Fig. 3.5(a). In this sensor, analyte-filled fiber core of diameter $d_c = 10\mu$m is surrounded by a 10 layer reflector with alternating refractive indices $n_l = 1.4$, and $n_h = 1.6$. All the low refractive index layers, with the exceptions of the second and tenth layers, have thicknesses $d_l = 373$ nm, while all the high refractive index layers have thicknesses of $d_h = 435$ nm. On the outside, the reflector is plated with a 40nm gold layer. Two defects are incorporated into the structure of the Bragg reflector. The first defect is introduced into the outer layer by doubling its thickness to 870 nm. This defect is introduced to get rid of an unwanted surface state on

the fiber-metal-analyte interface. The second defect is introduced into the second layer by reducind its thickness to 47 nm. The high refractive index defect created by the first three layers of the reflector attracts a localized state that causes anticrossing with the core mode, thus forcing the core mode to cross over the dispersion relation of the analyte, and enabling phase matching with a plasmon.

The main disadvantage of this plasmon excitation mechanism is that the intensity distribution in a crossed-over core mode, stops being Gaussian-like. In fact, such a mode is evanescent in the analyte region, hence, it becomes somewhat difficult to excite with a common Gaussian laser source. However, when the plasmon dispersion relation is very close to that of the analyte (as it is the case in the near-IR), then evanescent tail of a crossed-over core mode can extend substantially into the analyte filled core region, thus simplifying considerably coupling to such a mode. For example, design of Fig. 3.5(a) enables phase matching with a plasmon near 1306 nm (as seen from Fig. 3.5(b)). At this wavelength a crossed-over core mode still has 28% of its energy concentrated in the analyte filled hollow fiber core.

We conclude with sensitivity analysis of the proposed near-IR SPR sensor. In the lower part of Fig. 3.5(c) we present sensor amplitude sensitivity (3.4). Maximal sensitivity is achieved at 1298 nm and is equal to $725 \cdot \mathrm{RIU}^{-1}$. Once again, assuming that 1% change in the transmitted intensity can be detected reliably, this leads to a sensor resolution of $1.4 \cdot 10^{-5}$ RIU. Finally, we find that the corresponding spectral sensitivity (3.5) is $4300\ \mathrm{nm} \cdot \mathrm{RIU}^{-1}$. A spectral interrogation leads to a sensor resolution of $2.3 \cdot 10^{-5}$ RIU. Sensor length in this case is sub-cm.

3.5 SPR sensors using microstructured photonic crystal fibers

In the previous section we have presented several design strategies for the SPR sensors based on photonic crystal Bragg fibers. In principle, any photonic bandgap fiber can be used in place of a Bragg fiber to develop such sensors. In this section we present an example of a SPR sensor based on a solid core honeycomb photonic crystal fiber. As core guiding in such a fiber is analogous to core guiding in a small solid core Bragg fiber discussed earlier, our presentation will be brief. In Fig.3.6(a) the schematic of a

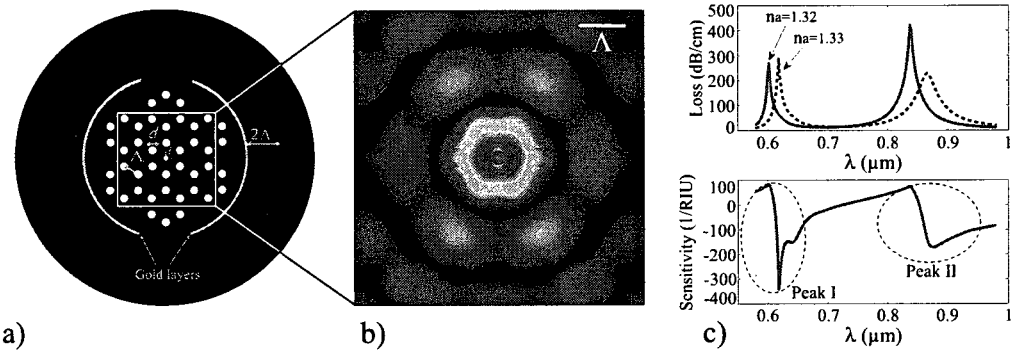

FIG. 3.6 – *Solid core honeycomb photonic crystal fiber-based SPR sensor. a) Schematic of a sensor. Solid core having a small central hole is surrounded by a honecomb photonic crystal reflector. Two large channels are integrated to implement analyte access to the fiber reflector region. Channels are goldplated for plasmon excitation. Gold layer is bordered by aqueous analyte. The purpose of the ring surrounding the channels is to add mechanical rigidity to the fiber and enable microfluidic manipulations. b) Energy flux distribution across the fiber crossection is shown for the fundamental core mode. c) Upper part: solid curve shows loss of the fundamental core mode near the phase matching point with a plasmon at which modal loss peaks. Dashed line shows shift of the modal loss curve when refractive index of an analyte is varied. Lower part: dependence of the sensor amplitude sensitivity on wavelength.*

honeycomb photonic crystal fiber-based SPR sensor is presented. Design parameters are chosen as follows, the center to center distance between adjacent holes is $\Lambda = 1.33\ \mu$m, the cladding hole diameter is $d = 0.6\Lambda$, the diameter of the hole in the core center is $d_c = 0.45\Lambda$. The central hole in the fiber core lowers its effective refractive index

compared to that of a silica cladding. The fiber is made of silica glass with refractive index $n_{glass} = 1.45$, the core and cladding holes are filled with air $n_{air} = 1$, while the large semi-circular channels are plated with a ~ 40 nm thick layer of gold and filled with aqueous analyte $n_a \sim 1.33$. With these parameters, the fiber core supports a leaky core mode confined by the bandgap of the honeycomb reflector. Guided by the bandgap of the fiber reflector, core mode effective refractive index can be considerably lower than that of the silica material. In addition, similarly to the case of a photonic crystal Bragg fiber, radiation loss of the bandgap guided core mode can be reduced by adding more layers to the honeycomb reflector. The main reason why we chose a honeycomb structure of the fiber reflector is because it enables a large photonic bandgap (Murao et al., 2006; Barkou et al., 1999), thus simplifying phase matching of the core guided and plasmonic modes.

Unlike planar metal/dielectric interface that supports a single plasmonic excitation, metallized microstructured fibers can support multiple plasmonic modes (Hassani and Skorobogatiy, 2006; Hassani et al., 2008a). Thus, when tracking losses of a core guided mode as a function of wavelength one typically observes several plasmonic peaks corresponding to the points of phase matching between the core mode and various plasmonic modes. In principle, simultaneous detection of changes in several plasmonic peaks can improve sensor sensitivity. For the case of a honeycomb photonic crystal fiber-based sensor we observe two plasmonic peaks (see the upper part of Fig.3.6(c)), one located at 600 nm and another at 840 nm. In the lower part of Fig. 3.6(c) we present amplitude sensitivity of the sensor as defined by (3.4). Maximal amplitude sensitivity (3.4) at the first peak is $340 \cdot \text{RIU}^{-1}$, while at the second peak it is $170 \cdot \text{RIU}^{-1}$. Based on the same 1% criterion, the sensor resolutions at the two peaks are $2.9 \cdot 10^{-5}$ RIU and $5.9 \cdot 10^{-5}$ RIU, respectively. Finally, spectral resolutions as defined by (3.5) at the two peaks are 1600 nm$\cdot$ RIU^{-1}, and 2800 nm$\cdot$ RIU^{-1}. The proper detection of a 0.1 nm change in the position of a resonance peak yields sensor resolutions at the two peaks of $6.3 \cdot 10^{-5}$ RIU, and $3.6 \cdot 10^{-5}$ RIU, respectively. Sensor lengths in both cases is sub-mm.

3.6 Conclusion

In conclusion, we have presented a novel approach to design a waveguide-based SPR sensor, where the Gaussian-like mode of an effectively single mode photonic crystal waveguide is phase matched at any desirable wavelength to a surface plasmon propagating along the metallized part of such a waveguide. The operating wavelength of such sensors can be anywhere from the visible to near-IR. Moreover, a wide variety of material combinations can be used to design such a sensor as there is no limitation on the value of the waveguide core refractive index. Finally, coupling strength between the waveguide core and plasmon modes can be varied by changing the number of the intermediate reflector layers, which also permits designing the overall sensor length.

The methodology for the photonic crystal waveguide-based SPR sensor design is quite general and its particular implementation can be based on metal plated planar integrated photonic crystal waveguides, Bragg fibers or microstructured photonic crystal fibers. Particularly, one starts with a choice of an operational wavelength λ_c. Then, the plasmon effective refractive index $n_{eff}(\lambda_c)$ at λ_c is approximated by its value for the plasmon excitation on a planar metal-analyte interface (3.2). Then, the photonic bandgap of a waveguide reflector at λ_c is designed to be centered in the vicinity of $n_{eff}(\lambda_c)$. By varying the waveguide core size (or by varying the geometry of a core), one can shift the dispersion relation of a core mode towards that of a plasmonic mode until phase matching occurs at λ_c. Sensor length can be changed by varying the number of layers in a photonic crystal reflector, with more efficient reflectors resulting in the longer sensors.

Finally, we have presented examples of the aqueous SPR sensors based on the planar photonic crystal waveguide, solid and analyte filled Bragg fibers, as well as solid core microstructured photonic crystal fiber. Amplitude sensitivity of the proposed designs was as high as $725 \cdot \mathrm{RIU}^{-1}$. Assuming that 1% change in the transmitted intensity can be

detected reliably, sensor resolution as low as $1.38 \cdot 10^{-5}$ RIU was demonstrated. Spectral sensitivity of the proposed designs was as high as 12000 nm$\cdot$ RIU^{-1}. Assuming that a 0.1 nm change in the position of a plasmonic peak can be detected reliably, sensor resolution as low as $8.3 \cdot 10^{-6}$ RIU was demonstrated. Sensor lengths in our examples varied from sub-mm to $\sim 10cm$. For measuring changes in the aqueous analyte, sensitivities of our fiber designs are comparable to or even surpass those of the best existing waveguide-based sensor designs (Homola et al., 1999).

CHAPITRE 4

ARTICLE 3: POROUS POLYMER FIBERS FOR LOW-LOSS TERAHERTZ GUIDING

Alireza Hassani, Alexandre Dupuis, and Maksim Skorobogatiy [1].

This chapter including next two chapters discuss the design of MOF based plasmonic-like sensors at THz which was not exist before. To design a waveguide based plasmonic-like sensor at THz, two challenges should be addressed which are proposing a low loss waveguide with tunable modal effective index and finding a material naturally support surface plasmon waves at THz. The following paper addresses the design of two low loss waveguides operating at THz, while The plasmonic-like excitation and design of plasmonic-like sensors at THz will be presented at the two next articles. Two designs of effectively single mode porous polymer fibers for low-loss guiding in THz regime are proposed. The first one is a fiber of several wavelengths in diameter containing an array of subwavelength holes in a dielectric rod. Our simulation for this fiber shows that because the continuity of displacement field at the boundary of air holes, the major part of the THz power can be confined inside subwavelength holes with optimum sizes between $\sim 0.1-0.2\lambda$, resulting in suppressing the material absorption loss by factor of ~ 15. Total fiber loss of less than 10 dB/m and fiber bandwidth of $\sim$1 THz is predicted for the porous fibers with subwavelength holes. Moreover, the size and number of airhole layers in porous fibers also enables tuning of the modal effective index of the core mode, thus facilitating the phase matching between the core mode and surface plasmon waves. The second proposed design details a large diameter hollow core PBG Bragg fiber made of solid film layers suspended in air by a network of circular bridges. Although our simulations predict the total loss of less than 5 dB/m for the Bragg fiber, the porous

subwavelength fiber will be used in the design of the THz waveguide based SPR-like sensor, in chapter 6, because a) the Bragg fiber has smaller bandwidth, ~ 0.1 THz, with compare to that of porous fiber, b) tuning the modal effective index in the porous fiber is much easier than the Bragg fiber and c) the fabrication of the porous subwavelength is easer.

1. Department Engineeing Physics, École Polytechnique de Montréal, Montréal Canada

4.1 Abstract

We propose two designs of effectively single mode porous polymer fibers for low-loss guiding of terahertz radiation. First, we present a fiber of several wavelengths in diameter containing an array of sub-wavelength holes separated by sub-wavelength material veins. Second, we detail a large diameter hollow core photonic bandgap Bragg fiber made of solid film layers suspended in air by a network of circular bridges. Numerical simulations of radiation, absorption and bending losses are presented; strategies for the experimental realization of both fibers are suggested. Emphasis is put on the optimization of the fiber geometries to increase the fraction of power guided in the air inside of the fiber, thereby alleviating the effects of material absorption and interaction with the environment. Total fiber loss of less than 10 dB/m, bending radii as tight as 3 cm, and fiber bandwidth of $\sim$ 1 THz is predicted for the porous fibers with sub-wavelength holes. Performance of this fiber type is also compared to that of the equivalent sub-wavelength rod-in-the-air fiber with a conclusion that suggested porous fibers outperform considerably the rod-in-the-air fiber designs. For the porous Bragg fibers total loss of less than 5 dB/m, bending radii as tight as 12 cm, and fiber bandwidth of $\sim$ 0.1 THz are predicted. Coupling to the surface states of a multilayer reflector facilitated by the material bridges is determined as primary mechanism responsible for the reduction of the bandwidth of a porous Bragg fiber. In all the simulations, polymer fiber material is assumed to be Teflon with bulk absorption loss of 130 dB/m.

4.2 Introduction

Terahertz radiation, with wavelengths from 30 to 3000 microns, has big potential for applications such as biomedical sensing, noninvasive imaging and spectroscopy. On one hand, the rich spectrum of THz spectroscopy has allowed for the study and label-free de-

tection of proteins (Xu et al., 2006), explosives (Cook et al., 2005), pharmaceutical durgs (Clare J. Strachan, 2005), and the hybridization of DNA (Nagel et al., 2002). On the other hand, the substantial subsurface penetration of terahertz wavelengths has driven a large amount of work on THz imaging (Chan et al., 2007). Applications range from non-destructive quality control of electronic circuits (Kiwa et al., 2003) to the spatial mapping of specific organic compounds for security applications (Kawase et al., 2003). Although THz radiation is strongly absorbed by water, the combination of spectroscopy and imaging has been used to demonstrate the differentiation of biological tissues (Löffler et al., 2001). Terahertz sources are generally bulky and designing efficient THz waveguides, in order to remotely deliver the broadband THz radiation, would be a big step towards commercialization of compact and robust THz systems. However, almost all materials are highly absorbent in the THz region making design of low loss waveguides challenging. Even air might exhibit high absorption loss if the water vapor content in it is not controlled. Before discussing porous fiber designs, we begin with a review of the recent advances in THz waveguides.

Whereas the losses of circular metallic tubes (Gallot et al., 2000), like stainless steel hypodermic needles, have a propagation loss on the order of 500 dB/m, recent techniques have considerably reduced the loss. On one hand, the use of thin metal layers on the inner surface of dielectric tubes (Harrington et al., 2004; Themistos et al., 2007; Ito et al., 2007), a technique which was initially developed for guiding CO_2 laser light, has been shown to successfully guide in the THz region. A thin Cu layer in a polystyrene tube10 and a thin Ag layer in a silica tube (Ito et al., 2007) have respectively been shown to have losses of 3.9 dB/m and 8.5 dB/m. On the other hand, surface plasmon mediated guidance on metallic wires has recently raised interest (Wang and Mittleman, 2004) because of the lowest predicted propagation losses (Cao and Jahns, 2005) of 0.9 dB/m. However, it is very difficult to excite the plasmons because their azimuthal polarization. Typical coupling losses are very high with less than 1% of the incident power transmit-

ted; even with the development of specialized antennas only 50% coupling is achieved. Furthermore, the bending losses are very high and the surface plasmon is a very delocalized mode (Cao and Jahns, 2005). Since the mode extends many times the diameter of the wire into the ambient air, modes of these waveguides are expected to couple strongly to the cladding environment. For higher coupling efficiency, and highly confined mode, hollow core waveguides are preferable. As an additional advantage, hollow waveguides offer the possibility of putting an analyte directly into the waveguide core, thus dramatically increasing sensitivity in spectroscopic and sensor applications.

Because of the high absorption losses in dielectrics, a variety of guiding mechanisms have been studied in order to reduce the propagation losses. On one hand, the resonance in the dielectric constant of ferroelectric polyvinylidene fluoride (PVDF) has been exploited for demonstrating a hollow core $n_{core} < 1$ waveguide and a hollow core Bragg fiber (Hidaka et al., 2005; Skorobogatiy and Kabashin, 2007) with losses lower than 10 dB/m. However, PVDF is a semi-crystalline polymer that has many phases and a complicated poling procedure is required for achieving the ferroelectric state. Another hollow core design was discussed by Yu et al. (jin Yu et al., 2007) is of a hollow Bragg fiber where solid layers are separated by air and supported by a network of solid supports, similarly to the air/silica Bragg fibers for the near-IR applications described in (Poli et al., 2007). Other photonic crystal structures have been tried (Park et al., 2002; Goto et al., 2004), but the absorption in a solid core remains considerable.

In yet another approach, many sub-wavelength waveguides have been developed (Jamison et al., 2000; Chen et al., 2006; Nagel et al., 2006). A solid sub-wavelength rod acts as a high refractive index core with surrounding air acting as a lower refractive index cladding. The field of the guided mode extends far into the surrounding air resulting in low absorption loss. Main disadvantage of rod-in-the-air subwavelength designs is that most of the power is propagated outside of the waveguide core, thus resulting in strong coupling to the environment, which is typically unwanted in power guiding applications.

Alternatively, Nagel et al. (Nagel et al., 2006) have demonstrated that addition of a sub-wavelength hole within a solid core increases the guided field within the air hole, thus reducing the absorption losses. Main disadvantage of a subwavelength hole design is that most of the power is still conducted in the high loss material of a core.

While losses of all-dielectric fibers are currently higher than those of hollow core metallized fibers, we believe that porous fiber geometry of a relatively large diameter could be designed to compete with the hollow metallized fibers. The driving factor for the development of porous all-dielectric fibers is that such fibers can be fabricated from a single material using standard fiber drawing techniques, which is, potentially, simpler than fabrication of metal coated waveguides due to omission of a coating step.

In this paper we present two designs of highly porous fibers that rely on two different guiding mechanisms – the total internal reflection (TIR) and photonic bandgap (PBG) guidance. The geometries of these structures are optimized to increase the fraction of power guided in the air inside of a fiber, thereby reducing the absorption losses and interaction with the environment. The paper is organized as follows. We first present a TIR guiding sub-wavelength fiber containing multiple sub-wavelength holes (see Fig. 4.1(a)), and compare its performance with that of a subwavelength rod-in-the-air fiber. We then present a PBG guiding porous Bragg fiber (see Fig. 4.1(b)) featuring a periodic array of concentric material layers separated by air, and supported with a network of circular bridges. Finally we conclude with a summary of the findings.

4.3 Porous fibers with multiple sub-wavelength holes

We start by reminding the reader briefly the optical properties of porous TIR fibers which were recently detailed in (Hassani et al., 2008b). Our goal is to then perform a comprehensive comparative analysis of TIR porous fibers, sub-wavelength rod fibers, and po-

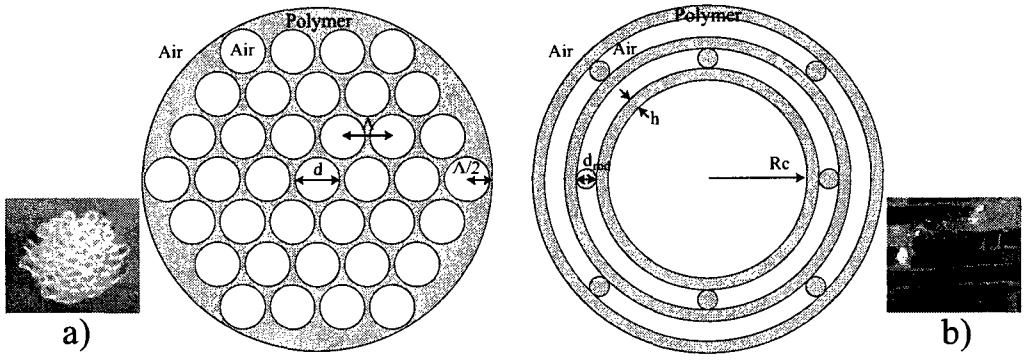

FIG. 4.1 – *Schematics of two porous fibers studied in this paper. a) Cross-section of a porous fiber with multiple sub-wavelength holes of diameter* $d \ll \lambda$ *separated by pitch* Λ. *b) Cross-section of a porous Bragg fiber featuring periodic sequence of concentric material rings of thickness* h *suspended in air by a network of circular bridges of diameter* d_{rod}.

rous TIR and photonic band gap Bragg fibers - all the excellent candidates for low loss guiding in THz regime.

The first structure we consider consists of a polymer rod having a hexagonal array of air holes (see Fig. 4.1(a)). Note that a periodic array of holes is not necessary as the guiding mechanism remains total internal reflection and not the photonic bandgap effect. The main task is to design a fiber having a relatively large core diameter for efficient light coupling, while at the same time having a significant fraction of light inside of the fiber air holes to reduce losses due to absorption of a fiber material, as well as to reduce interaction with the environment. In all the simulations presented in this section porous fiber is single mode. Experimentally, such porous fibers can be realized by capillary stacking and drawing technique (see an inset of Fig. 1(a)).

For the fiber material we assume a polymer of refractive index $n_{mat} = 1.5$, which is a typical value for most polymers at 1 THz. Refractive index of air is 1. First, we consider the fiber having 4 layers of subwavelength holes of two possible sizes $d/\lambda = [0.1, 0.15]$,

where d is the hole diameter and λ is the operating wavelength. Center-to-center distance between the two holes (lattice pitch) is defined as Λ. Finally, fiber diameter is considered to be 9Λ. In the remainder of this section the air hole size is fixed for each design, while the thickness of the material veins is varied (larger d/Λ ratios correspond to thinner veins). Fully vectorial finite element method is used for the calculation of the eigen modes of a fiber. In our simulations, design wavelength is fixed $\lambda = 300$ μm (frequency of 1 THz), unless specified otherwise.

Figure 4.2 shows effective refractive index of the fundamental mode of a porous fiber versus d/Λ for the three cases $d/\lambda = [0.1, 0.15]$. When material vein thickness is reduced (larger d/Λ fractions), effective refractive index of the fundamental mode becomes much smaller than that of a polymer fiber material. As a result, a large fraction of the modal power is expelled into the sub-wavelength air holes and air cladding. Consider, in particular, the case of $d/\lambda = 0.1$. When reducing the vein thickness to 0 ($d/\Lambda \rightarrow 1$) from Fig. 4.2(a) we see that modal effective refractive index monotonically decreases until it saturates at a value ~ 1.045. This saturation happens as even in the case of zero vein thickness the fiber crossection features a network of disjointed, however, finite sized triangular shaped regions.

Insets (a) in Fig. 4.2(a) shows distributions of the power flux S_z in the fiber crossection for a design with $d/\lambda = 0.1$, and $d/\Lambda = 0.8$. As seen form the inset, the flux distribution has Gaussian-like envelope. As material veins in the case of $d/\Lambda = 0.8$ are very thin, it is not surprising to find that for this design a larger portion of the modal power is concentrated in the air holes. The fraction of power η guided in the air can be obtained by using distribution of the Pointing vector component S_z over the fiber crossection as:

$$\begin{aligned} \eta &= \int_{\text{air}} \mathrm{S_z} dA / \int_{\text{total}} \mathrm{S_z} dA \\ \mathrm{S_z} &\propto Re\,(\hat{z} \cdot \int_{\text{total}} dA\; E \times H^*) \end{aligned} \quad , \tag{4.1}$$

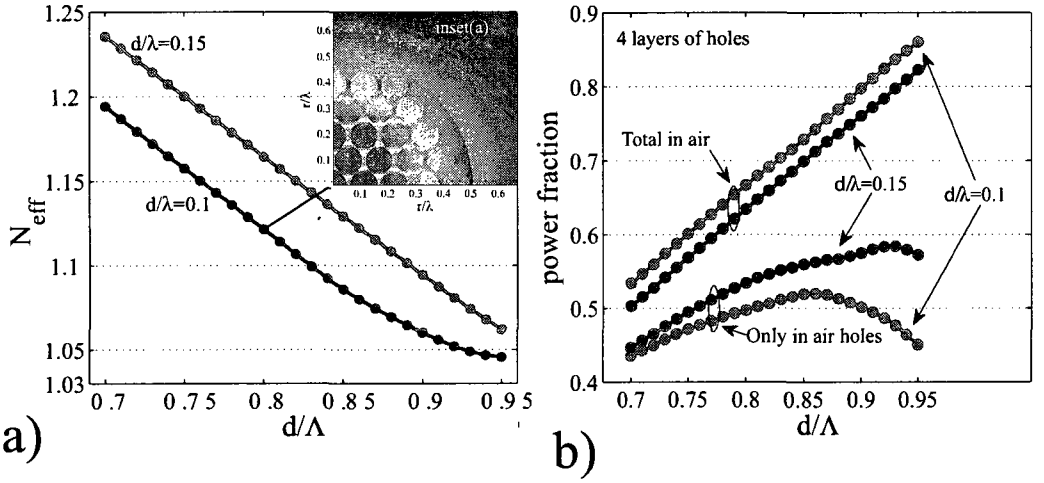

FIG. 4.2 – *a) Effective refractive index of the fundamental core mode versus* d/Λ *for the two fiber designs having hole diameters of* $d/\lambda = [0.1, 0.15]$. *For the fiber with* $d/\lambda = 0.1$, *distribution of the power flux in the waveguide crossection Sz is shown for* $d/\Lambda = 0.8$ *in the inset (a). b) Fraction of modal power guided in the air as a function of* d/Λ. *The two upper curves show the total power fraction in the air (air plus cladding) while the two lower curves indicate the power fraction in the air holes only.*

where "air" and "total" indicate integration over the air regions and the entire fiber cross-section, respectively, while E, H are the modal electric and magnetic fields. Fig. 4.2(b) shows the fraction of power guided in the air as a function of d/Λ for the two fibers with different air hole sizes. The two upper curves show the total power fraction in the air (air plus cladding), while the two lower curves indicate the fraction of power contained solely within the air holes. Consider now a particular case of $d/\lambda = 0.1$. As seeing from Fig. 4.2(b), as the pitch decreases (veins become thinner) the total modal power fraction in the air increases. The power fraction in the air holes inside of the fiber, however, achieves its maximum value at $d/\Lambda \simeq 0.86$. This behavior is relatively simple to rationalize. Indeed, thinning of the material veins beyond their optimal size leads to the reduction of the modal effective refractive index and stronger expulsion of the modal fields into the fiber air cladding, eventually resulting in the smaller modal power fraction

in the air holes of a fiber core. On the other hand, thickening of the material veins beyond their optimal size leads to higher concentration of the modal fields inside of the polymer veins, eventually also resulting in the smaller modal power fraction in the air holes of a fiber core. From Fig. 4.2(b) it follows that for a given size of the air holes d/λ, the d/Λ parameter can be optimized to increase the amount of power propagating inside of the porous fiber core, thus reducing the influence of cladding environment. Inversely, if the d/Λ is fixed, the air hole size d/λ can be also optimized to increase the amount of power propagating inside of the porous fiber. For the reference, existence of an optimal air hole size to maximize the fraction of power guided in the air was first described in the case of a single sub-wavelength air hole inside of a solid core waveguide (Nagel et al., 2006).

We now characterize absorption loss of the fundamental mode due to fiber material absorption. Particularly, the ratio of the modal absorption loss to the bulk material loss of a core material can be calculated using perturbation theory expression (Snyder and Love, 1983):

$$f = \frac{\alpha_{\text{mode}}}{\alpha_{\text{mat}}} = \frac{Re(n_{\text{mat}}) \int_{\text{mat}} |E|^2 \, dA}{Re\left(\hat{z} \cdot \int_{\text{total}} dA \, E \times H^*\right)}, \tag{4.2}$$

where α_{mat} is the bulk absorption losses of the core material (assuming that air has no loss). Figure 4.3(a) presents the normalized absorption loss of the fundamental core mode as a function of d/Λ. Not surprisingly, for higher air filling fractions (larger d/Λ) absorption loss is greatly reduced. For example, for a fiber with d/λ= 0.1, d/Λ = 0.95 the normalized absorption loss is $\sim$ 0.08. Considering that the fiber is made of a low loss polymer such as Teflon (Goto et al., 2004) with bulk absorption loss of α_{mat} = 0.3 $\text{cm}^{-1} \simeq$ 130 dB/m at 1 THz we obtain the fundamental mode loss α_{mode}= 10.4 dB/m.

Another important parameter to consider is radiation loss due to macrobending. In general, calculation of bending induced loss for microstructured fibers is not an easy task. In our case, however, due to Gaussian like envelope of the fundamental mode we can approximate our fiber as a low refractive index-contrast step-index fiber for which ana-

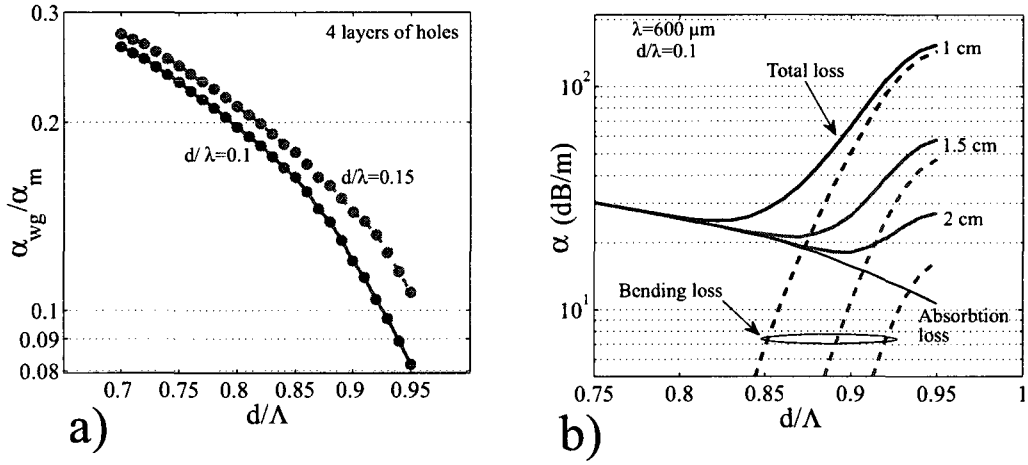

FIG. 4.3 – *a) Normalized absorption loss versus d/Λ for two porous fiber designs. b) Total of the bending and absorption losses versus d/Λ for the Teflon-based porous fiber with d/λ= 0.1 operating at 0.5 THz.*

lytical approximation of bending loss is readily available (Nielsen et al., 2004):

$$\alpha \cong \frac{\sqrt{\pi}}{8}\frac{1}{A_{eff}}\frac{1}{\beta(\beta^2-\beta_{cl}^2)^{1/4}}\frac{\exp\left(-\frac{2}{3}R_b(\beta^2-\beta_{cl}^2)^{3/2}\beta^{-2}\right)}{\sqrt{R_b(\beta^2-\beta_{cl}^2)\beta^{-2}+R_c}} \propto \frac{1}{\sqrt{\lambda R_b}}\exp(-\frac{R_b}{\lambda}\cdot const), \tag{4.3}$$

where modal propagation constant β is defined as $\beta = 2\pi n_{eff}/\lambda$, R_b is bending radius, R_c is a fiber core radius, and A_{eff} is the modal effective area defined as (Mortensen, 2002):

$$A_{\text{eff}} = \left[\int I(r)rdr\right]^2 \Big/ \left[\int I^2(r)rdr\right], \tag{4.4}$$

where $I(r) = |E_t|^2$ is the transverse electric field intensity distribution in the fiber crossection. As an example, consider porous fiber having d/λ= 0.1, and operated at λ = 600 μm (0.5 THz)(the longer operating wavelength, λ = 600 μm, shows a more challenging case for bending loss). In Fig. 4.3(b) we compare absorption, bending and total modal losses as a function of d/Λ design parameter. Thin solid curve represents straight fiber absorption loss assuming that the fiber is made of a Teflon polymer having 130 dB/m bulk absorption loss. Dashed curves show fiber macro-bending loss calculated

using (4.3) for 1 cm, 1.5 cm, and 2 cm values of the bending radii R_b. Finally, thick solid curves present total modal loss (the sum of absorption and bending losses). Interestingly, for very tight bends (bending radii of several cm and smaller) there exists an optimal design (in terms of d/Λ) that minimizes the total loss. Generally, for moderate air filling fractions $0.8 < d/\Lambda < 0.9$ the dominant loss mechanism is absorption loss due to field localization in the material core, whereas for high air filling fractions $d/\Lambda > 0.85$ bending loss dominates due to strong delocalization of the fundamental mode outside of the fiber core.

We conclude this section by comparing performance of a 3 layer porous fiber (Skorobogatiy et al., 2002)(with reducing one layers of holes) with that of a standard rod-in-the-air sub-wavelength fiber made of the same material (see Fig. 4.4). To make a fair comparison, we first design a rod-in-the-air fiber having the same absorption losses as a porous fiber, and then compare various propagation characteristics of the two fibers. Particularly, we consider porous fiber of Fig. 4.1(a) with $d/\lambda = 0.1$, $\lambda = 300$ μm. For every value of $0.7 < d/\Lambda < 0.95$ of a porous fiber, we then find a corresponding diameter D_r of a rod-in-the-air fiber so that the absorption losses of the two fibers are identical. For both fibers the core material is assumed to be Teflon polymer with $n_{mat} = 1.5$ and bulk absorption loss $\alpha_{mat} = 130$ dB/m. In Fig. 4(a) we first compare normalized diameters of the two fibers and observe that the core diameter of a rod-in-the-air fiber has to be significantly smaller than that of a porous fiber to achieve the same absorption loss. When comparing the effective modal diameters of the fundamental modes one notices that for a porous fiber the modal diameter is comparable to the size of a fiber core, while for a rod-in-the-air fiber the modal diameter is considerably larger than that of a fiber core. In other words, fundamental mode of a porous fiber is considerably less sensitive to the changes in the air cladding environment than the fundamental mode of a rod-in-the-air fiber. Superior field confinement by the porous fiber is also responsible for the higher effective refractive index of the fundamental mode of a porous fiber compared to that

fiber compared to that of a rod-in-the-air fiber (see Fig. 4.4(b)). Finally, we compare bending losses of the two fibers in Fig. 4(c). Using expression (4.3) we calculate and plot bending losses of the 3 layer porous fiber for the three different values of a fiber bending radius $R_b = [0.5,1.0,1.5]$ cm, as well as bending losses of a rod-in-the-air fiber for $R_b = [1.0,4.0,7.5]$ cm. We observe that for two fibers having the same absorption losses to also have similar bending losses, the bending radius of a rod-in-the-air fiber has to be significantly larger than a bending radius of a porous fiber. This makes us to conclude that resistance of a porous fiber to bending is superior to that of a rod-in-the-air fiber.

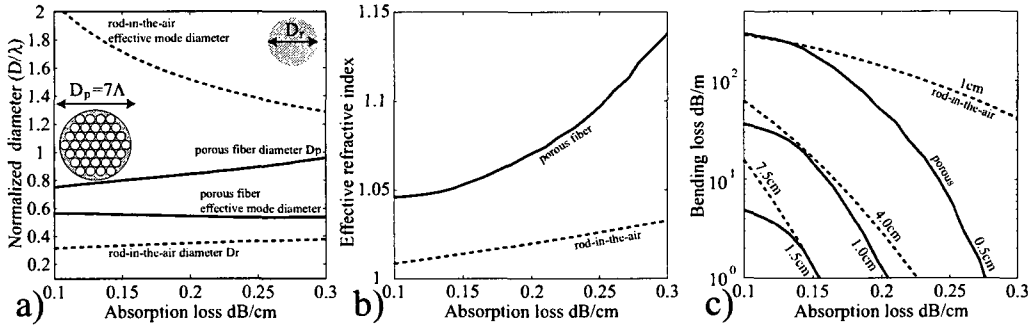

FIG. 4.4 – *Comparison of the propagation characteristics of the fundamental mode of a porous fiber (solid curves) with those of the fundamental mode of the equivalent rod-in-the-air subwavelength fiber (dashed curves). a) Normalized fiber and mode diameters. b) Modal effective refractive indices. c) Modal losses due to macro-bending.*

Finally, we comment on the overall size of a porous single mode fiber featuring N layers of holes. As follows from the schematic of Fig. 4.1(a), the diameter of a porous fiber is:

$$D_p = (2N+1)\,\Lambda = \lambda\,[(2N+1)\,(d/\lambda)\,/\,(d/\Lambda)] \approx \lambda\,(2N+1)\,(d/\lambda)\,. \qquad (4.5)$$

In (4.5) we have used the fact that in most designs the vein thickness is small $d/\Lambda \approx 1$. Particularly, in the case of $N = 3$ layers of holes and $d/\lambda \approx 0.1 - 0.2$ considered in this section we get $D_p \approx \lambda$; although the fiber diameter is not sub-wavelength, it is, however, comparable to the wavelength of operation. To simplify coupling to a THz beam of a

typical diameter of $5 - 10$ mm it is desirable to explore the possibility of designing single mode porous fiber with a diameter which is, at least, several times larger than the wavelength of operation. As follows from (4.5), one way of achieving this goal is by increasing the number of layers of holes in the fiber (see Fig. 4.5(a)), which also results in modes with larger effective areas. When increasing the fiber diameter, one has to be careful to ensure that the fiber remains single mode. Therefore, once the number of layers is increased, one typically has to make the material veins thinner. Unfortunately, our FEM software did not allow us to investigate fibers with more than $N = 5$ layers of holes. To demonstrate the possibility of large core-diameter porous fibers we resorted to design of porous Bragg fibers (see Fig. 4.5(b)) for which transfer matrix approach (Johnson et al., 2001) allows treatment of much larger systems. Particularly, in Fig. 5(b) we show schematic of a porous Bragg fiber consisting of 13 concentric material layers of thickness $h/\lambda = 0.01$ forming a periodic multilayer with a period Λ. Relative size of the air gap between individual layers is taken to be $(\Lambda - h)/\Lambda = 0.95$. With these parameters such a Bragg fiber is single mode with effective modal diameter of 5λ (mode diameter is comparable to the fiber core radius), and normalized absorption loss is 0.054. Energy flux distribution in the fundamental mode of such a fiber is shown in Fig. 4.5(b) exhibiting an overall Gaussian-like envelope with a small dip in the center. This demonstrates that, in principle, by increasing the number of periods in a fiber crossection, while reducing the thickness of material layers, one can design large area single mode porous fibers having most of the field confined in the fiber core and exhibiting greatly reduced absorption loss.

We conclude this section by presenting performance of a typical porous fiber as a function of the wavelength of operation. The fiber in question is designed for $\lambda = 300$ μm, has 4 layers of holes, and is characterized by $d/\lambda = 0.1$, $d/\Lambda = 0.88$. Fiber diameter is $D \simeq \lambda$. The material of the fiber is assumed to be Teflon polymer with bulk material loss $\alpha_{mat} = 130$ dB/m. In Fig. 4.5(a) we demonstrate absorption and bending losses of

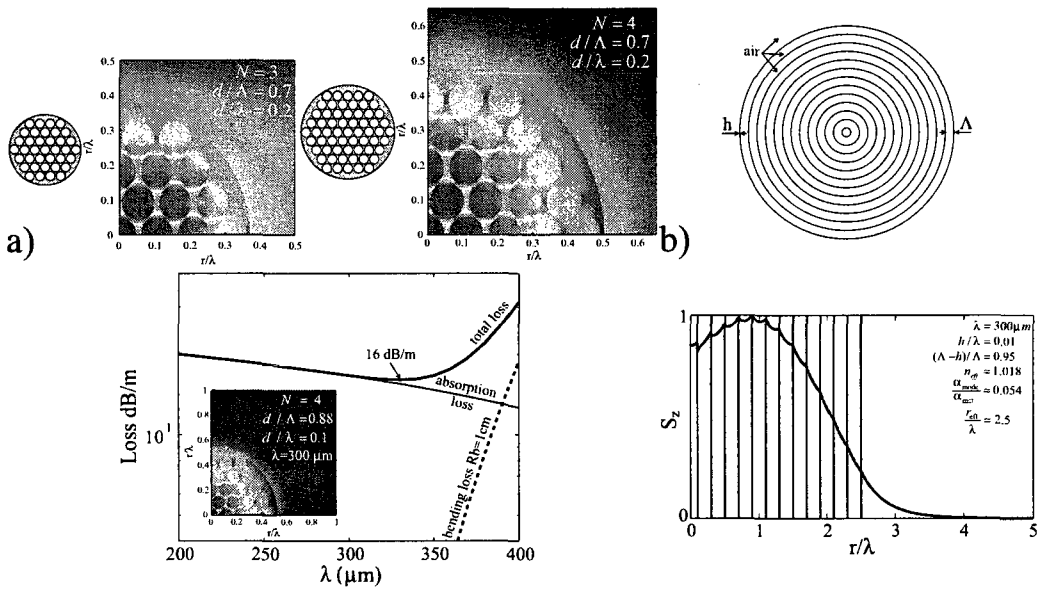

FIG. 4.5 – *Various implementations of porous fibers. a) Increasing the number of layers in a porous fiber leads to modes with larger effective mode diameters. In the lower plot a typical performance of a 4 layer porous fiber designed for* $\lambda = 300$ *μm is shown. b) Schematic of a 25 layer porous Bragg fiber and flux distribution in its fundamental mode.*

such a fiber assuming a very tight $R_b = 1$ cm bending radius. The fiber is effectively insensitive to bending as bending loss stays much smaller than the absorption loss even for very tight bending radii. We also see that performance of this fiber is broadband with total propagation loss less than 20 dB/cm across the whole $200 - 400$ μm wavelength region assuming the presence of bends as tight as $R_b = 1$ cm.

4.4 Porous photonic bandgap Bragg fibers with a network of bridges

In the remainder of the paper, we analyze guiding of THz radiation using porous photonic bandgap Bragg fiber. Schematic of such a fiber is shown in Fig. 4.1(b); Bragg fiber consists of a sequence of concentric material layers suspended in air by a network of material bridges in the shape of sub-wavelength rods. For the reference, porous Bragg

fiber geometry was recently discussed by Yu et al. (jin Yu et al., 2007), where instead of rods, thin material bridges were proposed, however, practical implementation of such a geometry may be challenging. Analysis of transmission properties of the air/silica based Bragg fibers with bridges for near IR applications was also presented recently in (Skorobogatiy et al., 2002).

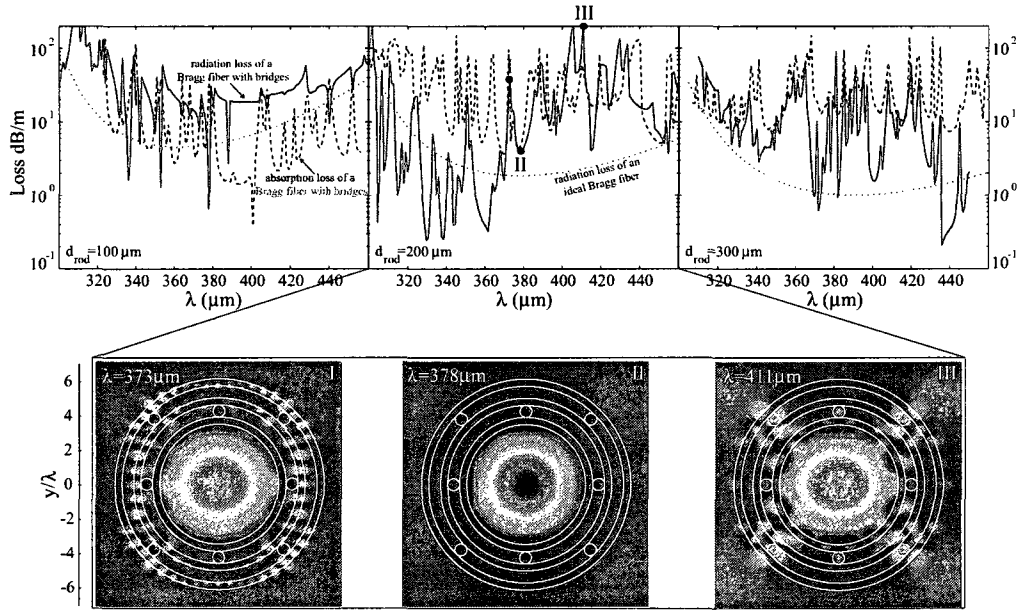

FIG. 4.6 – *Radiation losses (solid lines) and absorption losses (dashed lines) of the hollow core Bragg fibers for various bridge sizes* $d_{rod} = [100,200,300]$ *μm. For comparison, radiation loss of the equivalent Bragg fibers without rods are presented as dotted lines. Inset II shows* S_z *flux distribution in the fundamental core guided mode positioned at the minimum of the local bandgap at* $\lambda = 378$ *μm. Insets I and III show field distributions in the fundamental core mode at the wavelengths of coupling with different surface states.*

As detailed in Fig. 4.1(b), proposed fiber consists of a sequence of circular material layers of thickness h suspended in air by circular bridges (rods) of diameter d_{rod}. Thickness of the air layers is the same as the diameter of circular bridges. Since the bridges are small, the layers containing the bridges have an effective index close to that of air.

Thus, the alternating layers of polymer and air yield a high index-contrast Bragg fiber. Core radius R_c of a hollow Bragg fiber is assumed to be considerably larger than the wavelength of propagating light. Guidance in the hollow core is enabled by the photonic bandgap of a multilayer reflector. In the ideal Bragg fiber without bridges, for a design wavelength λ_c to coincide with the center of a photonic bangap of a multilayer reflector, thicknesses of the material and air layers have to be chosen to satisfy the following relation (Skorobogatiy and Kabashin, 2007):

$$d_{rod}\sqrt{n_{air}^2 - n_{eff}^2} + h\sqrt{n_{mat}^2 - n_{eff}^2} = \lambda_c/2. \tag{4.6}$$

Taking into account that in a large hollow core fiber the lowest loss core mode has effective refractive index n_{eff} slightly lower but very close to that of air n_{air}, we conclude that rod size does not affect considerably the resonance condition (4.6) and, therefore, can be chosen at will, while material layer thickness has to be chosen as $h = \lambda_c \Big/ \left(2\sqrt{n_{mat}^2 - n_{air}^2}\right)$. Note that this choice of material thickness is only an approximation, and therefore one should not expect exact matching of the wavelength of the center of a reflector bandgap with λ_c. In what follows we consider several designs of a 3 layer Bragg fiber with the following parameters $n_{mat} = 1.6$, $n_{air} = 1$, $d_{rod} = [100,200,300]$ μm. Design wavelength is $\lambda_c = 300$ μm, leading to the $h = 120$ μm choice of a material layer thickness. Fiber core radius is assumed to be $R_c = 1$ mm $\simeq 3.3\lambda_0$. Finally, fiber material loss is assumed to be comparable to that of a Teflon polymer $\alpha_{mat} = 130$ dB/m.

In Fig. 4.6 we present radiation losses (solid curves) and absorption losses (dashed curves) of the fundamental HE_{11} core guided mode of a Bragg fiber with bridges for various bridge sizes. For comparison, radiation losses of the fundamental core mode of equivalent Bragg fibers with identical parameters, however, without the dielectric bridges, are shown as dotted curves. Overall, radiation losses of the Bragg fibers with bridges follow radiation losses of the equivalent Bragg fibers without bridges. Howe-

ver, bandgaps of the Bragg fibers with bridges are fractured due to crossing of the core mode dispersion relation with those of the surface states. At the minima of the local bandgaps (see inset II in Fig. 4.6), field distribution of the fundamental core guided mode is Gaussian-like and it is well confined inside of the hollow core. For example, for $d_{rod} = 200$ μm at $\lambda = 378$ μm the total waveguide loss is ~ 8.7 dB/m and the bandwidth is ~ 10 μm. In principal, by adding only few more layers into Bragg reflector (5-7 material layers instead of 3 material layers shown in Fig. 4.1(b)), radiation loss can be reduced below absorption loss resulting in fibers of ~ 5 dB/m total loss in the case of $d_{rod} = 200$ μm, and fibers of ~ 1 dB/m total loss in the case of $d_{rod} = 100$ μm. At the wavelengths of crossing with surface states (see insets I and III in Fig. 4.6), radiation and absorption losses increase considerably due to excitation of the highly lossy surface states localized inside of the material layers of a Bragg reflector. As seen from the insets I and II in Fig. 6, fields of the surface states are concentrated in the vicinity, or directly, at the material bridges separating separating concentric layers of a Bragg reflector. By comparing the loss data in Fig. 6 for various fiber designs one concludes that when bridge size increases, the number of surface states also increases. Therefore, to improve fiber bandwidth one has to avoid fracturing of the reflector bandgap with surface states, which is, in principle possible, by reducing the thickness of the bridges. of the bridges. However, even in the best case scenario of ideal Bragg fibers without any bridges, bandwidth of a plastic-based fiber with $n_{mat} \sim 1.6$ is relatively small and on the order of ~ 100 μm ~ 0.3 THz.

Finally, to evaluate resistance of the porous Bragg fibers to bending, we present macro-bending loss analysis for the case of porous Bragg fibers without bridges. We use perturbation matched coupled-mode theory described in (Skorobogatiy et al., 2002) to solve mode scattering problem due to bending, assuming that at the bend input a single HE_{11} mode is excited. Simulated bending losses are presented in Fig. 4.7 for the two orthogonal modal polarizations (parallel and perpendicular to the plane of the bend). Note that

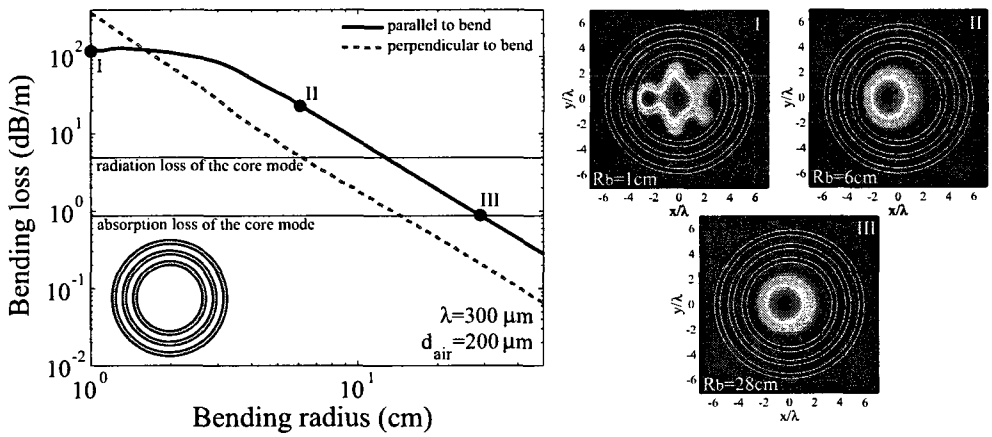

FIG. 4.7 – *Bending losses of a porous Bragg fiber without bridges designed and operated at* $\lambda_c = 300$ *μm. Bending loss is strongly sensitive to the polarization of an* HE_{11} *mode, with the polarization in the plane of a bend being the lossiest. In the insets we show* S_z *flux distributions at the output of the* 90^0 *bends of various radii.*

bending loss is strongly polarization dependent, with the polarization in the plane of a bend being the lossiest. We also note that for the bending loss of the lossiest polarization to be lower than the straight fiber radiation loss one has to insure bending radii of no tighter than 12 cm. Fig. 7 we show field distributions at the output of the 90^0 bends of various radii. For tight bending radii $R_b < 6$ cm we observe that not only bending loss becomes appreciable, but also the quality of the output beam deteriorates as judged by the non-Gaussian distribution of the beam fields.

We conclude this section by mentioning in passing that we have attempted fabrication of porous Bragg fibers experimentally. Inset in Fig. 4.1(b) presents optical microscope image showing a small part of the cross-section of a porous multilayer. The fiber was made by co-rolling of a solid PMMA film with a second PMMA film that had windows cut into it. Once rolled, the windows formed the air gaps and the remaining bridges of the cut film formed bridges separating the solid film layers. Preliminary bolometer measurements of THz transmission through porous Bragg fibers having 1 cm hollow core diameter resulted in total loss estimate of $\sim$ 40 dB/m. We are currently pursuing

more detailed transmission measurements of these fibers.

4.5 Conclusions

We have proposed two types of porous plastic fibers for low-loss guidance of THz radiation. Firstly, a microstructured polymer THz fiber composed of a polymer rod containing hexagonal array of sub-wavelength air holes was discussed. Let us emphasize that a periodic array of holes is not necessary as the guiding mechanism remains total internal reflection, and not the photonic bandgap effect. Although in this design the fiber core diameter is comparable to that of the wavelength of operation, nevertheless, the major portion of THz power launched into the fiber is confined within the air holes inside of the fiber core. As a result, coupling to the cladding environment is greatly reduced, while the modal absorption loss lower than 10 dB/m can be achieved with 130 dB/m bulk absorption loss of a fiber material. Using approximate analytical expression to calculate macro-bending losses, allowed us to conclude that suggested porous fibers are highly resistant to bending, with bending loss being smaller than modal absorption loss for bends as tight as 3 cm of radius. Finally, suggested porous fibers are broadband having $\sim$ 1 THz bandwidth even in the presence of tight bends. Secondly, we have considered porous photonic bandgap Bragg fibers made of a set of concentric material layers suspended in air by the network of circular bridges. Fiber hollow core diameter is much larger that the operating wavelength, thus allowing efficient coupling to various THz sources. Although total modal loss (absorption plus radiation loss) lower than 5 dB/m can be achieved with 130 dB/m bulk absorption loss of a fiber material, fiber bandwidth was found to be smaller than 0.1 THz. Parasitic coupling to the surface states of a multilayer reflector facilitated by the material bridges was determined as primary mechanism responsible for the reduction of the bandwidth of a porous photonic bandgap Bragg fiber.

CHAPITRE 5

ARTICLE 4: SURFACE-PLASMON-RESONANCE-LIKE FIBER-BASED SENSOR AT TERAHERTZ FREQUENCIES

Alireza Hassani, Alexandre Dupuis, and Maksim Skorobogatiy[1].

This chapter proposing ferroelectric PVDF naturally supports SPR at THz including previous chapter proposing the low loss porous fiber designs present materials which are necessary to complete the puzzle of the design of MOF based plasmonic-like sensors at THz. To illustrate PVDF support SPR naturally, THz plasmon-like excitation on top of a thin ferroelectric PVDF layer, covering solid-core polymeric Bragg fiber and facing a liquid analyte, is demonstrated theoretically. We discuss the fact that the refractive index behavior of the ferroelectric PVDF layer demonstrates a new type of plasmonic-like excitation in THz regime which was impossible when using metal layers at the THz. PVDF can be electrically poled to convert to a ferroelectric semi-crystalline polymer. The real part of the ferroelectric PVDF dielectric constant is negative, and by analogy with the behavior of metals in the visible range, PVDF layer is expected to support a plasmon-like excitation. Moreover, PVDF gives an opportunity to design a fully polymeric structure for THz plasmonic devices. Furthermore, we demonstrate that instead of designing complex artificial metamaterials for surface plasmon excitation at THz, a THz plasmonic-like refractometry sensor can be design similar to ones exist at visible-IR range. For example, here, the structure of the proposed solid Bragg fiber based plasmonic-like refractometry sensor for the THz range is somehow similar to ones we proposed for visible and IR. Finally, we show the possibility of designing a refractometry sensor in the THz regime with the resolution of $2 \cdot 10^{-4}$ RIU for the analyte index of $n_a = 1.33$.

1. Department Engineeing Physics, École Polytechnique de Montréal, Montréal Canada

5.1 Abstract

THz plasmon-like excitation on top of a thin ferroelectric polyvinylidene fluoride (PVDF) layer covering solid-core polymeric Bragg fiber and facing liquid analyte is demonstrated theoretically. In a view of designing a fiber-based sensor of analyte refractive index, phase matching of a THz plasmon-like mode with the fundamental core guided mode of a fiber is then demonstrated for the most challenging case of low refractive index analytes. Novel sensing methodology based on the core mode anomalous dispersion is proposed. Similarly to the Surface Plasmon Resonance sensors in the visible, we show the possibility of designing high sensitivity sensors in the THz regime with a resolution of $2 \cdot 10^{-4}$ in refractive index change.

5.2 Introduction

In the visible and ultraviolet range, the collective oscillation of free charge carriers at a metal-dielectric interface yields a surface plasmon wave propagating along the surface of the metal (Agranovich and Mills, 1982; Homola, 1995; Hassani and Skorobogatiy, 2007a; Skorobogatiy and Kabashin, 2006a; Gauvreau et al., 2007). The sensitivity of plasmon excitation to changes in the refractive index of the dielectric medium has been widely exploited for sensing applications. The plasma frequency, which imposes a lower frequency limit for the existence of these plasmons, is defined by $\omega_p^2 = ne^2/\varepsilon_0 m_e$, where n,e,ε_0,m_e are the electron density, electric charge, vacuum permittivity and electron mass. Since the free electron density in metals is typically in the range of 10^{22}cm^{-3}, the plasma frequency is frequently limited to the visible and ultraviolet regions. At frequencies significantly below the plasma frequency (like the THz range), large negative permittivity strongly prohibits electromagnetic fields from penetration inside a metal, and plasmon excitation on the metal/dielectric interface becomes challenging. Therefore,

efficient plasmonic excitation at lower frequencies requires materials with lower plasma frequencies (Wu et al., 2003; Qiu, 2005; O'Hara et al., 2005; Wang and Mittleman, 2006; Chen et al., 2006; Rivas et al., 2006; Lee et al., 2006; Maier et al., 2006; Miyamaru et al., 2007; Pendry et al., 1996; Pendry et al., 1998). Recently, Pendry et al. have suggested an artificial material in the form of a 2D subwavelength metallic wire lattice for which the effective plasma frequency is designable and equals $\omega_p^2 = 2\pi c^2/a^2 \ln(a/r)$ (Pendry et al., 1996; Pendry et al., 1998). Since this plasmon frequency relies on the wire radius, r, and the lattice constant, a, the geometrical parameters of the artificial structure can tune the electron plasma frequency of metal to the THz or sub-THz frequency range. Moreover, further studies have recently confirmed that artificial subwavelength-sized metal structures can tune the plasma frequency of metals to GHz or THz frequency range and allow metals to support plasmon-like surface waves at frequencies much lower than the visible range (Wu et al., 2003; Qiu, 2005; Chen et al., 2006; Maier et al., 2006).

Alternatively, some materials can naturally support plasmon-like excitations in the THz regime due to resonances in their dielectric constant. Particularly, polyvinylidene fluoride (PVDF) is a ferroelectric semi-crystalline polymer with a small absolute value of permittivity in the visible and near-IR regions. However, in the THz region the dielectric function of ferroelectric PVDF exhibits a resonance:

$$\varepsilon_{PVDF}(\omega) = \varepsilon_{opt} + \frac{(\varepsilon_{dc} - \varepsilon_{opt})\omega_{TO}^2}{\omega_{TO}^2 - \omega^2 + i\gamma\omega}, \tag{5.1}$$

where, according to Ref. 17 $\varepsilon_{opt} = 2.0$, $\varepsilon_{dc} = 50.0$, $\omega_{TO} = 0.3\,THz$, and $\gamma = 0.1\ THz$. Fig. 5.1 shows the real and imaginary parts of the refractive index of ferroelectric PVDF in the wavelength range between 100 μm (3 THz) and 700 μm (0.43 THz). The real part of the refractive index of PVDF in this region is less than one, while the imaginary part is positive and mostly larger than one. Therefore, the real part of the PVDF dielectric constant is negative and by analogy with the behavior of the metals in the visible range, PVDF layer is expected to support a plasmon-like excitation. Furthermore, PVDF

gives an opportunity to design a fully polymeric structure for THz plasmonic devices using such established mass production techniques as micro-embossing and fiber drawing, which potentially makes the fabrication process highly suitable for the industrial scale-up.

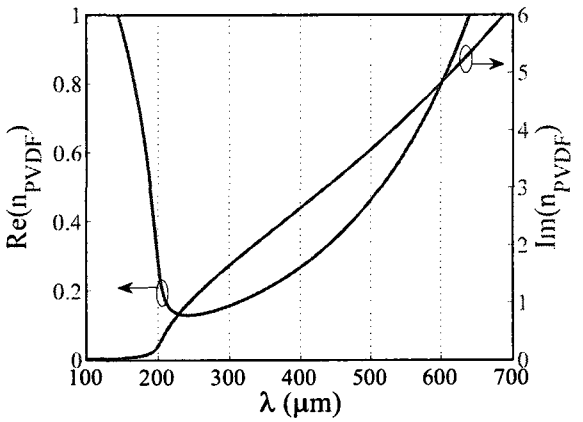

FIG. 5.1 – *The real and imaginary part of the refractive index of ferroelectric PVDF.*

This paper pursues two goals. First is to show that layers of ferroelectric PVDF can support THz plasmon-like excitations similar to the ones found in metals in the visible range. Second is to show that similarly to the design of SPR sensors in the visible, we can design integrated fiber-based sensors in THz regime, which are highly sensitive to the changes in the refractive index of analyte. Practical implementation of the THz SPR-like sensor discussed in this work is a solid-core Bragg fiber with a PVDF layer on top facing low refractive index analyte.

5.3 THz plasmon-like excitations

We first would like to remind the reader general ideas behind the principles of operation of a fiber-based SPR sensor. A typical configuration of such a sensor is a fiber with a thin metal layer deposited on its surface in the near proximity of a fiber core. Another side

of a metal layer is facing the analyte to be monitored. During operation of a sensor, one launches a broadband light into the fiber core. In the vicinity of a specific wavelength defined by the sensor design, one of the core modes is phase matched (avoiding crossing of the corresponding dispersion relations) with a plasmon excitation mode confined to the metal/analyte interface. In the vicinity of such a resonant wavelength one observes dramatic decrease in the power transmitted through the fiber due to partial energy transfer from the core guided mode into a lossy plasmon. As dispersion relation of a plasmon mode is very sensitive to the refractive index of an analyte, resonant wavelength, and, hence, spectral position of the absorption peak will shift when analyte refractive index is changed. By detecting spectral shift in the absorption peak of a core guided mode, changes in the analyte refractive index on the order of $10^{-4} - 10^{-5}$ RIU (Refractive Index Units) can be detected.

Additionally, as detailed in Refs.(Skorobogatiy and Kabashin, 2006b) and (Gauvreau et al., 2007), using photonic bandgap fibers considerably simplifies phase matching of the plasmon and core guided fiber modes, especially in the case of low refractive index analytes. Particularly, effective refractive index of a plasmon excitation is typically close to that of an analyte, while effective refractive index of a core guided fiber mode is close to that of a core material. As there are few optical materials that have refractive indices smaller than 1.45, in practice, it becomes challenging to achieve phase matching between the plasmon and core guided modes when analyte refractive index is smaller than 1.4 (the case of gaseous and aqueous analytes). A key advantage of using the photonic bandgap fibers is that the fundamental core guided mode in such fibers can be designed to have an arbitrarily small effective refractive index. Particularly, by placing the reflector bandgap at the desired wavelength of operation, and by adjusting the fiber core size one can design a fundamental core mode to have arbitrarily small effective refractive index, and to achieve phase matching with a plasmon mode at any desired operational wavelength and for any analyte. In this paper, we demonstrate the possibility of THz plasmonic-like ex-

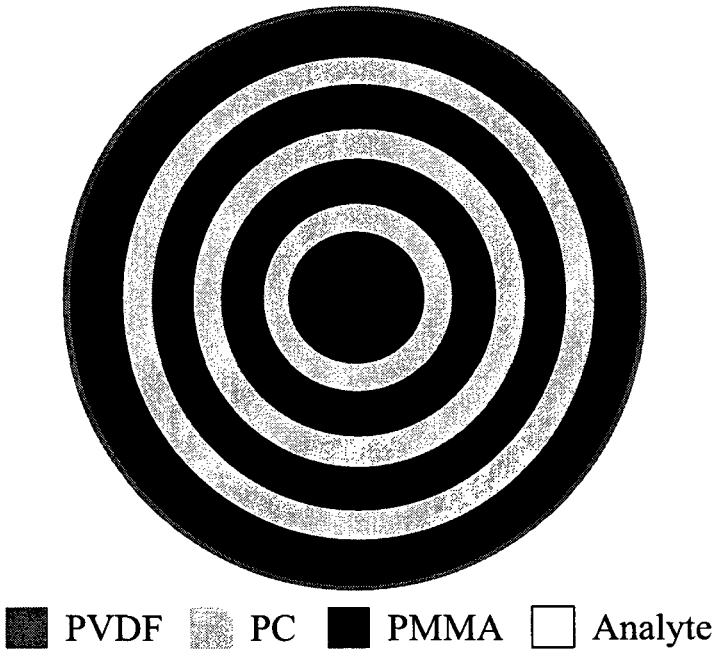

FIG. 5.2 – *Schematic of a solid-core THz Bragg fiber with PVDF layer facing analyte.*

citation on top of a PVDF layer facing a low refractive index liquid analyte with n=1.33. A plasmon-like mode is excited by the fundamental mode of a solid core Bragg fiber at the frequency of phase matching between the two modes. The Bragg fiber detailed here is assumed to have a solid core made of polymethyl methacrylate (PMMA) (refractive index $n_{PMMA} = 1.59$ at 1 THz), and surrounded with three bi-layers of polycarbonate (PC) (refractive index $n_{PC} = 1.65$ at 1 THz) and PMMA, thus forming a Bragg reflector (Jin et al., 2006). The core radius is $R_c = 300\mu$m, the thicknesses of the PC and PMMA layers are 130 μm, and 205 μm, respectively. A 10 μm thick ferroelectric PVDF layer is placed on top of the Bragg reflector. Fig. 5.2 (a) presents a schematic of the proposed solid-core THz Bragg fiber. The PMMA/PC thicknesses were chosen so that the center wavelength of the Bragg reflector bandgap is near 280 μm ($\sim$1 THz).

When operating within the bandgap of a Bragg fiber reflector, the fields of a fundamental Gaussian-like HE_{11} leaky core mode decay exponentially fast into the periodic reflector.

Therefore, modal field intensity in the PVDF layer also decreases exponentially fast with the number of layers in the reflector. Therefore, the total number of bi-layers must remain small in order for the light to be able to couple to a plasmon. It is important to note that in this first study, the material absorption was considered only in the PVDF layer. As we will see further, this choice is justified as loss incurred due to coupling to a plasmon excitation, generally, is much higher than the loss due to absorption of the fiber materials. Therefore, to simplify interpretation of the results we set fiber material losses to zero.

We used a finite-element method with perfectly matched layer boundaries and a four fold symmetry (Jin, 2002) in order to find the complex propagation constants of the core-guided and plasmonic modes by solving the vectorial Maxwell equations. In a particular case of fibers exhibiting circular symmetry, the results produced by the finite element method can be also confirmed by a transfer matrix method. Since we have neglected material absorption, the imaginary part of the core mode propagation constant defines modal propagation loss resulting from coupling to a lossy plasmon. For a given analyte, we design a Bragg fiber reflector in such a manner as to ensure that the effective refractive index of a plasmonic excitation (which is close to that of analyte) falls within the fiber band gap. We then vary the fiber core size to position core guided mode dispersion curve in such a way as to phase match it with a plasmon mode. Sensing in analytes of significantly different refractive indices requires distinct fiber designs. In all the simulations that follow we arbitrarily assume a low refractive index analyte with refractive index of n=1.33. Nevertheless, design considerations presented in this paper are general and can be adapted to any analyte refractive index.

Fig. 5.3 shows the dispersion relation of the fundamental core mode (blue curve), and the plasmonic mode (red curve). The solid and dotted blue curves present the dispersion relations of the fundamental core mode for the two values of the analyte refractive index of 1.33 and 1.335, respectively. Furthermore, Fig. 5.4 shows the field distributions in various fiber modes and at several points of interest indicated in Fig. 5.3. Particu-

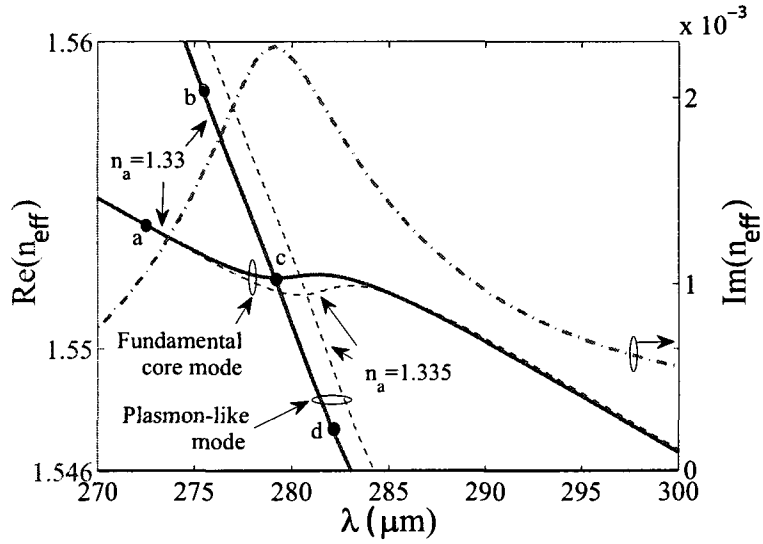

FIG. 5.3 – *Dispersion relations of the core-guided mode (solid and dotted blue curves) and the surface plasmon mode (solid and dotted red curves) in the vicinity of the phase-matching point C. Solid curves are calculated for the analyte refractive index* $n_a = 1.33$, *while dotted curves are calculated for* $n_a = 1.335$. *Transmission loss of a core-guided mode (dashed black curve) exhibits strong increase at the phase matching point C due to efficient mixing with a plasmon wave.*

lalry, Fig. 5.4 (a) shows the field distribution in the fiber core mode at the point A in Fig. 5.3, which is located far from the point of phase matching with a plasmon (point C in Fig. 5.3). There, the mode is well confined to the fiber core with only a little intensity in the PVDF layer region. In Fig. 5.4 (b) we show the field distribution in the plasmonic mode at the point B in Fig. 5.3, which is located far from the phase matching point with the fiber core mode. As expected, most of the modal intensity is concentrated at the PVDF/analyte interface. When the refractive index of analyte increases from $n_a = 1.33$ to $n_a = 1.335$, the plasmonic mode shifts toward longer wavelengths (red dotted curve). In Fig. 5.4 (c) we show the field distribution in the core mode at the point C in Fig. 5.3, which is located exactly at the phase matching point with a plasmon mode. At point C strong mixing between the two modes is observed. Also note that the curvature of the core mode dispersion relation changes in the vicinity of the phase matching point C. Ori-

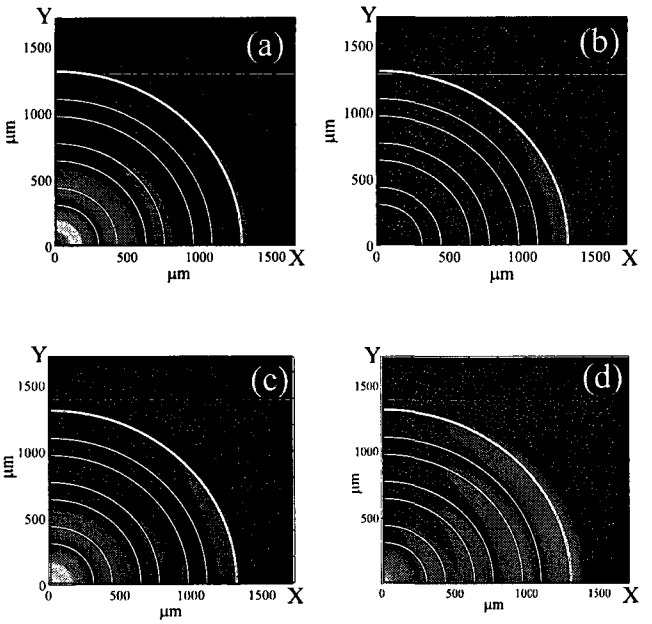

FIG. 5.4 – *S_z field distributions in the fiber modes at various points indicated in Fig. 5.3. a) Fundamental core mode far from the phase matching point. b) Plasmonic mode far and to the left from the phase matching point. c) Fundamental core mode at the phase matching point. d) Plasmonic mode far and to the right from the phase matching point. This mode is located very close to the edge of a reflector bandgap resulting in a strong penetration of a plasmon mode fields into the fiber core.*

ginally, we believed that this change is due to interaction of a core guided mode with yet another fiber mode. After performing exhaustive simulations with transfer matrix and finite element codes we are convinced that there is no other mode located in this region. Therefore, we have to conclude that observed anomaly in the dispersion relation of a core guided mode is due to unusually strong and extended interaction of such a mode with a plasmonic mode. Particularly, when plotting the field distribution in the plasmon mode at the point D, which is located far to the right from the phase matching point, we still observe a very strong mixing between the core guided and plasmonic modes. By studying positions of bandgap edges we find that this behavior of a plasmonic mode is due to the fact that its dispersion relation to the right of a phase matching point C ap-

proaches very quickly the edge of a reflector bandgap. In this case, modal penetration of a plasmon mode through the reflector and into the fiber core becomes strongly pronounced. This, in turn, leads to a strong interaction between the plasmon and core guided modes even far from the phase matching point, and as a consequence, an anomaly in the core mode dispersion relation.

Finally, the black dotted curve in Fig. 5.3 shows the imaginary part of the effective refractive index of the fundamental core mode, which also defines modal propagation loss due to absorption by the plasmon. In the units of dB/cm such a loss is expressed as:

$$\alpha\,[dB/cm] = \mathrm{Im}\,(n_{eff}) \cdot 40\pi/\,(\lambda\,[cm] \cdot \log 10) = 1819\,[dB/cm] \cdot \mathrm{Im}\,(n_{eff}) \cdot \nu\,[THz]\,. \tag{5.2}$$

For example, at 1 THz, $\mathrm{Im}\,(n_{eff}) \sim 10^{-3}$ defines a $\sim$1.8 dB/cm propagation loss of a fiber mode. Note that in this paper material absorption of the fiber materials have been neglected with an exception of a PVDF layer. In practice, total modal propagation loss will be approximately given by the sum of the bulk loss of a core material and the loss due to coupling to a plasmon excitation.

Fig. 5.5 shows anomalous dispersion of the fundamental core mode of a Bragg fiber near the phase matching point with a plasmon mode. Due to strong interaction of the fundamental core mode with a plasmon mode, dispersion of a core mode is highly sensitive to the changes in the refractive index of analyte. For example, assuming analyte refractive index of 1.33, the core mode dispersion achieves its maximum positive value of 60 ps/nm-km at 282 μm (blue curve in Fig. 5.5). When changing refractive index of analyte by $5 \cdot 10^{-3}$ RIU, the core mode dispersion curve shifts towards longer wavelengths resulting in a new value of modal dispersion of -55 ps/nm-km at 282 μm (red curve in Fig. 5.5). Such a dramatic sensitivity of modal dispersion to changes in the refractive index of analyte can be, in principle, used for sensing through detection of changes in the pulse propagation.

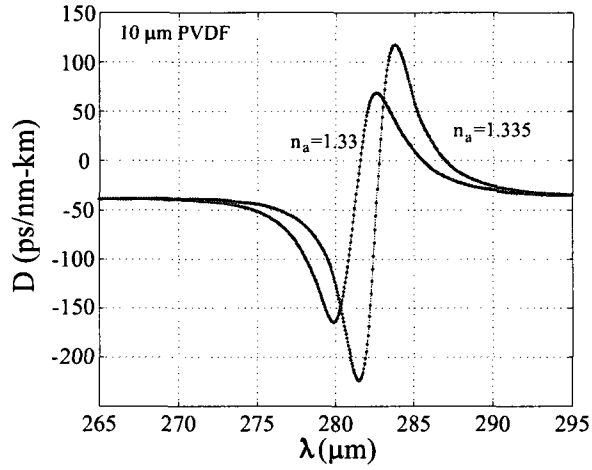

FIG. 5.5 – *Dispersion of the fundamental core mode near the phase matching point with a plasmon mode for the two values of the analyte refractive index* $n_a = 1.33$ *(blue curve) and* $n_a = 1.335$ *(red curve)*

5.4 Sensitivity of a THz SPR-like sensor

Finally, we address the question of sensitivity of a proposed SPR-like sensor to the changes in the refractive index of analyte. One mode of operation of a proposed sensor is by registering at a fixed frequency the changes in the amplitude of a transmitted light. We define $\alpha(\lambda,n_a)$ to be the transmission loss of the fiber core mode as a function of the wavelength and the refractive index of analyte n_a. Considering P_0 to be the power launched into the fiber core mode, the power detected after propagation along the sensor of length L will be $P(L,\lambda,n_a) = P_0 \exp(-\alpha(\lambda,n_a)L)$. For the operational wavelength λ, the amplitude sensitivity to the dn_a change in the analyte refractive index can then be defined as:

$$S_A(\lambda)[RIU^{-1}] = \frac{1}{P(L,\lambda,n_a)} \frac{P(L,\lambda,n_a + dn_a) - P(L,\lambda,n_a)}{dn_a}. \tag{5.3}$$

The sensor length L is typically limited by the modal transmission loss. A reasonable choice of a sensor length is $L = 1/\alpha(\lambda,n_a)$; such a choice of sensor length results in a simple definition of sensitivity with respect to small changes in the analyte refractive index:

$$S_A(\lambda)[RIU^{-1}] = \frac{1}{P(L,\lambda,n_a)}\frac{\partial P(L,\lambda,n_a)}{\partial n_a} = -\frac{1}{\alpha(\lambda,n_a)}\frac{\partial \alpha(\lambda,n_a)}{\partial n_a}. \tag{5.4}$$

In Fig. 5.6 we present amplitude sensitivity of a solid-core Bragg fiber sensor presented earlier. The maximal sensitivity is achieved at 285μm and equals to 50 RIU^{-1}. Assuming that 1 change in the transmitted intensity can be detected reliably, this leads to the sensor resolution of $2 \cdot 10^{-4}$ RIU. The solid and dotted black curves in Fig. 5.6 show losses of a core guide mode for the two values of the analyte refractive indices. Finally, based on the value of modal losses the sensor length is in a 1 cm range.

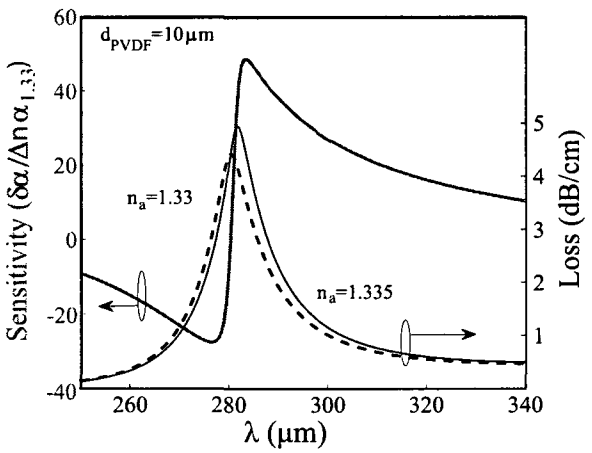

FIG. 5.6 – *Sensitivity of a solid-core Bragg fiber-based sensor incorporating a thin ferroelectric PVDF layer (blue line). Loss of a fundamental core mode of a fiber in the vicinity of a phase matching point with a plasmonic mode for the two values of analyte refractive index* $n_a = 1.33$ *(dotted curve) and* $n_a = 1.335$ *(solid curve).*

5.5 Conclusion

In conclusion, the THz plasmon-like excitation on a thin PVDF film via phase matching with a fundamental core mode of a solid-core Bragg fiber is demonstrated. Anomalous dispersion of a core guided mode due to strong interaction with a plasmonic mode near the band edge of a fiber bandgap is demonstrated. Novel methodology of sensing changes in the refractive index of analyte via detection of changes in propagation of short pulses is suggested. Finally, amplitude-based sensor resolution as low as $2 \cdot 10^{-4}$ RIU is demonstrated in THz regime, with sensor length in a 1 cm range.

CHAPITRE 6

ARTICLE 5: SURFACE PLASMON RESONANCE-LIKE INTEGRATED SENSOR AT TERAHERTZ FREQUENCIES FOR GASEOUS ANALYTES.

Alireza Hassani and Maksim Skorobogatiy[1].

In this chapter, using the proposed solution for low loss THz waveguide in chapter 4 and plasmonic-like excitation in chapter 5 we design a waveguide based plasmonic-like refractometry sensor at THz for gaseous analytes. In this sensor, plasmonic excitation occurs on top of a $\sim$ 30 μm ferroelectric PVDF layer wrapped around a subwavelength porous polymer fiber. The subwavelength porous fiber provides a low loss guiding mechanism as well as considerable tunability for the core modal effective index enabling the phase matching between the core mode and surface plasmons bordering a gaseous analyte at $\sim 300 \mu m$. To our knowledge it is the first waveguide based plasmonic-like sensores design for gaseous analytes in THz regime. We are interested in SPR sensors operating at THz because The longer the operating wavelength of the SPR sensors is, the longer the probe depth of SPR sensor is, resulting in bigger sized particles can be detected by SPR sensors. Here, in direct analogy to SPR sensing in the visible, plasmon-like resonances at THz provides the probe depth of $\sim$ 60 μm which is much longer than that $0.1-0.3$ μm probe depth of SPRs at visible. This enables study of the micron-sized particle binding dynamics within $10-60 \mu m$ of the sensor surface, which is the particular interest for the label-free detection of specific bacteria by functionalizing the sensor surface with bacteria specific phages. Finally, the amplitude and spectral based refractometry sensitivity of $3.4 \cdot 10^{-4}$ RIU, and $1.3 \cdot 10^{-4}$ RIU are predicted for this sensors

.

1. Department Engineeing Physics, École Polytechnique de Montréal, Montréal Canada

6.1 Abstract

Plasmon-like excitation at the interface between fully polymeric fiber sensor and gaseous analyte is demonstrated theoretically in terahertz regime. Such plasmonic excitation occurs on top of a $\sim 30\mu$m ferroelectric PVDF layer wrapped around a subwavelength porous polymer fiber. In a view of designing a fiber-based sensor of analyte refractive index, phase matching of a plasmon-like mode with the fundamental core guided mode of a low loss porous fiber is then demonstrated for the challenging case of a gaseous analyte. We then demonstrate the possibility of designing high sensitivity sensors with amplitude resolution of $3.4 \cdot 10^{-4}$ RIU, and spectral resolution of $1.3 \cdot 10^{-4}$ RIU in THz regime. Finally, novel sensing methodology based on detection of changes in the core mode dispersion is proposed.

6.2 Introduction

In the visible and ultraviolet range, the collective oscillation of free charge carriers at a metal-dielectric interface yields a surface plasmon wave propagating along the surface of the metal (Agranovich and Mills, 1982; Homola, 1995; Hassani and Skorobogatiy, 2007a; Skorobogatiy and Kabashin, 2006a; Gauvreau et al., 2007). Propagating at the metal/dielectric interface, surface plasmons are extremely sensitive to changes in the refractive index of the dielectric. This feature constitutes the core of many Surface Plasmon Resonance (SPR) sensors. Typically, in the visible range, these sensors are implemented in the Kretschmann-Raether prism geometry where p-polarized light is launched through a glass prism and reflected from a thin metal (Au, Ag) film deposited on the prism facet. The presence of a prism allows phase matching of an incident electromagnetic wave with a plasmonic wave at the metal/ambient dielectric interface at a specific combination of the angle of incidence and wavelength. Mathematically, phase matching condition is ex-

pressed as equality between the plasmon wave-vector and a projection of the wavevector of an incident wave along the interface (Agranovich and Mills, 1982).

The sensitivity of plasmon excitation to changes in the refractive index of the dielectric medium has been widely exploited for sensing applications. The plasma frequency, which imposes a lower frequency limit for the existence of these plasmons, is defined by $\omega_p^2 = ne^2/\varepsilon_0 m_e$, where n,e,ε_0,m_e are the electron density, electric charge, vacuum permittivity and electron mass. Since the free electron density in metals is typically in the range of 10^{22} cm^{-1}, the plasma frequency is frequently limited to the visible and ultraviolet regions. At frequencies significantly below the plasma frequency (like the THz range), large negative permittivity strongly prohibits electromagnetic fields from penetration inside a metal, and plasmon excitation on the metal/dielectric interface becomes challenging. Therefore, efficient plasmonic excitation at lower frequencies requires materials with lower plasma frequencies (Wu et al., 2003; Qiu, 2005; O'Hara et al., 2005; Wang and Mittleman, 2006; Chen et al., 2006; Rivas et al., 2006; Lee et al., 2006; Maier et al., 2006; Miyamaru et al., 2007; Pendry et al., 1996; Pendry et al., 1998). Pendry et al. have suggested an artificial material in the form of a 2D subwavelength metallic wire lattice for which the effective plasma frequency is designable and equals $\omega_p^2 = 2\pi c^2/a^2 \ln(a/r)$ (Pendry et al., 1996; Pendry et al., 1998). Since this plasmon frequency relies on the wire radius, r, and the lattice constant, a, the geometrical parameters of the artificial structure can tune the electron plasma frequency of metal to the THz or sub-THz frequency range. Moreover, further studies have recently confirmed that artificial subwavelength-sized metal structures can tune the plasma frequency of metals to GHz or THz frequency range and allow metals to support plasmon-like surface waves at frequencies much lower than the visible range (Wu et al., 2003; Qiu, 2005; Chen et al., 2006; Maier et al., 2006).

Thanks to the refractive index behavior of the ferroelectric Polyvinylidene fluoride (PVDF) layer we demonstrate new type of plasmonic-like excitations in THz regime which was

impossible before while using metal layers in THz regime. PVDF is a ferroelectric semi-crystalline polymer with a small absolute value of permittivity in the visible and near-IR regions. However, in the THz region the dielectric function of ferroelectric PVDF exhibits a resonance:

$$\varepsilon_{PVDF}(\omega) = \varepsilon_{opt} + \frac{(\varepsilon_{dc} - \varepsilon_{opt})\omega_{TO}^2}{\omega_{TO}^2 - \omega^2 + i\gamma\omega}, \tag{6.1}$$

where, according to (Hidaka et al., 2005) $\varepsilon_{opt} = 2.0$, $\varepsilon_{dc} = 50.0$, $\omega_{TO} = 0.3THz$, and $\gamma = 0.1\ THz$. Fig. 6.1 shows the real and imaginary parts of the refractive index of ferroelectric PVDF in the wavelength range between 100 μm (3 THz) and 700 μm (0.43 THz). The real part of the refractive index of PVDF in this region is less than one, while the imaginary part is positive and mostly larger than one. Therefore, the real part of the PVDF dielectric constant is negative and by analogy with the behavior of the metals in the visible range, PVDF layer is expected to support a plasmon-like excitation. Moreover, PVDF gives an opportunity to design a fully polymeric structure for THz plasmonic devices using such established mass production techniques as micro-embossing and fiber drawing, which potentially makes the fabrication process highly suitable for the industrial scale-up.

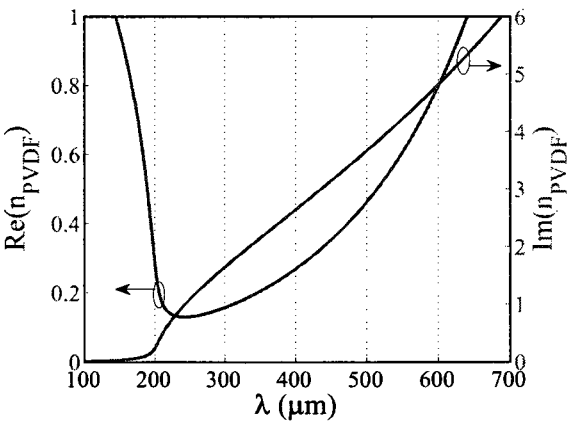

FIG. 6.1 – *The real and imaginary parts of the refractive index of ferroelectric PVDF.*

This paper pursues two goals. The first goal is to show that thin layers of ferroelectric

PVDF in air can support THz plasmon-like excitations similar to the ones found at the metal/dielectric interfaces in the visible range. The second goal is to design a fully polymeric integrated fiber-based sensor in THz regime capable of detecting the index change in gaseous analytes (the most challenging case).

In direct analogy to SPR sensing in the visible, existence of plasmon-like resonances in THZ can enable study of the micron-sized particle binding dynamics within 10-60 μm of the sensor surface. This can be of particular interest for the label-free detection of specific bacteria by fictionalizing the sensor surface with bacteria specific phages. In comparison, SPR sensors in the visible can only detect binding of nano-molecules with sizes less than 100nm (size of a plasmon tail), rendering the method insensitive to the larger particles, such as bacteria.

It is worth mentioning that SPR sensing mechanism is completely different in spirit from spectroscopy based sensing. Particularly, plasmon-based sensors are mostly sensitive to changes in the real part of the refractive index in a thin sensing layer in the near vicinity of a metal surface. Specificity of a SPR sensor is achieved by coating a metal layer with a thin sensing layer that changes its refractive index when exposed to the target analyte. In contrast, spectroscopy based methods use detection of absorption lines in the spectrum of a target analyte, thus relying on existence of a spectroscopic "finger print" (Mittleman et al., 1998; Harmon and Cheville, 2004; Guo et al., 2007) for the detection and differentiation of a target. Moreover, when target analyte is weakly absorbing (which is, for example, the case for gas detection) one typically needs a several meter long gas cell to be able to measure absorption spectrum reliably. In a strike contrast to spectroscopic detection, SPR-based sensors can achieve the same sensitivity for low absorbing analytes in devices of only a few centimeters of length.

6.3 THz plasmon-like excitation at the PVDF/air interface

We start by explaining general ideas behind the principles of operation of a fiber-based SPR sensor. A typical configuration of such a sensor is a fiber with a thin metal layer deposited on its surface in the near proximity of a fiber core. Another side of a metal layer is facing the analyte to be monitored. During operation of a sensor, one launches a broadband light into the fiber core. In the vicinity of a specific wavelength defined by the sensor design, one of the core modes is phase matched (avoiding crossing of the corresponding dispersion relations) with a plasmon excitation mode confined to the metal/analyte interface. In the vicinity of such a resonant wavelength one observes dramatic decrease in the power transmitted through the fiber due to partial energy transfer from the core guided mode into a lossy plasmon wave. As dispersion relation of a plasmon mode is very sensitive to the refractive index of the analyte, resonant wavelength, and hence, spectral position of the absorption peak will shift when analyte refractive index is changed. By detecting spectral shift in the absorption peak of a core guided mode, changes in the analyte refractive index on the order of $10^{-4} - 10^{-5}$ RIU (Refractive Index Units) can be detected.

Based on the theory governing plasmon surface waves, effective refractive index of a plasmon excitation is typically close, while somewhat higher, than that of the analyte. On the other hand, effective refractive index of a fiber mode guided in a solid core is close to that of the core material. As there are no readily available optical materials that have refractive indices near 1, in practice, it becomes challenging to achieve phase matching between the plasmon and core guided modes when working with gaseous analytes. One solution (Skorobogatiy and Kabashin, 2006a; Gauvreau et al., 2007) that we have proposed to resolve the phase matching problem in the visible range was to use photonic bandgap fibers to design the effective refractive index of a core guided mode to be low enough so that phase matching with a plasmon becomes possible. The key advantage of

using the photonic bandgap fibers is that fundamental core guided mode in such fibers can be, in principle, designed to have arbitrarily small effective refractive index. In practice, we have realized that photonic bandgap fibers that support Gaussian-like core mode with too low of an effective refractive index, necessarily have very small core sizes, thus leading to coupling challenges.

An alternative solution to the phase matching problem is to greatly lower the effective refractive index of a core guided mode by making the material of a fiber core highly porous (with the pore sizes being sub-wavelength). Such approach in THz regime has an additional advantage of low loss guidance outside of a phase matching point with a plasmon, as effective material absorption is greatly reduced in porous materials. As a particular design for such a fiber we consider a Teflon rod of 1480 μm diameter having porous core in the form of 4 layers of hexagonally arranged subwavelength holes. In the following simulations the hole-to-hole distance (the pitch) is considered to be 86 μm, while the hole diameter is 76 μm. The refractive indices of Teflon and air are taken to be 1.59 and 1.0 respectively. From outside, the teflon rod is covered with a thin PVDF layer facing air. In the following simulations we consider two thicknesses of a PVDF layer - 30 μm and 35 μm. Sub-wavelength single mode porous fibers for THz have been first introduced in (Hassani et al., 2008b; Hassani et al., 2008c), and they were demonstrated to support Gaussian-like fundamental mode with effective refractive index close to 1, while being also resistent to bending losses even for tight bending radii.

As detailed in (Hassani et al., 2008b; Hassani et al., 2008c), introduction of sub-wavelength holes in the fiber core allows to lower dramatically the effective refractive index of the core guided mode. This, in turn, makes phase matching possible between the core guided mode and THz plasmon propagating at the PVDF/air interface. Furthermore, outside of the phase matching point, most energy in the Gaussian-like core mode is guided in the subwavelength holes, thus resulting in greatly reduced absorption loss. In Fig. 6.3 we present dispersion relation and losses of a core guided and plasmonic modes for

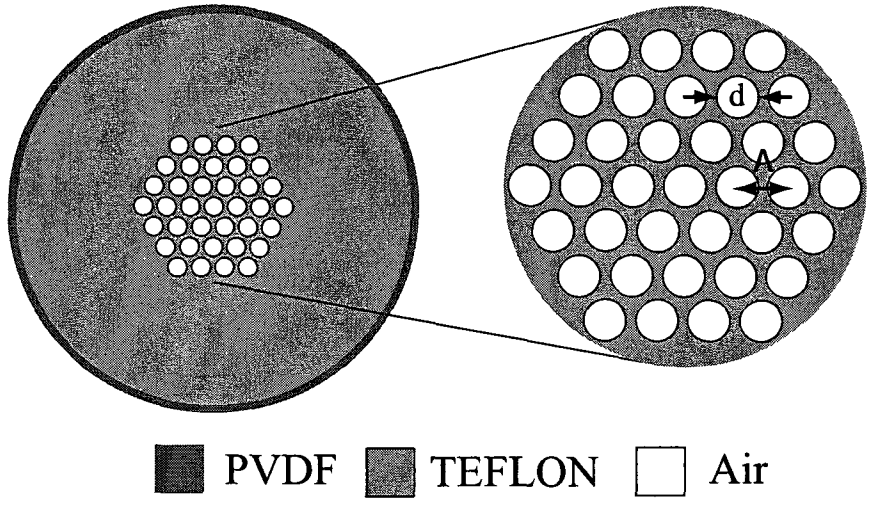

FIG. 6.2 – *Schematic of a porous THz fiber with a PVDF layer facing analyte.*

a structure defined in Fig. 6.2. Particularly, Fig. 6.3(a) presents the effective refractive index of the core guided and plasmon modes as a function of wavelength for the two values of a PVDF thickness. Avoided mode crossing between the two modes around the wavelength of 300 μm is clearly visible. In Fig. 6.3 (b), losses of the core guided and plasmonic modes near the point of avoided crossing are shown. Losses of a core guided mode peak ($\sim$ 30dB/cm) at the point of phase matching with a plasmon, while being much lower (<10dB/cm)) outside of the phase matching region (see also Fig. 6.6). In order to highlight increase in core mode losses solely due to its coupling to a plasmon, in our simulations we consider that Teflon material is lossless. In fact, bulk Teflon loss is reported to be $\sim$1.3dB/cm. When added to simulations we find that Teflon material loss increases the loss of a core guided mode by mere 0.2dB/cm in the vicinity of 300 μm. Clearly, loss contribution due to bulk material loss of Teflon is much smaller than loss contribution due to coupling to a plasmon (absorption in a PVDF layer), even outside of a phase matching point.

In Fig. 6.4 we present distribution across the fiber crossection of the longitudinal energy flux component Sz for a core guided mode in the vicinity of a phase matching point. Only

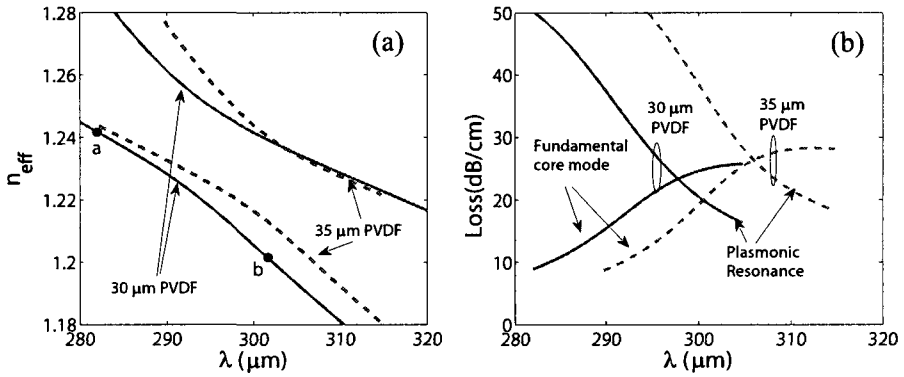

FIG. 6.3 – *Avoided crossing of the dispersion relations of the fundamental core mode and a THz plasmon-like excitation in a porous fiber with PVDF layer. The figure shows the a) real, and b) imaginary parts of the refractive index of the two modes as a function of wavelength.*

1/4 of the fiber crossection is shown due to symmetry. Fig. 6.4(a),(b), correspond to the points (a) and (b) on the core mode dispersion curve in Fig. 6.3(a). As expected, near the phase matching point core mode (high flux intensity in the air holes in the porous core) is strongly hybridized with a plasmon (high flux intensity at the PVDF/air interface).

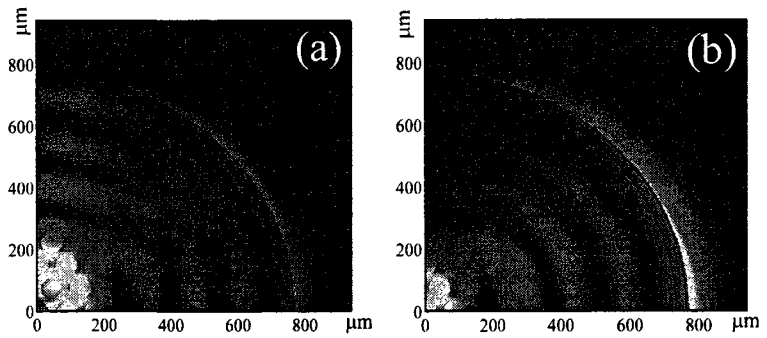

FIG. 6.4 – *Longitudinal energy flux component distribution across the fiber crossection for the core guided mode in the vicinity of a phase matching point with a plasmon. Plots (a) and (b) are calculated for the points (a) and (b) in Fig. 6.3a).*

In Fig. 6.5 we also present dispersion of a core guided mode versus wavelength in the vicinity of a phase matching point. Two solid curves in Fig. 6.5 correspond to the two

values of the air refractive index $n_a = 1$ and $n_a = 1.01$ (only the refractive index of air outside the fiber is varied), assuming PVDF layer thickness of 30 μm. All the dispersion curves show a positive peak at the phase matching point, while passing through zero and becoming negative outside of the phase matching region. Note that even a small change in the air refractive index changes considerably dispersion of a core guided mode near the phase matching point. Thus, a 1% increase in the air refractive index shifts the dispersion peak by about 2 μm, while reducing mode dispersion by about 20 ps/nm-km (from about 35 ps/nm-km). Such strong changes are related to the sensitivity of a plasmon mode dispersion relation to the changes in the refractive index of air at the PVDF/air interface. Furthermore, the dispersion of fiber core mode is very sensitive to the PVDF layer thickness. Particularly, dashed line in Fig. 6.5 is computed using $n_a = 1$, and PVDF layer thickness of 35 μm. One observes that the dispersion peak shifts about 4 μm and increases by almost 50 ps/nm-km when the thickness of a PVDF layer increases from 30 to 35 μm.

6.4 Sensitivity of an SPR-like THz sensor

Here, we address the question of sensitivity of a proposed SPR-like sensor to the changes in the refractive index of analyte. One mode of operation of a proposed sensor is by registering at a fixed frequency the changes in the amplitude of a transmitted light. We define $\alpha(\lambda,n_a)$ to be the transmission loss of the fiber core mode as a function of the wavelength and the refractive index of analyte n_a. Considering P_0 to be the power launched into the fiber core mode, the power detected after propagation along the sensor of length L will be $P(L,\lambda,n_a) = P_0 \exp(-\alpha(\lambda,n_a)L)$. For the operational wavelength λ, the amplitude sensitivity to the dn_a change in the analyte refractive index can then be

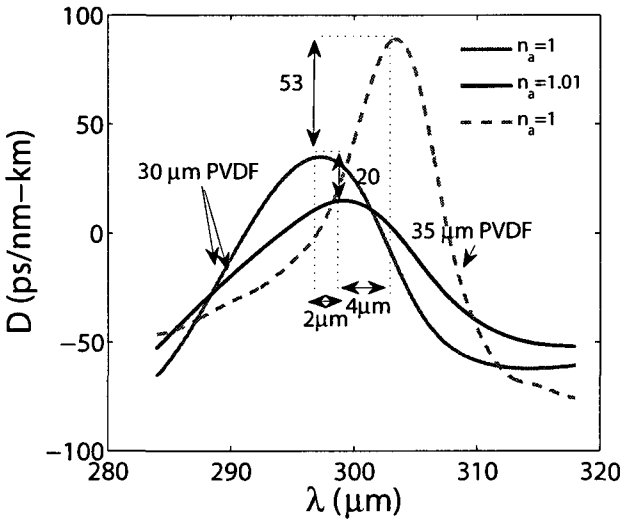

FIG. 6.5 – *Dispersion of the core guided mode of a porous core fiber covered with a thin PVDF layer facing air analyte (see Fig. 6.2). Solid curves - PVDF layer thickness 30 μm, two different values of the air analyte refractive index $n_a = 1$, $n_a = 1.01$. Dashed curve - PVDF layer thickness 35 μm, $n_a = 1$.*

defined as:

$$S_A(\lambda)[RIU^{-1}] = \frac{1}{P(L,\lambda,n_a)} \frac{P(L,\lambda,n_a + dn_a) - P(L,\lambda,n_a)}{dn_a}. \tag{6.2}$$

The sensor length L is typically limited by the modal transmission loss. A reasonable choice of a sensor length is $L = 1/\alpha(\lambda,n_a)$; such a choice of sensor length results in a simple definition of sensitivity with respect to small changes in the analyte refractive index:

$$S_A(\lambda)[RIU^{-1}] = \frac{1}{P(L,\lambda,n_a)} \frac{\partial P(L,\lambda,n_a)}{\partial n_a} = -\frac{1}{\alpha(\lambda,n_a)} \frac{\partial \alpha(\lambda,n_a)}{\partial n_a}. \tag{6.3}$$

In Fig. 6.6 we present amplitude sensitivity of the porous-core fiber-based Surface Plasmon Resonance (SPR) sensor as defined by Eq. (6.3). The maximal sensitivity is achie-

ved at 292 μm and equals to 29 RIU^{-1}. Assuming that 1% change in the transmitted intensity can be reliably detected, sensor resolution of $3.4 \cdot 10^{-4}$ RIU is predicted.

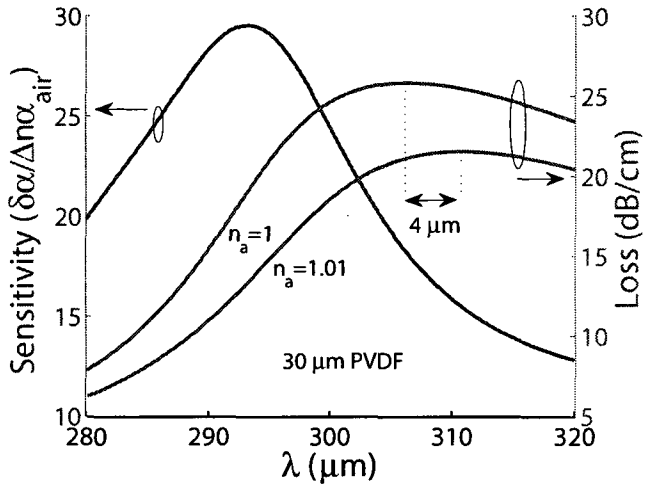

FIG. 6.6 – *Sensitivity of a porous-core fiber sensor featuring a 30 μm PVDF layer facing air analyte (blue line). Losses of a core guided mode versus wavelength (green lines) in the vicinity of a phase matching point with a plasmon for two values of the analyte refractive index* $n_a = 1$, $n_a = 1.01$.

Another way of defining sensor sensitivity is via a spectral measurement. Particularly, by detecting $\Delta\lambda_p$ shift in the position of a resonant absorption peak for Δn_a change in the refractive index of analyte one can define spectral sensitivity as $S_\lambda = \Delta\lambda_p/\Delta n_a$. For example, in Fig. 6.6 we show loss curves of a core guide mode calculated for the two different values of an air analyte refractive index $n_a = 1$ and $n_a = 1.01$. As seen from Fig. 6.6, analyte refractive index change of 0.01 results in a 4 μm shift of a loss peak, thus defining spectral sensitivity to be $S_\lambda = 400$ μm/RIU. Assuming a typical 100 MHz spectral resolution of a time domain THz setup (equivalently 30 nm wavelength resolution at 1 THz), sensor resolution of $1.3 \cdot 10^{-4}$ RIU is predicted.

6.5 Conclusion

In conclusion, fully polymeric SPR-like sensor is demonstrated in THz using porous core fiber covered with a thin feroellectric PVDF layer facing gaseous analyte. Plasmon-like excitation at the PVDF/air interface can be excited by the fiber core mode when phase matching is satisfied. Similarly to the optical SPR sensors, guided core mode exhibits a pronounced loss peak at the point of its phase matching with a plasmon-like mode. Moreover, core mode dispersion varies dramatically in the same phase matching region. By detecting changes in the wavelength of phase matching due to changes in the analyte refractive index, highly sensitive detection systems are possible. We show that both amplitude-based and spectral-based detection methods lead to sensitivities to the changes in the gaseous analyte refractive index on the order of $\sim 10^{-4} RIU$.

CHAPITRE 7

OVERALL DISCUSSION AND CONCLUSION

The overall discussion and conclusion of the materials (5 articles) presented in this thesis proposing the design of novel MOF based SPR sensors for the visible, IR and THz spectral range are presented in this chapter. The designs and results in these articles are divided to two main categories which are the design of the MOF based SPR sensors at visible - IR range and the design of MOF based plasmonic-like sensors at THz. This chapter is organized in the following; first, we discuss and compare the results, presented in chapter 2 and 3, for visible and IR SPR sensors; for example, in term of sensitivity, operation wavelength and etc. Second, we will discuss the design of MOF based plasmonic-like sensors at THz, presented in chapter 4 to 6, including the proposed porous waveguide and then compare plasmonic-like sensors at THz with the ones presented for visible and IR in term of sensitivity and probe depth. Later on, the feasibility of the designs for visible, IR and THz are explained. Finally, because the material presented in this thesis are the first design proposition for MOF based SPR sensors at visible, IR and THz that is not fully covering all of the aspect of these sensors, we suggest the study of noise of MOF based SPR sensors which still need to be investigated for future workss.

The design concept of TIR MOF based SPR sensor and PBG MOF based SPR sensors were presented in chapter 2 and 3. In these chapters, solutions for light-plasmon phase matching and microfluidics difficulties which are two main problems in conventional fiber based SPR were proposed by using TIR and PBG MOFs in the body of SPR sensors.

Generally, at longer wavelength ($\lambda > 0.6\ \mu$m), the index of surface plasmons is near to the index of the analyte bordering the metallic layer . Especially in the IR regime, the

surface plasmon index is respectively around of 1.33 and 1 for aqueous and gaseous analytes, while the modal effective index of light inside conventional fiber is around $\sim$1.45, which is much near to the index of glass. Therefore, light-plasmon phase matching in conventional fiber is possible for high index analyte at lower wavelength, λ<0.6 μm, where the index of surface plasmon reach to $\sim$1.45. On the other hand, lower operation wavelength means lower sensitivity and probe depth, concluding that there is no opportunity for gaseous refractometry sensing using conventional fiber based SPR sensors. To excite surface plasmon at higher wavelength, i.e. $\sim$1 μm, or for lower index analytes, the modal effective index of a fiber has to be tuned to a lower value which matches to that of the surface plasmon at the wavelength of choice. In General, tuning the modal effective index of light in conventional fiber is very limited because of limitation in the size, geometry and choice of material for the core and cladding of the fiber.

In contrast, TIR MOFs and PBG MOFs offer high modal effective index tunability. The core and cladding index of TIR MOFs can be adjusted by the number and position of holes in the core and cladding of these fibers. This gives extensive opportunity of tuning the modal effective index of light propagating inside of TIR MOFs and considerably facilitate the light-plasmon phase matching in MOF based SPR sensors. In a PBG MOF, the periodic structure of air holes along the cladding of a MOF offers a photonic band gap which can be adjusted for the wavelength of choice. This photonic band gap forces light to propagate along the core of PBG MOF regardless of the index of the core, which means the index of core can be less than that of the cladding material; this enables more modal effective index tunability in PBG MOFs versus TIR MOFs. For instant, it is possible to reach to modal effective index of air, $\sim$1, in hollow core MOFs which is not possible using TIR MOFs. However, the design of PBG MOFs are more complex and time consuming with compare to TIR MOFs.

In Table 7.1 shows the maximum amplitude and spectral refractometry sensitivity and operation wavelength of the proposed TIR MOFs and PBG MOFs. The two first rows at

the table shows the sensitivities and operation wavelength of the two TIR MOF based SPR sensors presented in chapter 2. The sensitivity difference of these two sensors is because of the shape of the metallic layers supporting surface plasmons inside the fiber. This shows that the shape of metallic layer, introduced as a new parameter for design of SPR sensors, can be optimized to enhance the SPR refractometry sensitivity. In both designs, phase matching was facilitated by introduction of an airhole along the fiber core.

TAB. 7.1 – *The proposed TIR MOF and PBG MOF based SPR sensors characteristics*

Type of Fiber	Amplitude Sensitivity	Spectral sensitivity	wavelength
TIR MOF I	$8 \cdot 10^{-5}$ RIU	$1.2 \cdot 10^{-4}$ RIU	0.6 μm
TIR MOF II	$5 \cdot 10^{-5}$ RIU	$3 \cdot 10^{-5}$ RIU	0.65 μm
Large Core Bragg Fiber	$3.8 \cdot 10^{-5}$ RIU	$3.3 \cdot 10^{-5}$ RIU	0.697 μm
Small Core Bragg Fiber	$3.7 \cdot 10^{-5}$ RIU	$8.3 \cdot 10^{-6}$ RIU	0.836 μm
Analyte filled Bragg Fiber	$1.4 \cdot 10^{-5}$ RIU	$2.3 \cdot 10^{-5}$ RIU	1.298 μm
Honey Comb PBG MOF			
Peak 1	$2.9 \cdot 10^{-5}$ RIU	$6.3 \cdot 10^{-5}$ RIU	0.6μm
peak 2	$5.9 \cdot 10^{-5}$ RIU	$3.6 \cdot 10^{-5}$ RIU	0.84μm

The rest of the table presents the data for PBG MOFs based SPR sensors, which are based on Bragg fibers (1D PBG fibers) and Honey Comb Photonic Crystal Fibers (2D PBG fibers). By changing the band gap and size or index of the core in the Bragg fibers we illustrate the vast ability of plasmonic excitation from 0.697 μm to 1.298 μm. This shows that The operating wavelength of PBG MOF based SPR sensors can be adjusted anywhere from the visible to near-IR. Furthermore, the last design shows a PBG MOF based SPR sensors with two simultaneous plasmonic peaks excitations, one at visible and another one at IR range, which is impossible using conventional fibers. The maximum amplitude and spectral based refractometry sensitivity for our designs are $1.38 \cdot 10^{-5}$ RIU and $8.3 \cdot 10^{-6}$ RIU, respectively. Worth mentioning that the sensitivities of our MOF based SPR designs are comparable to or even surpass those of the best existing conventional waveguide-based sensor designs (Homola et al., 1999). Furthermore, the table shows some of the PBG MOF based SPR sensors are designed for the near-IR,

while is not possible for conventional fiber based SPR sensors. The probe depth of these sensors operating at near-IR goes beyond 1μm which is $2-3$ times more than that of SPR sensors operating at visible; this enables the detection of biolayer consisting of some bigger sized viruses or bioparticles which their sizes not exceeding this probe depth.

Improved microfluidics in all designs was addressed by the integration of large analyte filled channels adjacent to the fiber core. Moreover, integration of the microfluidic channels during MOF drawing increases sensor reliability as laborious extra step of microfluidics packaging is avoided.

The second part of this thesis is dedicated to the design of waveguide based Plasmonic-like sensors in the THz regime. The design of waveguide based SPR sensors at THz face two main challenges which are the design of a low loss waveguide and finding a material supporting naturally surface palsmons at THz. The first complexity in designing of THz waveguides is the fact that almost all materials are highly absorbent in the THz region. Since the lowest absorption loss occurs in dry air, an efficient waveguide design must maximize the fraction of power guided in the air. Second complexity is that at the THz range unlike the visible and IR range, the large negative permittivity of metals strongly prohibits electromagnetic fields from penetration inside a metal, and plasmon excitation on the metal/dielectric interface becomes challenging. Therefore, the problem of plasmonic excitation at THz have been solved using artificial metamaterials, for which the complex geometrical parameters of metamaterials can tune the electron plasma frequency of metal to the THz range. Design of metamaterials needs laborious design and fabrication and is very time consuming. In chapters 4 and 5 we respectively proposed solutions for the design of a low loss waveguide and a material for natural plasmonic excitation at THz to overcome these two main challenges. Using these solutions, in the chapter 6 (the last article), finally, a THz porous fiber based plasmonic-like SPR sensors is proposed with high refractometry sensitivity for the challenging case of gaseous analytes. In the following, We will discuss and compare the results of these there articles.

The design of low loss porous fibers, guiding in Terahertz regime, for use in the body of our proposed THz plasmonic sensor was addressed in chapter 4. We have proposed a subwavelength porous fiber and a hollow core Bragg fiber for low-loss guidance of THz radiation. The loss and bandwidth of these two fiber are presented in Table 2. The porous polymer fiber is composed of a polymer rod containing hexagonal array of subwavelength air holes. Although, in this design the fiber core diameter is comparable to the operation wavelength, the major portion of THz power launched into the fiber is confined within the air holes inside of the fiber core. Consequently, the modal absorption loss lower than 10 dB/m was achieved with 130 dB/m bulk absorption loss of the fiber material. Furthermore, our calculations shows that porous fibers are highly resistant to bending, with bending loss being smaller than modal absorption loss for bends as tight as 3 cm of radius. The second fiber, hollow core Bragg fibers, made of a set of concentric material layers suspended in air by the network of circular bridges has a total modal loss around of $\sim$ 5 dB/m for material with 130 dB/m absorption loss. Despite of this low absorption loss, the Bragg fiber bandwidth, $\sim$ 0.1 THZ, was found to be smaller than that of the porous fiber $\sim$ 1 THz , becasue of the parasitic coupling to the surface states of the multilayer reflector. The second disadvanatge of the Bragg fiber is that almost all of the power propagating along the hollow core which makes the tuning of modal effective index challenging. Considering the disadvantage of the Hollow Bargg fiber, we choose the subwavelength porous fiber to design the THz plasmonic-like sensor; in this fiber the plasmonic excitation can be facilitated by tuning the modal effective index controlled by the size of airholes inside the core of fiber.

TAB. 7.2 – *Subwavelength Porous and Hollow Bragg Fibers Characteristics at* 1 *THz*

Type of Fiber	Absorption loss	Bandwidth
Subwavelength Porous Fiber	10 dB/m	$\sim$ 1 THz
Hollow Core Bragg Fiber	5 dB/m	$\sim$ 0.1 THz

A solution for THz surface plasmon excitation is proposed in chapter 5, where we notice

that the real part of the PVDF dielectric constant is negative in the wavelength range between 100 μm and 700 μm. Thus, by analogy with the behavior of the metals in the visible range, a PVDF layer is expected to support a plasmon-like excitation in the THz regime which was impossible before while using metal layers in this regime. To illustrate and simulate that a PVDF layer can support surface plasmons at THz, we proposed the design criteria of a solid core Bragg fiber based plasmonic-like THz sensors. In this sensor, the THz plasmon-like excitation on a 10μm PVDF film via phase matching with the fundamental core mode of the solid-core Bragg fiber is demonstrated for analyte index of n_a =1.33. The amplitude-based refractometry resolution as low as $2 \cdot 10^{-4}$ RIU is calculated at 280μm, with the sensor length in a 1 cm range.

Second THz plasmonic-like sensor is proposed in the chapter 6 for refractometry sensing in gaseous analytes, $n_a = 1$. This fully polymeric THz Plasmonic-like sensor is a subwavelength porous core fiber covered with a thin 30μm ferroelectric PVDF layer facing a gaseous analyte. In this design, the low loss porous fiber, proposed in the chapter 4, enables the excitation of surface plasmons at PVDF/air interface by tuning the modal effective index of the fiber core mode to a lower index $n_{eff} = 1.2$ at 300μm. Similarly to the optical SPR sensors, guided core mode exhibits a pronounced loss peak at the point of its phase matching with a plasmon-like mode. By detecting changes in the wavelength of phase matching due to changes in the analyte refractive index, highly sensitive detection systems are possible. The amplitude and spectral based refractometry sensitivity of $3.4 \cdot 10^{-4}$ RIU, and $1.3 \cdot 10^{-4}$ RIU are predicted for gaseous analytes, $n_a = 1$.

Table 7.3 shows the characteristics of the Bragg fiber based Plasmonic-like sensors for aqueous analytes and subwavelength porous fiber based plasmonic sensor for gaseous analytes. The refractometry sensitivity of the the two sensors is in order of $\sim 10^{-4}$ RIU in the THz regime. Comparing with the Table 7.1, even thought the refractometry sensitivity of these two sensors are not more than that of SPR sensors at visible and IR, the operation wavelength of these sensors are roughly about $\sim$300 times of that of those sen-

sors, which leads to probe depth of $\sim 60\ \mu$m. Thus, in direct analogy to SPR sensing in the visible, existence of plasmon-like resonances at the THz enables study of the micron-sized particle binding dynamics within $\sim 10-60\,\mu$m of the sensor surface. This can be of particular interest for the label-free detection of specific bacteria by functionalizing the sensor surface with bacteria specific phages. In comparison, SPR sensors in the visible can only detect binding of nano-molecules with sizes less than $100-300\ \mu$m (size of a plasmon tail), rendering the method insensitive to the larger particles, such as bacteria.

TAB. 7.3 – *Subwavelength Porous and Solid Core Bragg Fiber based THz SPR Sensors*

Type of Fiber	Amplitude Sensitivity	Wavelength	Analyte index
Solid Core Bragg Fiber	$2 \cdot 10^{-4}$ RIU	280 μm	1.33
Subwavelength Porous Fiber	$3.4 \cdot 10^{-4}$ RIU	300 μm	1

Finally, PVDF gives an opportunity to design a fully polymeric structure for THz plasmonic devices using such established mass production techniques as micro-embossing and fiber drawing, which potentially makes the fabrication process highly suitable for the industrial scale-up.

The discussion about feasibility of sensors can be divided to two parts, which are feasibility of the proposed sensors at visible - IR and THz. The feasibility for visible - IR sensors has two factors, the possibility of fabrication of the MOFs at visible - IR and the possibility of gold coating inside holes. TIR and PBG MOFs are commercially available, and current technology enables fabrication of MOFs with the structures in the range sizes we proposed. On the other hand, the deposition of metal layers inside of the microstructured optical fiber is recently reported either with high pressure Chemical Vapor Deposition (CVD) technique (Sazio et al., 2006) or wet chemistry deposition technique used in fabrication of metal covered hollow waveguides (Harrington, 2000). Thus the proposed structures are feasible. Regarding to feasibility of the THz subwavelength porous fiber based plasmonic-like sensors, the proposed low loss porous polymer fiber is fabricated in our group (Dupuis et al., 2009). The driving factor for the development

of porous all-dielectric fibers is that such fibers can be fabricated from a single material using standard fiber drawing techniques, which is, potentially, simpler than fabrication of metal coated waveguides due to omission of a coating step.

Even thought, we have covered many design aspects of the MOF based SPR sensors in this thesis, there are some parameters such as noise which can be studied in future works. Temperature and multimode excitation are two main source of noise at the conventional based SPR sensors. The refractive index of a dielectric, i.e. glass or polymer, is a function of temperature. Thus, a change in the ambient temperature changes the modal effective index of the core fiber, resulting in changing the phase matching wavelength while the analyte index remains constant. Multimode excitation in a fiber is the second source of noise. Because each core mode has a corresponding propagation constant exciting surface plasmon at a different wavelength, a wide plasmonic peak, which is the superposition of the several plasmonic peaks can be observed at a multimode fiber based SPR sensors. This wide plasmonic peaks reduce the refractometry resolution of the SPR sensor. As a rule of thump we can expect that the noise in the MOF based SPR sensors can be reduced more than that of the conventional fiber based SPR sensors, because the MOFs can be designed to be $3-6$ times less sensitive to temperature than single mode fibers (Dangui et al., 2005) and operating in endlessly single mode regime (Saitoh et al., 2005), which is not possible for conventional fibers. Therefore, as a future work we suggest to study and model the noise of MOF based SPR sensors and compare it with that of conventional fiber based SPR sensors.

RÉFÉRENCES

Agranovich, V. M. and Mills, D. L. (1982). *Surface Polaritons - Electromagnetic Waves at Surfaces and Interfaces.* North- Holland.

Al-Bader, S. J. and Imtaar, M. (1993). Optical fiber hybrid-surface plasmon polaritons. *J. Opt. Soc. Am. B*, **10**(1), 83.

Alonso, R., as, J. S., Pelayo, J., Villuendas, F., and Tornos, J. (1994). Single-mode, optical-fiber sensors and tunable wavelength filters based on the resonant excitation of metal-clad modes. *Appl. Opt.*, **33**(22), 5197–5201.

Alonso, R., Villuendas, F., Tornos, J., and Pelayo, J. (1993). New ['']in-line' optical-fibre sensor based on surface plasmon excitation. *Sensors and Actuators A: Physical*, **37-38**, 187 – 192.

Amodio, P. and Paprzycki, M. (1997). A cyclic reduction approach to the numerical solution of boundary value odes. *SIAM J. Sci. Comput.*, **18**(1), 56–68.

Argyros, A., Bassett, I., van Eijkelenborg, M., Large, M., Zagari, J., Nicorovici, N. A., McPhedran, R., and de Sterke, C. M. (2001). Ring structures in microstructured polymer optical fibres. *Opt. Express*, **9**(13), 813–820.

Argyros, A., van Eijkelenborg, M. A., Large, M. C., and Bassett, I. M. (2006). Hollow-core microstructured polymer optical fiber. *Opt. Lett.*, **31**(2), 172–174.

Balachandran, R. M., Pacheco, D. P., and Lawandy, N. M. (1996). Photonic textile fibers. *Appl. Opt.*, **35**(12), 1991–1994.

Barkou, S. E., Broeng, J., and Bjarklev, A. (1999). Silica-air photonic crystal fiber design that permits waveguiding by a true photonic bandgap effect. *Opt. Lett.*, **24**(1), 46–48.

Benoit, G., Hart, S., Temelkuran, B., Joannopoulos, J., and Fink, Y. (2003). Static and dynamic properties of optical micro-cavities in photonic bandgap yarns. *Adv. Mater.*, **15**, 2053–2056.

Berzowska, J. (2004). Very slowly animating textiles: Shimmering flower. In *SIGGRAPH 2004, proceedings of the 31st international conference on computer graphics and interactive techniques.*

Bise, R., Jasapara, J., Steinvurzel, P., and DiGiovanni, D. (2002). Temperature tuning of dispersion in a photonic band gap fiber. *Lasers and Electro-Optics, 2002. CLEO '02. Technical Digest. Summaries of Papers Presented at the*, pages 614–615 vol.1.

Bock, W. and Urbanczyk, W. (2004). Measurements of sensitivity of birefringent holey fiber to temperature, elongation, and hydrostatic pressure. *Instrumentation and Measurement Technology Conference, 2004. IMTC 04. Proceedings of the 21st IEEE*, **2**, 1228–1232 Vol.2.

Busch, K. and John, S. (1999). Liquid-crystal photonic-band-gap materials: The tunable electromagnetic vacuum. *Phys. Rev. Lett.*, **83**, 967–970.

Cao, Q. and Jahns, J. (2005). Azimuthally polarized surface plasmons as effective terahertz waveguides. *Opt. Express*, **13**(2), 511–518.

Chan, W. L., Deibel, J., and Mittleman, D. M. (2007). Imaging with terahertz radiation. *Reports on Progress in Physics*, **70**(8), 1325–1379.

Chen, L.-J., Chen, H.-W., Kao, T.-F., Lu, J.-Y., and Sun, C.-K. (2006). Low-loss subwavelength plastic fiber for terahertz waveguiding. *Opt. Lett.*, **31**(3), 308–310.

Cinteza, L. O., Ohulchanskyy, T. Y., Sahoo, Y., Bergey, E. J., Pandey, R. K., and Prasad, P. N. (2006). Diacyllipid micelle-based nanocarrier for magnetically guided delivery of drugs in photodynamic therapy. *Molecular Pharmaceutics*, **3**(4), 415–423.

Clare J. Strachan, Philip F. Taday, D. A. N. K. C. G. J. A. Z. M. P. T. R. (2005). Using terahertz pulsed spectroscopy to quantify pharmaceutical polymorphism and crystallinity. *Journal of Pharmaceutical Sciences*, **94**(4), 837–846.

Cook, D. J., Decker, B. K., and Allen, M. G. (2005). Quantitative thz spectroscopy of explosive materials. In *Optical Terahertz Science and Technology*, page MA6. Optical Society of America.

Cordeiro, C. M. B., Franco, M. A. R., Chesini, G., Barretto, E. C. S., Lwin, R., Cruz, C. H. B., and Large, M. C. J. (2006). Microstructured-core optical fibre for evanescent sensing applications. *Opt. Express*, **14**(26), 13056–13066.

Crystal-fibre. http://www.crystal-fibre.com.

Ctyroky, J., Abdelmalek, F., Ecke, W., and Usbeck, K. (1999a). Modelling of the surface plasmon resonance waveguide sensor with bragg grating. *Opt. Quantum Electron.*, **31**, 927.

Ctyroky, J., Homola, J., Lambeck, P. V., Musa, S., Hoekstra, H. J. W. M., Harris, R. D., Wilkinson, J. S., Usievich, B., and Lyndin, N. M. (1999b). Theory and modelling of optical waveguide sensors utilising surface plasmon resonance. *Sens. Actuators B*, **54**, 66.

D'Amato, E. (2002). Stress-strain monitoring in textile composites by means of optical fibers. *Exp. Techniques & Design in Composite Mat.*, **221**, 245–253.

Dangui, V., Kim, H., Digonnet, M., and Kino, G. (2005). Phase sensitivity to temperature of the fundamental mode in air-guiding photonic-bandgap fibers. *Opt. Express*, **13**(18), 6669–6684.

Diez, A., Andres, M. V., and Cruz, J. L. (2001). In-line fiber-optic sensors based on the excitation of surface plasma modes in metal-coated tapered fibers. *Sens. Actuators B*, **73**, 95.

Ditlbacher, H., Galler, N., Koller, D. M., Hohenau, A., Leitner, A., Aussenegg, F. R., and Krenn, J. R. (2008). Coupling dielectric waveguide modes to surface plasmon polaritons. *Opt. Express*, **16**(14), 10455–10464.

Dostalek, J., Ctyroky, J., Homola, J., Brynda, E., Skalsky, M., Nekvindova, P., Spirkova, J., Skvor, J., and Schrofel, J. (2001). Surface plasmon resonance biosensor based on

integrated optical waveguide. *Sens. Actuators B*, **76**, 8.

Dupuis, A., Allard, J.-F., Morris, D., Stoeffler, K., Dubois, C., and Skorobogatiy, M. (2009). Fabrication and thz loss measurements of porous subwavelength fibers using a directional coupler method. *Opt. Express*, **17**(10), 8012–8028.

Dupuis, A., Gao, Y., Guo, N., Pone, E., Godbout, N., Lacroix, S., Dubois, C., and Skorobogatiy, M. (2006). Biodegradable, double-core, porous optical fiber for sensing applications. In *Optical Fiber Sensors*, page WA2. Optical Society of America.

Dupuis, A., Guo, N., Gao, Y., Gauvreau, B., Dubois, C., and Skorobogatiy, M. (2008a). Prospects for "green" microstuctured optical fibers. In *Conference on Lasers and Electro-Optics/Quantum Electronics and Laser Science Conference and Photonic Applications Systems Technologies*, page CTuMM5. Optical Society of America.

Dupuis, A., Guo, N., Gao, Y., Godbout, N., Lacroix, S., Dubois, C., and Skorobogatiy, M. (2007a). Prospective for biodegradable microstructured optical fibers. *Opt. Lett.*, **32**(2), 109–111.

Dupuis, A., Guo, N., Gauvreau, B., Hassani, A., Pone, E., Boismenu, F., and Skorobogatiy, M. (2007b). Guiding in the visible with "colorful" solid-core bragg fibers. *Opt. Lett.*, **32**(19), 2882–2884.

Dupuis, A., Guo, N., Gauvreau, B., Hassani, A., Pone, E., Boismenu, F., and Skorobogatiy, M. (2008b). All-fiber spectral filtering with solid core photonic band gap bragg fibers. In *Optical Fiber Communication Conference and Exposition and The National Fiber Optic Engineers Conference*, page OThM3. Optical Society of America.

Dupuis, A., Guo, N., Gauvreau, B., Hassani, A., Pone, E., Boismenu, F., and Skorobogatiy, M. (2008c). All-fiber spectral filtering with solid core photonic band gap bragg fibers. In *Optical Fiber Communication Conference and Exposition and The National Fiber Optic Engineers Conference*, page OThM3. Optical Society of America.

Dupuis, A., Guo, N., Gauvreau, B., Hassani, A., Pone, E., Boismenu, F., and Skorobogatiy, M. (2008d). "colorful" solid-core bragg fibers guiding in the visible. In *Confe-*

rence on Lasers and Electro-Optics/Quantum Electronics and Laser Science Conference and Photonic Applications Systems Technologies, page CTuMM2. Optical Society of America.

El-Sherif, M., Yuan, J., and MacDiarmid, A. (2000). Fiber optic sensors and smart fabrics. *J. Intelligent Mat. Systems & Struct.*, **11**, 407–414.

Emiliyanov, G., Jensen, J. B., Bang, O., Hoiby, P. E., Pedersen, L. H., Kjær, E. M., and Lindvold, L. (2007). Localized biosensing with topas microstructured polymer optical fiber. *Opt. Lett.*, **32**(5), 460–462.

Engeness, T., Ibanescu, M., Johnson, S., Weisberg, O., Skorobogatiy, M., Jacobs, S., and Fink, Y. (2003). Dispersion tailoring and compensation by modal interactions in omniguide fibers. *Opt. Express*, **11**(10), 1175–1196.

Fudouzi, H. and Xia, Y. (2003). Colloidal crystals with tunable colors and their use as photonic papers. *Langmuir*, **19**, 9653–9660.

Gallot, G., Jamison, S. P., McGowan, R. W., and Grischkowsky, D. (2000). Terahertz waveguides. *J. Opt. Soc. Am. B*, **17**(5), 851–863.

Gao, Y., Guo, N., Gauvreau, B., Rajabian, M., Skorobogata, O., Pone, E., Zabeida, O., Martinu, L., Dubois, C., and Skorobogatiy, M. (2006). Consecutive solvent evaporation and co-rolling techniques for polymer multilayer hollow fiber preform fabrication. *J. Mat. Res.*, **21**, 2246–2254.

Garvey, D. W., Zimmerman, K., Young, P., Tostenrude, J., Townsend, J. S., Zhou, Z., Lobel, M., Dayton, M., Wittorf, R., Kuzyk, M. G., Sounick, J., and Dirk, C. W. (1996). Single-mode nonlinear-optical polymer fibers. *J. Opt. Soc. Am. B*, **13**(9), 2017–2023.

Gauvreau, B., Hassani, A., Fehri, M. F., Kabashin, A., and Skorobogatiy, M. A. (2007). Photonic bandgap fiber-based surface plasmon resonance sensors. *Opt. Express*, **15**(18), 11413–11426.

Gauvreau, B., Khadri, D., Guo, N., and Skorobogatiy, M. (2008). Suspended core high numerical aperture multimode polymer fiber. In *Conference on Lasers and Electro-*

Optics/Quantum Electronics and Laser Science Conference and Photonic Applications Systems Technologies, page CThV7. Optical Society of America.

Ghosh, S., Amidei, C., and Furrow, K. (2005). Development of a sensor-embedded flexible textile structure for apparel or large area applications. *Indian J. Fibre & Textile Res.*, **30**, 42–48.

Goto, M., Quema, A., Takahashi, H., Ono, S., and Sarukura, N. (2004). Teflon photonic crystal fiber as terahertz waveguide. *Japanese Journal of Applied Physics*, **43**(2B), L317–L319.

Grasso, M., Hunn, B., and Rewerts, A. (1997). Effect of textile properties in evaluating a directional shading fabric. *Textile Res. J.*, **67**, 233–247.

Grigorenko, A. N., Nikitin, P., and Kabashin, A. V. (1999). Phase jumps and interferometric surface plasmon resonance imaging. *Appl. Phys. Lett.*, **75**, 3917.

Guo, R., Akiyama, K., Minamide, H., and Ito, H. (2007). Frequency-agile terahertz-wave spectrometer for high-resolution gas sensing. *Applied Physics Letters*, **90**(12), 121127.

Guobin, R., Zhi, W., Shuqin, L., Yan, L., and Shuisheng, J. (2004). Full-vectorial analysis of complex refractive index photonic crystal fibers. *Opt. Express*, **12**(6), 1126–1135.

Gupta, B. D. and Sharma, A. K. (2005). Sensitivity evaluation of a multi-layered surface plasmon resonance-based fiber optic sensor: a theoretical study. *Sens. Actuators B*, **107**, 40.

Han, H., Park, H., Cho, M., and Kim, J. (2002). Terahertz pulse propagation in a plastic photonic crystal fiber. *Appl. Phys. Lett.*, **80**, 2634.

Hardaker, S. and Gregory, R. (2003). Progress toward dynamic color-responsive "chameleon" fiber systems. *MRS Bull.*, **28**, 564–567.

Harlin, A., Makinen, M., and Vuorivirta, A. (2003). Development of polymeric optical fibre fabrics as illumination elements and textile displays. *AUTEX Res. J.*, **3**.

Harmon, S. A. and Cheville, R. A. (2004). Part-per-million gas detection from long-baseline thz spectroscopy. *Applied Physics Letters*, **85**(11), 2128–2130.

Harrington, J., George, R., Pedersen, P., and Mueller, E. (2004). Hollow polycarbonate waveguides with inner cu coatings for delivery of terahertz radiation. *Opt. Express*, **12**(21), 5263–5268.

Harrington, J. A. (2000). A review of ir transmitting, hollow waveguides. *Fiber and Integrated Optics*, **19**, 211 – 227.

Harris, R. and Wilkinson, J. S. (1995). Waveguide surface plasmon resonance sensors. *Sens. Actuators B*, **29**, 261.

Hart, S., Maskaly, G., Temelkuran, B., Prideaux, P., Joannopoulos, J., and Fink, Y. (2002). External reflection from omnidirectional dielectric mirror fibers. *Science*, **296**, 510–513.

Hassani, A., Dupuis, A., and Skorobogatiy, M. (2008a). Low loss porous terahertz fibers containing multiple subwavelength holes. *Applied Physics Letters*, **92**(7), 071101.

Hassani, A., Dupuis, A., and Skorobogatiy, M. (2008b). Low loss porous terahertz fibers containing multiple subwavelength holes. *Applied Physics Letters*, **92**(7), 071101.

Hassani, A., Dupuis, A., and Skorobogatiy, M. (2008c). Porous polymer fibers for low-loss terahertz guiding. *Opt. Express*, **16**(9), 6340–6351.

Hassani, A., Dupuis, A., and Skorobogatiy, M. (2008d). Surface-plasmon-resonance-like fiber-based sensor at terahertz frequencies. *J. Opt. Soc. Am. B*, **25**(10), 1771–1775.

Hassani, A., Gauvreau, B., Fehri, M. F., Kabashin, A., and Skorobogatiy, M. A. (2008e). Photonic crystal fiber and waveguide-based surface plasmon resonance sensors for applications in the visible and near-ir. *Electromagnetics, Special Issue in Surface Waves and Complex Mediums*, **28**, 198–213.

Hassani, A., Gauvreau, B., and Skorobogatiy, M. (2008f). Novel photonic crystal fiber sensors using splitting of a degenerate plasmonic doublet. In *Conference on Lasers*

and Electro-Optics/Quantum Electronics and Laser Science Conference and Photonic Applications Systems Technologies, page CMJ1. Optical Society of America.

Hassani, A. and Skorobogatiy, M. (2006). Design of the microstructured optical fiber-based surface plasmon resonance sensors with enhanced microfluidics. *Opt. Express*, **14**(24), 11616–11621.

Hassani, A. and Skorobogatiy, M. (2007a). Design criteria for microstructured-optical-fiber-based surface-plasmon-resonance sensors. *J. Opt. Soc. Am. B*, **24**(6), 1423–1429.

Hassani, A. and Skorobogatiy, M. (2007b). Practical design of microstructured optical fibers for surface plasmon resonance excitation. In *Conference on Lasers and Electro-Optics/Quantum Electronics and Laser Science Conference and Photonic Applications Systems Technologies*, page CWO4. Optical Society of America.

Hassani, A. and Skorobogatiy, M. (2007c). Practical design of microstructured optical fibers for surface plasmon resonance sensing. In *Optical Fiber Communication Conference and Exposition and The National Fiber Optic Engineers Conference*, page OThA5. Optical Society of America.

Hassani, A. and Skorobogatiy, M. (2008). Surface plasmon resonance-like integrated sensor at terahertz frequencies for gaseous analytes. *Opt. Express*, **16**(25), 20206–20214.

Hatcher, M. (2002). France telecom debuts fiber screen. *Optics.org News*.

Hautakorpi, M., Mattinen, M., and Ludvigsen, H. (2008). Surface-plasmon-resonance sensor based on three-hole microstructured optical fiber. *Opt. Express*, **16**(12), 8427–8432.

Hidaka, T., Minamide, H., Ito, H., ichi Nishizawa, J., Tamura, K., and Ichikawa, S. (2005). Ferroelectric pvdf cladding terahertz waveguide. *J. Lightwave Technol.*, **23**(8), 2469.

Holman, J. (1981). *Heat Transfer*. McGraw-Hill.

Homola, J. (1995). Optical fiber sensor based on surface plasmon resonance excitation. *Sens. Actuators B*, **29**, 401.

Homola, J., Ctyroky, J., Skalky, M., Hradiliva, J., and Kolarova, P. (1997a). A surface plasmon resonance based integrated optical sensor. *Sens. Actuators B*, **39**, 286.

Homola, J., Slavik, R., and Ctyroky, J. (1997b). Interaction between fiber modes and surface plasmon waves: spectral properties. *Opt. Lett.*, **22**(18), 1403–1405.

Homola, J., Yee, S. S., and Gauglitz, G. (1999). Surface plasmon resonance sensors: review. *Sens. Act. B*, **54**, 3–15.

I. Maekawa, T. Gunji, T. T. Study on optical properties of silk-like fabrics. *J. Textile Machinery Soc. Japan*, **30**, 18–27.

Ito, T., Matsuura, Y., Miyagi, M., Minamide, H., and Ito, H. (2007). Flexible terahertz fiber optics with low bend-induced losses. *J. Opt. Soc. Am. B*, **24**(5), 1230–1235.

Jackson, J. D. (1998). *Classical Electrodynamics.* Wiley.

Jaluria, Y. and Torrance, K. E. (2003). *Computational heat transfer.* Tyalor & Francis.

Jamison, S. P., McGowan, R. W., and Grischkowsky, D. (2000). Single-mode waveguide propagation and reshaping of sub-ps terahertz pulses in sapphire fibers. *Applied Physics Letters*, **76**(15), 1987–1989.

Jeon, T.-I., Zhang, J., and Grischkowsky, D. (2005). Study of the thz sommerfeld wave on single metal wires. In *Conference on Lasers and Electro-Optics/Quantum Electronics and Laser Science and Photonic Applications Systems Technologies*, page CFM5. Optical Society of America.

Jiang, Y., Chen, X., Howley, B., Chen, M. Y., and Chen, R. T. (2006). Effects of temperature fluctuation on highly dispersive photonic crystal fibers. *Applied Physics Letters*, **88**(1), 011108.

Jin, J. (2002). *The Finite Element Method in Electromagnetics.* John Wiley & Sons, Inc., New York.

Jin, Y., Kim, G., and Jeon, S. (2006). Terahertz dielectric properties of polymers. *Journal of the Korean Physical Society*, **49**, 513–517.

jin Yu, R., qiang Zhang, Y., Zhang, B., ran Wang, C., and qi Wu, C. (2007). New cobweb-structure hollow bragg optical fibers. *Optoelectronics Letters*, **3**(1), 10–13.

Joannopoulos, J. D., Johnson, S. G., Winn, J. N., and Meade, R. D. (2008). *Photonic Crystals: Molding the Flow of Light.* Princeton University Press.

Johnson, S., Ibanescu, M., Skorobogatiy, M., Weisberg, O., Engeness, T., Soljacic, M., Jacobs, S., Joannopoulos, J., and Fink, Y. (2001). Low-loss asymptotically single-mode propagation in large-core omniguide fibers. *Opt. Express*, **9**(13), 748–779.

Jorgenson, R. C. and Yee, S. S. (1993). A fiber-optic chemical sensor based on surface plasmon resonance. *Sens. Actuators B*, **12**, 213.

Ju, J., Wang, Z., Jin, W., and Demokan, M. (2005). Temperature sensitivity of a two-mode photonic crystal fiber interferometer. *Lasers and Electro-Optics Society, 2005. LEOS 2005. The 18th Annual Meeting of the IEEE*, pages 873–874.

Kabashin, A. V. and Nikitin, P. (1998). Surface plasmon resonance interferometer for bio- and chemical-sensors. *Opt. Commun.*, **150**, 5.

Kawase, K., Ogawa, Y., Watanabe, Y., and Inoue, H. (2003). Non-destructive terahertz imaging of illicit drugs using spectral fingerprints. *Opt. Express*, **11**(20), 2549–2554.

Kerbage, C., Ging, J., Hale, A., and Eggleton, B. (2002a). Coherent microfluidic resonances in microstructured optical fiber. *Lasers and Electro-Optics Society, 2002. LEOS 2002. The 15th Annual Meeting of the IEEE*, **2**, 813–814 vol.2.

Kerbage, C., Steinvurzel, P., Hale, A., Windeler, R., and Eggleton, B. (2002b). Birefringent tunable hybrid microstructured optical fiber. *Lasers and Electro-Optics, 2002. CLEO '02. Technical Digest. Summaries of Papers Presented at the*, pages 14 vol.1–.

Kim, D.-H. and Kang, J. (2004). Sagnac loop interferometer based on polarization maintaining photonic crystal fiber with reduced temperature sensitivity. *Opt. Express*, **12**(19), 4490–4495.

Kiwa, T., Tonouchi, M., Yamashita, M., and Kawase, K. (2003). Laser terahertz-emission microscope for inspecting electrical faults in integrated circuits. *Opt. Lett.*, **28**(21), 2058–2060.

Knight, J. C., Birks, T. A., Russell, P. S. J., and Atkin, D. M. (1996). All-silica single-mode optical fiber with photonic crystal cladding. *Opt. Lett.*, **21**(19), 1547–1549.

Knight, J. C., Birks, T. A., Russell, P. S. J., and Rarity, J. G. (1998). Bragg scattering from an obliquely illuminated photonic crystal fiber. *Appl. Opt.*, **37**(3), 449–452.

Koike, Y., Ishigure, T., and Nihei, E. (1995). High-bandwidth graded-index polymer optical fiber. *J. Lightwave Technol.*, **13**, 1475.

Kojovic, A., Zivkovic, I., Brajovic, L., Mitrakovic, D., and Aleksic, R. (2005). Low energy impact damage detection in laminar termoplastic composite materials by means of embedded optical fibers. *Current Res. Adv. Mat.*, **494**, 481–486.

Koncar, V. (2005). Optical fiber fabric displays. *Opt. Photon. News*, **16**(4), 40–44.

Kretschmann, E. and Raether, H. (1968). Radiative decay of non-radiative surface plasmons excited by light. *Z. Naturforsch*, **A23**, 2135–2136.

Kuang, K. and Cantwell, W. (2003). Detection of impact damage in thermoplastic-based glass fiber composites using embedded optical fiber sensors. *J. Thermoplastic Composite Mat.*, **16**, 213–229.

Kuhlmey, B. T., Pathmanandavel, K., and McPhedran, R. C. (2006). Multipole analysis of photonic crystal fibers with coated inclusions. *Opt. Express*, **14**(22), 10851–10864.

Kurihara K, Nakamura K, H. E. S. K. (2002). An absorption-based surface plasmon resonance sensor applied to sodium ion sensing based on an ion-selective optode membrane. *Anal Chem.*, **24**(74), 6323–33.

Kuriki, K., Koike, Y., and Okamoto, Y. (2002). Plastic optical fiber lasers and amplifiers containing lanthanide complexes. *Chem. Rev.*, **102**, 2347.

Lægsgaard, J. and Alkeskjold, T. T. (2006). Designing a photonic bandgap fiber for thermo-optic switching. *J. Opt. Soc. Am. B*, **23**(5), 951–957.

Larsen, T., Bjarklev, A., Hermann, D., and Broeng, J. (2003). Optical devices based on liquid crystal photonic bandgap fibres. *Opt. Express*, **11**(20), 2589–2596.

Lavers, C. P. and Wilkinson, J. (1994). A waveguide-coupled surface-plasmon sensor for an aqueous environment. *Sens. Actuators B*, **22**, 75.

Lee, J., Seo, M., Park, D., Kim, D., Jeoung, S., Lienau, C., Park, Q.-H., and Planken, P. (2006). Shape resonance omni-directional terahertz filters with near-unity transmittance. *Opt. Express*, **14**(3), 1253–1259.

Liedberg, B., Nylander, C., and Lundstrom, I. Surface plasmon resonance for gas detection and biosensing. *Sens. Actuators B*, **4**, 299.

Limpert, J., Schreiber, T., Liem, A., Nolte, S., Zellmer, H., Peschel, T., Guyenot, V., and Tünnermann, A. (2004). Thermo-optical properties of air-clad photonic crystal fiber lasers in high power operation. In *Advanced Solid-State Photonics (TOPS)*, page 90. Optical Society of America.

Löffler, T., Bauer, T., Siebert, K., Roskos, H., Fitzgerald, A., and Czasch, S. (2001). Terahertz dark-field imaging of biomedical tissue. *Opt. Express*, **9**(12), 616–621.

Lumigram. http://www.lumigram.com.

Lumitex. http://www.lumitex.com/technologies.html.

Lyytikäinen, K., Zagari, J., Barton, G., and Canning, J. (2004). Heat transfer within a microstructured polymer optical fibre preform. *Modelling and Simulation in Materials Science and Engineering*, **12**(3), S255–S265.

Maier, S. A., Andrews, S. R., Martín-Moreno, L., and García-Vidal, F. J. (2006). Terahertz surface plasmon-polariton propagation and focusing on periodically corrugated metal wires. *Physical Review Letters*, **97**(17), 176805.

Martynkien, T., Szpulak, M., and Urbanczyk, W. (2005). Modeling and measurement of temperature sensitivity in birefringent photonic crystal holey fibers. *Appl. Opt.*, **44**(36), 7780–7788.

McGowan, R. W., Gallot, G., and Grischkowsky, D. (1999). Propagation of ultrawideband short pulses of terahertz radiation through submillimeter-diameter circular waveguides. *Opt. Lett.*, **24**(20), 1431–1433.

Melendez, J. L., Carr, R., Bartholomew, D. U., Kukanskis, K. A., Elkind, J., Yee, S. S., Furlong, C. E., and Woodbury, R. G. (1996). A commercial solution for surface plasmon sensing. *Sens. Actuators B*, **35**, 212.

Mignanelli, M., Wani, K., Ballato, J., Foulger, S., and Brown, P. (2007). Polymer microstructured fibers by one-step extrusion. *Opt. Express*, **15**(10), 6183–6189.

Mittleman, D., Jacobsen, R., Neelamani, R., Baraniuk, R., and Nuss, M. (1998). Gas sensing using terahertz time-domain spectroscopy. *Applied Physics Letters B*, **67**, 379–390.

Miyamaru, F., Takeda, M. W., Suzuki, T., and Otani, C. (2007). Highly sensitive surface plasmon terahertz imaging with planar plasmonic crystals. *Opt. Express*, **15**(22), 14804–14809.

Monzon-Hernandez, D. and Villatoro, J. (2006). High-resolution refractive index sensing by means of a multiple-peak surface plasmon resonance optical fiber sensor. *Sens. Actuators B*, **115**, 227.

Monzón-Hernández, D., Villatoro, J., Talavera, D., and Luna-Moreno, D. (2004). Optical-fiber surface-plasmon resonance sensor with multiple resonance peaks. *Appl. Opt.*, **43**(6), 1216–1220.

Morikawa, K., Fujisawa, T., Saitoh, K., and Koshiba, M. (2006). Transmission characteristics of laterally illuminated photonic crystal fibers. *IEICE Electr. Express*, **3**, 70–73.

Mortensen, N. A. (2002). Effective area of photonic crystal fibers. *Opt. Express*, **10**(7), 341–348.

Murao, T., Saitoh, K., and Koshiba, M. (2006). Design of air-guiding modified honeycomb photonic band-gap fibers for effectively singlemode operation. *Opt. Express*,

14(6), 2404–2412.

Nagel, M., Bolivar, P. H., Brucherseifer, M., Kurz, H., Bosserhoff, A., and Büttner, R. (2002). Integrated thz technology for label-free genetic diagnostics. *Applied Physics Letters*, **80**(1), 154–156.

Nagel, M., Marchewka, A., and Kurz, H. (2006). Low-index discontinuity terahertz waveguides. *Opt. Express*, **14**(21), 9944–9954.

Nasilowski, T., Martynkien, T., Statkiewicz, G., Szpulak, M., Olszewski, J., Golojuch, G., Urbanczyk, W., Wojcik, J., Mergo, P., Makara, M., Berghmans, F., and Thienpont, H. (2005). Temperature and pressure sensitivities of the highly birefringent photonic crystal fiber with core asymmetry. *Applied Physics B: Lasers and Optics*, **81**, 325–331.

Nielsen, M., Mortensen, N., Albertsen, M., Folkenberg, J., Bjarklev, A., and Bonacinni, D. (2004). Predicting macrobending loss for large-mode area photonic crystal fibers. *Opt. Express*, **12**(8), 1775–1779.

O'Hara, J., Averitt, R., and Taylor, A. (2005). Prism coupling to terahertz surface plasmon polaritons. *Opt. Express*, **13**(16), 6117–6126.

Omniguide. http://www.omni-guide.com.

Ortigosa-Blanch, A., Diez, A., Delgado-Pinar, M., Cruz, J., and Andres, M. (2004). Temperature independence of birefringence and group velocity dispersion in photonic crystal fibres. *Electronics Letters*, **40**(21), 1327–1329.

Ozisik, M. (1993). *Heat Conduction.* John Wiley & Sons, INC., second edition.

Park, H., Cho, M., Kim, J., and Han, H. (2002). Terahertz pulse transmission in plastic photonic crystal fibres. *Physics in Medicine and Biology*, **47**(21), 3765–3769.

Patskovsky, S., Kabashin, A. V., and Meunier, M. (2005). Near-infrared surface plasmon resonance sensing on a si platform with nanoparticle-based signal enhancement. *Optical Materials*, **27**(5), 1093 – 1096. Si-based Photonics: Towards True Monolithic Integration.

Pendry, J. B., Holden, A. J., Robbins, D. J., and Stewart, W. J. (1998). Low frequency plasmons in thin-wire structures. *Journal of Physics: Condensed Matter*, **10**(22), 4785–4809.

Pendry, J. B., Holden, A. J., Stewart, W. J., and Youngs, I. (1996). Extremely low frequency plasmons in metallic mesostructures. *Phys. Rev. Lett.*, **76**(25), 4773–4776.

Piliarik, M., Homola, J., Manikova, Z., and Ctyroky, J. (2003). *Sens. Actuators B*, **90**, 236.

Poli, F., Foroni, M., Giovanelli, D., Cucinotta, A., Selleri, S., Jensen, J. B., Lægsgaard, J., Bjarklev, A., Vienne, G., Jakobsen, C., and Broeng, J. (2007). Silica bridge impact on hollow-core bragg fiber transmission properties. In *Optical Fiber Communication Conference and Exposition and The National Fiber Optic Engineers Conference*, page OML8. Optical Society of America.

Pone, E., Dubois, C., Gu, N., Gao, Y., Dupuis, A., Boismenu, F., Lacroix, S., and Skorobogatiy, M. (2006a). Drawing of the hollow all-polymer bragg fibers. *Opt. Express*, **14**(13), 5838–5852.

Pone, E., Dubois, C., Guo, N., Lacroix, S., and Skorobogatiy, M. (2006b). Newtonian and non-newtonian models of the hollow all-polymer bragg fiber drawing. *J. Lightwave Technol.*, **24**(12), 4991–4999.

Pone, E., Hassani, A., Lacroix, S., and Skorobogatiy, M. (2008). A pressure sensor based on the loss birefringence of a microstructured optical fiber containing metal coated elliptical inclusions. In *Conference on Lasers and Electro-Optics/Quantum Electronics and Laser Science Conference and Photonic Applications Systems Technologies*, page CMZ3. Optical Society of America.

Qiu, M. (2005). Photonic band structures for surface waves on structured metal surfaces. *Opt. Express*, **13**(19), 7583–7588.

Raether, H. (1988). *Surface Plasmons on Smooth and Rough Surfaces and on Gratings*. Springer.

Rivas, J. G., Kuttge, M., Kurz, H., Bolivar, P. H., and Sánchez-Gil, J. A. (2006). Low-frequency active surface plasmon optics on semiconductors. *Applied Physics Letters*, **88**(8), 082106.

Rubin, B. (1999). Tailored fiber cross sections. *Adv. Mat.*, **10**, 1225–1227.

Rubin, B., Kobsa, H., and Shearer, S. (1994). Modeling the dependence of fabric reflectance on denier per filament. *Textile Res. J.*, **64**, 685–689.

Rubin, B., Kobsa, H., and Shearer, S. M. (1997). Prediction and verification of an iridescent synthetic fiber. *Appl. Opt.*, **36**(25), 6388–6392.

Russel, P. (2006). Photonic crystal fibers. *J. Lightwave Technol.*, **24**, 4729–4749.

Saitoh, K., Tsuchida, Y., Koshiba, M., and Mortensen, N. A. (2005). Endlessly single-mode holey fibers: the influence of core design. *Opt. Express*, **13**(26), 10833–10839.

Sazio, P. J. A., Amezcua-Correa, A., Finlayson, C. E., Hayes, J. R., Scheidemantel, T. J., Baril, N. F., Jackson, B. R., Won, D.-J., Zhang, F., Margine, E. R., Gopalan, V., Crespi, V. H., and Badding, J. V. (2006). Microstructured Optical Fibers as High-Pressure Microfluidic Reactors. *Science*, **311**(5767), 1583–1586.

Schuster, J., Trahan, M., and D. Heider, W. L. (2003). Influence of fabric ties on the performance of woven-in optical fibres. *Composites Part A - Appl. Science & Manufacturing*, **34**, 855–861.

Selem, B., Rothmaier, M., Camenzind, M., Khan, T., and Walt, H. (2007). Novel flexible light diffuser and irradiation properties for photodynamic therapy. *J. Biomed. Opt.*, **12**, 34024.

Shapira, O., Kuriki, K., Orf, N. D., Abouraddy, A. F., Benoit, G., Viens, J. F., Rodriguez, A., Ibanescu, M., Joannopoulos, J. D., Fink, Y., and Brewster, M. M. (2006). Surface-emitting fiber lasers. *Opt. Express*, **14**(9), 3929–3935.

Sheridan, A. K., Harris, R. D., Bartlett, P. N., and Wilkinson, J. S. (2004). Phase interrogation of an integrated optical spr sensor. *Sens. Actuators B*, **97**, 114.

Shevchenko, Y. Y. and Albert, J. (2007). Plasmon resonances in gold-coated tilted fiber bragg gratings. *Opt. Lett.*, **32**(3), 211–213.

Sirikasemlert, A. and Tao, X. (1999). Effects of fabric parameters on specular reflection of single-jersey knitted fabrics. *Textile Res. J.*, **69**, 663–675.

Skorobogatiy, M. (2005). Efficient antiguiding of te and tm polarizations in low-index core waveguides without the need for an omnidirectional reflector. *Opt. Lett.*, **30**(22), 2991–2993.

Skorobogatiy, M. (2006). Efficient antiguiding without omnidirectional reflectors. In *Conference on Lasers and Electro-Optics/Quantum Electronics and Laser Science Conference and Photonic Applications Systems Technologies*, page JWB87. Optical Society of America.

Skorobogatiy, M. and Dupuis, A. (2007). Ferroelectric all-polymer hollow bragg fibers for terahertz guidance. *Appl. Phys. Lett.*, **90**, 113514.

Skorobogatiy, M., Dupuis, A., and Guo, N. (2007). Design and fabrication of ferroelectric all-polymer hollow bragg fibers for thz guidance. In *National Fiber Optic Engineers Conference*, page JWA98. Optical Society of America.

Skorobogatiy, M. and Guo, N. (2007a). Bandwidth enhancement by differential mode attenuation in multimode photonic crystal bragg fibers. *Opt. Lett.*, **32**(8), 900–902.

Skorobogatiy, M. and Guo, N. (2007b). Bandwidth enhancement by differential mode attenuation in multimode photonic crystal bragg fibers. In *Conference on Lasers and Electro-Optics/Quantum Electronics and Laser Science Conference and Photonic Applications Systems Technologies*, page CWF3. Optical Society of America.

Skorobogatiy, M., Jacobs, S., Johnson, S., and Fink, Y. (2002). Geometric variations in high index-contrast waveguides, coupled mode theory in curvilinear coordinates. *Opt. Express*, **10**(21), 1227–1243.

Skorobogatiy, M. and Kabashin, A. (2006a). Photon crystal waveguide-based surface plasmon resonance biosensor. *Appl. Phys. Lett.*, **89**, 211641.

Skorobogatiy, M. and Kabashin, A. (2007). Photon crystal waveguide-based surface plasmon resonance biosensor. In *Conference on Lasers and Electro-Optics/Quantum Electronics and Laser Science Conference and Photonic Applications Systems Technologies*, page CThZ3. Optical Society of America.

Skorobogatiy, M. and Yang, J. (2008). *Fundamentals of Photonic Crystal Guiding*. Cambridge University Press.

Skorobogatiy, M. A. and Kabashin, A. (2006b). Plasmon excitation by the gaussian-like core mode of a photonic crystal waveguide. *Opt. Express*, **14**(18), 8419–8424.

Slavik, R., Homola, J., and Ctyroký, J. (1998). Miniaturization of fiber optic surface plasmon resonance sensor. *Sensors and Actuators B: Chemical*, **51**(1-3), 311 – 315.

Snyder, A. and Love, J. (1983). *Optical Waveguide Theory*. Chapman Hall, New York,.

Sokkar, T., Kabeel, M., Ramadan, W., and Hamza, A. (1992). A contribution to the study of color of fabrics. *Color Res. Appl.*, **17**, 219–224.

Spigulis, J., Pfafrods, D., Stafekis, M., and Jelinska-Platace, W. (1997). The 'glowing' optical fibre designs and parameters. In *Proceedings of SPIE, the International Society for Optical Engineering*, pages 231–236. Society of Photo-Optical Instrumentation Engineers.

Suzuki, H., Sugimoto, M., Matsuiand, Y., and Kondoh, J. (2006). Fundamental characteristics of a dual-colour fibre optic spr sensor. *Meas. Sci. Technol.*, **17**, 1547.

Takeyasu, N., Tanaka, T., and Kawata, S. (2005). Metal deposition deep into microstructure by electroless plating. *Japanese Journal of Applied Physics*, **44**(35), L1134–L1137.

Temelkuran, B., Hart, S. D., Benoit, G., Joannopoulos, J. D., and Fink, Y. (2002). Wavelength-scalable hollow optical fibres with large photonic bandgaps for co2 laser transmission. *Nature*, **420**, 650–653.

Themistos, C., Rahman, B. M. A., Rajarajan, M., Grattan, K. T. V., Bowden, B., and Harrington, J. A. (2007). Characterization of silver/polystyrene (ps)-coated hollow

glass waveguides at thz frequency. *J. Lightwave Technol.*, **25**(9), 2456–2462.

Trouillet, A., Ronot-Trioli, C., Veillas, C., and Gagnaire, H. (1996). Chemical sensing by surface plasmon resonance in a multimode optical fibre. *Pure Appl. Opt.*, **5**, 227.

Tubb, A. J. C., Payne, F. P., Millington, R. B., and Lowe, C. R. (1997). Single-mode optical fibre surface plasma wave chemical sensor. *Sens. Actuators B*, **41**, 71.

Uskokovic, P., Balac, I., Brajovic, L., Simic, M., Putic, S., and Aleksic, R. (2001). Delamination detection in woven composite laminates with embedded optical fibers. *Adv. Eng. Mat.*, **3**, 492–496.

Uskokovic, P., Miljkovic, M., Krivokuca, M., Putic, S., and Aleksici, R. (1999). An intensity based optical fibre sensor for flexural damage detection in woven composites. *Adv. Composits Lett.*, **8**, 55–58.

van Eijkelenborg, M. A., Argyros, A., Bachmann, A., Barton, G., Large, M. C. J., Henry, G., Issa, N. A., Klein, K. F., Poisel, H., Pok, W., Poladian, L., Manos, S., and Zagari, J. (2004). Bandwidth and loss measurements of graded-index microstructured polymer optical fibre. *Electron. Lett.*, **40**, 592.

Vidal, M. B., Lopez, R., Aleggret, S., Alonso-Chamarro, J., Garces, I., and Mateo, J. (1993). Determination of probable alcohol yield in musts by means of an spr optical sensor. *Sens. Actuators B*, **11**, 455.

Vienne, G., Xu, Y., Jakobsen, C., Deyerl, H.-J., Jensen, J., Sorensen, T., Hansen, T., Huang, Y., Terrel, M., Lee, R., Mortensen, N., Broeng, J., Simonsen, H., Bjarklev, A., and Yariv, A. (2004). Ultra-large bandwidth hollow-core guiding in all-silica bragg fibers with nano-supports. *Opt. Express*, **12**(15), 3500–3508.

Wakita, A. and Shibutani, M. (2006). Mosaic textile: wearable ambient display with non-emissive color-changing modules. In *ACE '06: Proceedings of the 2006 ACM SIGCHI international conference on Advances in computer entertainment technology*, New York, NY, USA, page 48. ACM.

Wang, K. and Mittleman, D. M. (2004). Metal wires for terahertz wave guiding. *Nature*, **432**, 376–379.

Wang, K. and Mittleman, D. M. (2006). Dispersion of surface plasmon polaritons on metal wires in the terahertz frequency range. *Physical Review Letters*, **96**(15), 157401.

Wegmuller, M., Legre, M., Gisin, N., Ritari, T., Ludvigsen, H., Folkenberg, J., and Hansen, K. (2004). Experimental investigation of wavelength and temperature dependence of phase and group birefringence in photonic crystal fibers. *Transparent Optical Networks, 2004. Proceedings of 2004 6th International Conference on*, **2**, 111–114 vol.2.

Weiss, M. N., Srivastava, R., and Grogner, H. (1996). Experimental investigation of a surface plasmon-based integratedoptic humidity sensor. *Electron. Lett.*, **32**, 842.

Weisser, M., Menges, B., and Mittler-Neher, S. (1999). Refractive index and thickness determination of monolayers by plasmons. *Sens. Actuators B*, **56**, 189.

Westbrook, P., Eggleton, B., Windeler, R., Hale, A., Strasser, T., and Burdge, G. (2000). Cladding-mode resonances in hybrid polymer-silica microstructured optical fiber gratings. *Photonics Technology Letters, IEEE*, **12**(5), 495–497.

White, T. P., Kuhlmey, B. T., McPhedran, R. C., Maystre, D., Renversez, G., de Sterke, C. M., and Botten, L. C. (2002). Multipole method for microstructured optical fibers. i. formulation. *J. Opt. Soc. Am. B*, **19**(10), 2322–2330.

Wolinski, T. R., Szaniawska, K., Ertman, S., Lesiak, P., Domanski, A. W., Dabrowski, R., Nowinowski-Kruszelnicki, E., and Wojcik, J. (2006). Influence of temperature and electrical fields on propagation properties of photonic liquid-crystal fibres. *Measurement Science and Technology*, **17**(5), 985–991.

Wu, D., Fang, N., Sun, C., Zhang, X., Padilla, W. J., Basov, D. N., Smith, D. R., and Schultz, S. (2003). Terahertz plasmonic high pass filter. *Applied Physics Letters*, **83**(1), 201–203.

Xu, J., Plaxco, K. W., and Allen, S. J. (2006). Probing the collective vibrational dynamics of a protein in liquid water by terahertz absorption spectroscopy. *Protein Sci*,

15(5), 1175–1181.

Xue, S., Tanner, R., Barton, G., Lwin, R., Large, M., and Poladian, L. (2005a). Fabrication of microstructured optical fibers-part i: problem formulation and numerical modeling of transient draw process. *Lightwave Technology, Journal of*, **23**(7), 2245–2254.

Xue, S., Tanner, R., Barton, G., Lwin, R., Large, M., and Poladian, L. (2005b). Fabrication of microstructured optical fibers-part ii: numerical modeling of steady-state draw process. *Lightwave Technology, Journal of*, **23**(7), 2255–2266.

Xue, S. C., Large, M. C. J., Barton, G. W., Tanner, R. I., Poladian, L., and Lwin, R. (2006). Role of material properties and drawing conditions in the fabrication of microstructured optical fibers. *J. Lightwave Technol.*, **24**(2), 853.

Yamaguchi, S. and Takanabe, H. (2001). Fibers having fine concave and convex surface from silica hybrid polyester. *Sen-I akkaishi*, **57**, 111–119.

Zhang, H., Gao, W., and Qiu, H. (2003). Retro-reflection of round fibers. *Textile Res. J.*, **73**, 965–970.

Zhang, L. and Uttamchandani, D. (1988). Optical chemical sensing employing surface plasmon resonance. *Electron. Lett.*, **23**, 1469.

Zhao, C.-L., Yang, X., Lu, C., Jin, W., and Demokan, M. (2004). Temperature-insensitive interferometer using a highly birefringent photonic crystal fiber loop mirror. *Photonics Technology Letters, IEEE*, **16**(11), 2535–2537.

Zheng, Y., Pitsianis, N., and Brady, D. (2006). Nonadaptive group testing based fiber sensor deployment for multiperson tracking. *IEEE Sens. J.*, **6**, 490–494.

Zivkovic, I., Brajovic, L., Uskokovic, P., and Aleksic, R. (2005). Indentation damage detection in thermoplastic composite laminates by using embedded optical fibers. *J. Adv. Mat.*, **37**, 33–37.

Zou, L., Bao, X., V., S. A., and Chen, L. (2004). Dependence of the brillouin frequency shift on strain and temperaturein a photonic crystal fiber. *Opt. Lett.*, **29**(13), 1485–1487.